Multiscale modelling of streamers

PROEFSCHRIFT

ter verkrijging van de graad van doctor aan de Technische Universiteit Eindhoven, op gezag van de rector magnificus prof.dr. S.K. Lenaerts, voor een commissie aangewezen door het College voor Promoties, in het openbaar te verdedigen op woensdag 29 november 2023 om 16:00 uur

door

Dennis Derek Bouwman

geboren te Amsterdam

Dit proefschrift is goedgekeurd door de promotoren en de samenstelling van de promotiecommissie is als volgt:

Voorzitter:	prof.dr. Kees Storm	
Promotor:	prof.dr. Ute Ebert	
Co-promotoren:	dr. Jannis Teunissen	(Centrum Wiskunde & Informatica)
	dr. Alejandro Luque Estepa	(Instituto de Astrofísica de Andalucía)
Leden:	prof.dr. Gerrit Kroesen	
	dr.ir. Sander Nijdam	
	prof.dr.ir. Wim van Saarloos	(Universiteit Leiden)

CWI

Research institute for mathematics &
computer science in the Netherlands

Acknowledgements

I have much to be grateful of and I have received great support from many people throughout the years. Often this support was found in little things that are easily overlooked. Nevertheless they are of great importance. So before we dive into the marvellous multi-scale world of streamer discharges I would like to direct a few words to the people that, to me, represent these little things:

To my parents, Guido and Joke: I have so much to thank you for. Thank you for being the solid foundation that I needed at times, especially in the first year of my Ph.D. when it was difficult to find suitable housing. Thank you for always being there for me. I shall miss my Wednesday sleep-overs in Amstelveen.

My deep gratitude is offered to *de vosjes* and my roommates in OD54. Thank you for welcoming me back home during the COVID-19 pandemic. This so-called *double-boomerang* has had a profound impact on my happiness. Truly, there was no better place to weather the storm.

Piotr and Elena, thanks for all the fun visits in Amsterdam. Your (old) Wi-Fi password is an inspiration to us all.

Many thanks to Karin and Gert-Jan for always having just the right screw. It is a great pleasure to have such kind neighbours and wonderful family.

I would like to thank *de nerd vrienden* for the countless board-games throughout the years. May the call for an honest game of *doerak* never go unanswered! Your regular company and endless banter is very dear to me. In the spirit of that banter: if any of you ever wants to improve their gameplay you should come to me and I will give you some free doctor's advice.

A special shout-out goes to Mark for being a superb *Dungeon Master*. Your creativity, spontaneity and laissez-faire attitude to bad ideas is the spark driving our amazing campaign.

I am very grateful for my brothers William and Morris. Morris, thank you for your enthusiasm and excellent graphic skills which have resulted in the beautiful cover of my thesis.

En nu ter zake.

Summary

Streamers are a common initial stage of electric discharges. They are growing filaments of ionized gas that create an initial conducting path which can later develop into a spark. Streamer discharges are studied because of their relevance to dielectric breakdown, which is important for high-voltage devices, plasma-chemical applications and atmospheric electricity.

Streamers are multiscale phenomena, with widely varying spatial and temporal scales. To simulate this one can develop a hierarchy of models, which simultaneously resolves the interactions between particles and the behaviour of the ensemble. A well-known example is the methodology leading to the plasma fluid model and variants thereof. Simulations using such models have proven to be a powerful tool to investigate the physics of streamer discharges. Nevertheless such models are computationally expensive when trying to simulate the collective dynamics of discharges composed of many streamers. To overcome this limitation a simplified, yet physically-sound, macroscopic representation of streamers has to be developed.

In this thesis we will traverse the hierarchy of models for streamers and then extend this towards the macroscopic scale. The first half of this thesis is motivated by applications involving plasma-assisted combustion, which is why there is an emphasis on air-methane mixtures. On the smallest scale we focus on electron scattering cross sections with methane. We highlight an inconsistency in the data regarding neutral dissociation. We suggest cross sections for neutral dissociation and formulate a complete and consistent cross section set. Then we continue to the mesoscopic scale as we investigate positive streamers in stoichiometric air-methane mixtures by three-dimensional particle-in-cell simulations. We show that the addition of 9.5% methane strongly affects the photoionization mechanism which results in more frequent branching. Additionally, we calculate plasma-chemical quantities of these streamers. Finally we extend the hierarchy of models to the macroscopic scale. We characterize single positive streamers in terms of only a handful of macroscopic parameters. To that end we derive analytic approximations of electron dynamics in terms

of these parameters. We use these to show how to calculate all macroscopic parameters of steady positive streamers in air as a function of the applied background electric field. Our predictions are in reasonable agreement with results from numerical simulations. This indicates that our model captures the relevant physics of steady streamers using a simple macroscopic representation.

Samenvatting

Streamers zijn een veelvoorkomende beginfase van elektrische ontladingen. Het zijn groeiende filamenten van geïoniseerd gas die een eerste geleidende pad vormen dat zich later kan ontwikkelen tot een vonk. Streamer ontladingen worden onderzocht omdat ze relevant zijn voor diëlektrische doorslag, wat weer belangrijk is voor hoogspanningsapparatuur, plasma-chemische toepassingen en atmosferische elektriciteit.

Streamers zijn een meerschalen fenomeen, met uiteenlopende ruimte- en tijd-schalen. Om dit te simuleren heeft men een hiërarchie van modellen ontwikkeld die gelijktijdig de wisselwerking tussen individuële deeltjes en het gedrag van het geheel kan beschrijven. Een schoolvoorbeeld hiervan is de methodiek die tot de plasma-stromingsvergelijkingen leidt. Simulaties met zulke modellen hebben hebben hun nut bewezen als het aankomt op de natuurkundige beschrijving van streamer ontladingen. Desondanks vereisen zulke modellen erg veel rekenkracht, vooral wanneer we ontladingen simuleren die zijn opgebouwd uit veel streamers. Om dit probleem te overkomen hebben we een versimpelde, maar natuurkundig-correcte, macroscopische weergave van streamers nodig.

In dit proefschrift zullen we de hiërarchie van modellen voor streamers doorlopen en dit uitbreiden naar de macroscopische schaal. De eerste helft van dit proefschrift wordt tevens gemotiveerd door de toepassingen van plasma-ondersteunde verbranding, waardoor er een nadruk ligt op lucht-methaan mengsels. Op de kleinste schaal concentreren wij ons op de botsingsdoorsneden voor reacties tussen elektronen en methaan. We laten zien dat de bestaande literatuur niet consistent is wanneer het aankomt op neutrale dissociatie. Voor dit proces stellen wij nieuwe botsingsdoorsneden voor en laten zien dat je hiermee een complete en consistente verzameling aan botsingsdoorsneden krijgt. Daarna gaan we verder op de mesoscopische schaal waar we positieve streamers in stoichiometrische lucht-methaan mengsels onderzoeken middels drie-dimensionale deeltjes simulaties. We laten zien dat de toevoeging van 9.5% methaan het photoïonizatie mechanisme sterk beïnvloed en dat er daardoor meer vertakkingen onstaan. Daarbij berekenen we enkele plasma-chemische

quantiteiten van deze streamers. Tot slot breiden we de hiërarchie van modellen uit naar de macrscopische schaal. We beschrijven streamers met slechts een paar macroscopische parameters. Om dat te bereiken leiden we eerst analytische benaderingen voor de elektronen dynamica af in termen van deze macroscopische parameters. Die benaderingen gebruiken we vervolgens om te laten zien hoe men de macroscopische parameters van *steady* positieve streamers in lucht kan berekenen als functie van het opgelegde elektrische veld. Onze voorspellingen komen redelijk overeen met de resultaten van numerieke simulaties. Dit duidt aan dat ons model de relevante natuurkunde van *steady* streamers omvat met een simpele macroscopische weergave

Table of contents

Chapter 1

Introduction

Air is essentially an electrical insulator. We experience this every time we disconnect an electronic device from its power source. Even for high voltage transmission lines a few meters of air is sufficient for safe insulation. At the same time there are many examples of electricity flowing through air in the form of an electric spark. The most prominent spark is a lightning strike. This shows that under specific conditions air can change from an insulator to a conductor. Even though sparks appear to be instantaneous, they are in fact the result of a fast and complex sequence of events that eventually transform a small portion of air into an electrically conducting medium. At the heart of the formation of sparks is a phenomenon called the *streamer discharge*, which is the topic of this thesis. Streamers are growing filaments of ionized gas that create the initial conducting path which can later develop into a spark. Figures 1.1 and 1.2 show streamers generated in the lab and a natural streamer discharge occurring high above thunderclouds.
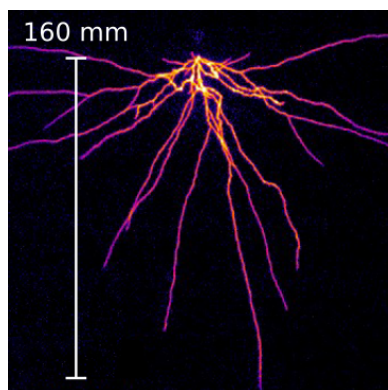
Fig. 1.1 Streamers in the lab. Image taken from [1]
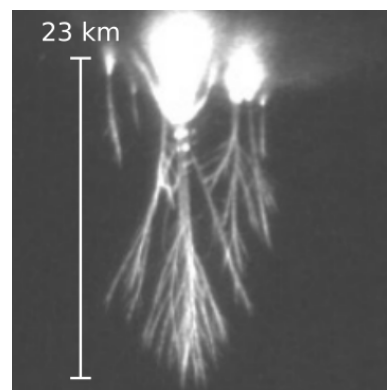
Fig. 1.2 Streamers in nature. Image taken from [2]

1.1   Why study electrical discharges?

Prior to explaining the physics of streamers, we shall consider why we are interested in electric discharges in the first place. We base our motivation on three applications:

1. **High-voltage engineering:** High-voltage power systems require specialized equipment to safely interrupt electric currents. Gas circuit breakers are used for this purpose. These components can contain the gas sulfur-hexafluoride (SF_6) because of its superb discharge-suppressing properties. Sadly, SF_6 is also a potent greenhouse gas with a global warming potential of 23.900 times that of CO_2 over a 100 year period [3]. Understanding the formation of sparks can aid the search for suitable replacements of SF_6 in gas circuit breakers.

2. **Plasma-chemistry:** Electric discharges initiate chemical reactions that would not occur thermally at room temperature and pressure. An example of this is ozone generation. Ozone (O_3) is widely used for disinfection and in pharmaceuticals. Discharges in air produce this compound, for example, when an energetic electron breaks up an oxygen molecule and the fragment reacts to produce ozone [4]

$$e + O_2 \rightarrow e + O + O, \quad \text{and then} \quad O + O_2 + N_2 \rightarrow O_3 + N_2. \tag{1.1}$$

   The ability of discharges to trigger chemical reactions without the requirement of elevated temperatures or pressures promises environmentally-friendly alternatives to traditional chemical production. Examples of other chemical applications are: industrial surface treatment [5], plasma-medicine [6] and plasma-activated water [7]. Another noteworthy application is plasma-assisted combustion, where electric discharges are used to trigger other chemical reaction pathways with the aim of enhancing control over combustion and ignition processes [8]. An understanding of electric discharges and the chemistry they initiate is key to improving such methods.

3. **Atmospheric electricity:** Thunderclouds separate huge amounts of charge over vast distances. This results in discharges of a spectacular kind, such as lightning strikes. Other examples of atmospheric electricity are blue jets and sprites. In fact, the discharge shown in figure 1.2 is a sprite. Streamers play an important role in sprites and the development of lightning strikes. A full understanding of atmospheric electricity must therefore include a detailed description of the streamer.
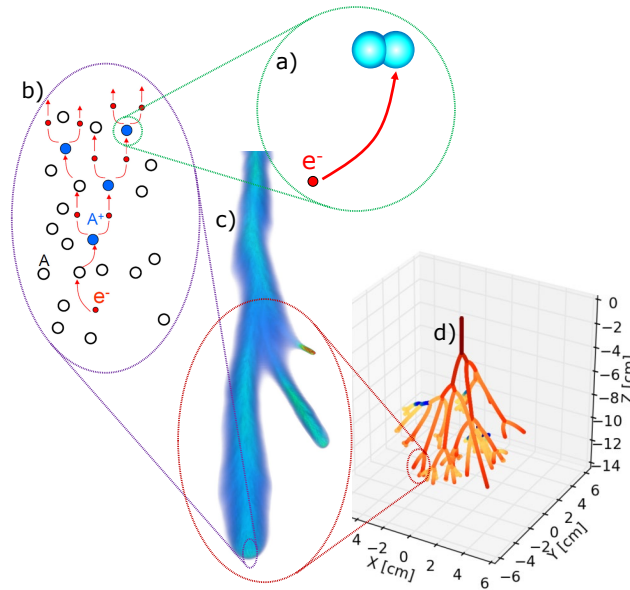
Fig. 1.3 The multiscale nature of streamer discharges: (a) individual electron-molecule collisions, (b) start of an electron avalanche, (c) the plasma fluid representation and (d) a streamer tree. Image taken from [9], inset (d) was taken from [10].

1.2   The multiscale nature of streamers

Streamer discharges involve a wide range of temporal and spatial scales. In air at 1 bar and room temperature the spatial scales range from the mean free path of an electron (tens of nanometers), through the typical scale of the diameter of the streamer head (several millimeters), and on to the size of an ensemble of numerous interacting streamers (up to a meter or more). Models of streamers thus have to span all these scales which is a huge theoretical and computational challenge. To overcome this it is common to employ a hierarchy of models: on each scale we give a convenient description of the relevant physics which is then included in coarser-scale models. In the coming sections we start at the smallest scale and zoom out until we finally arrive on the scale of streamer trees. This is illustrated in figure 1.3.

1.2.1   Particle interactions

The smallest length scale concerns the interactions between particles: electrons, molecules and photons. Consider a gas to which an electric field is applied. Free electrons gain energy as they are accelerated by this electric field. As the electron (e) moves through the gas it

encounters much heavier atoms and molecules (M) with which it can collide[1]. There are different types of relevant electron collisions:

- Most common is the elastic collision, which leaves M practically unchanged: $e + M \rightarrow e + M$.

- The electron can also transfer part of its kinetic energy to the internal energy of M and put it in an excited state: $e + M \rightarrow e + M^*$. Here M^* refers to rotational, vibrational or electronically excited states. If M is a molecule then inelastic collisions can also lead to dissociation.

- Highly energetic electrons are able to liberate other electrons by impact ionization: $e + M \rightarrow e + e + M^+$. This increases the number of free electrons and creates a positive ion M^+. Dissociative ionization of molecules is also possible.

- Electrons can also attach to molecules: $e + M + M \rightarrow M^- + M$. This decreases the number of free electrons and creates a negative ion M^-. Non-dissociative electron attachment collisions are three-body processes, which means that it is far more likely to occur if a third particle is present. Dissociative attachment of molecules is also possible and do not require a third particle, e.g. $e + O_2 \rightarrow O^- + O$.

For most practical purposes collisions are modelled statistically using cross sections. The cross section is a measure of the probability that a certain collision occurs and it is dependent on the energy of the incoming electron. Within the context of electric discharges, where we find large numbers of free electrons behaving similarly, a statistical description of electron collisions is convenient and accurate. Traditionally cross sections are obtained by experimental observation [11], however for atoms and simple molecules they can also be calculated using methods from computational quantum dynamics [12]. In chapter 2 we review and propose electron scattering cross sections with methane.

Other types of particle interactions worth mentioning are chemical reactions and interactions involving photons and ions:

- Excited states, ions or dissociated molecules generally are more reactive and undergo chemical reactions, such as ozone production described in (1.1). For plasma-chemical applications it is important to account for the reaction pathways of interest.

---

[1] In principle an electron can also encounter ions, excited states and other free electrons. However, for streamers such particle interactions are highly unlikely. This is explained by the low ionization degree of streamers which is typically around 10^{-5}. In other words, there is such a dominant abundance of neutral atoms and molecules that free electrons practically only encounter M. We therefore only have to consider collisions with M.

- Interactions with high-energy photons (in the UV energy range) can be important to consider. Specifically in air such photons (γ) are produced by the discharge itself and create new electrons in a three-step process [13]

$$e + N_2 \rightarrow e + N_2^*,$$
$$N_2^* \rightarrow N_2 + \gamma,$$
$$\gamma + O_2 \rightarrow e + O_2^+.$$
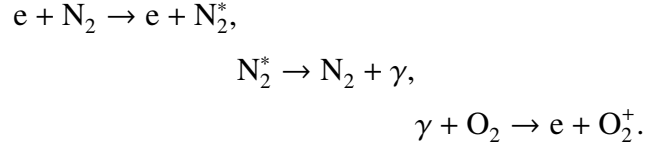
  This process is called photoionization. Although photoionization is generally weak it is important because it is non-local, as the photon will travel some distance between emission and absorption. Through photoionization the discharge can pre-ionize regions where it has not yet travelled. This is can be essential for certain discharges, e.g. positive streamers. Photon-molecule interactions are also modelled using cross sections.

- In principle ions also accelerate in the electric field and undergo similar collisions as electrons. However, since ions are much heavier than electrons they accelerate much slower and they lose more energy in elastic collisions with other atoms and molecules. Therefore we shall ignore the slow motion of ions for now and only consider electrons as mobile particles.

1.2.2   Particle model

Next we introduce particle models to simulate the stochastic motion of an electron under the influence of collisions. Within a particle model we solve the equations of motion that describe the deterministic trajectory of an electron between collisions

$$\begin{cases} \partial_t \mathbf{x}(t) = \mathbf{v}(t), \\[2mm] \partial_t \mathbf{v}(t) = \dfrac{q_e}{m_e}\, \mathbf{E}(\mathbf{x}(t), t), \end{cases} \tag{1.2}$$

where $\mathbf{x}$ is the position, $\mathbf{v}$ is the velocity, q_e is the electron charge, m_e is the electron mass and $\mathbf{E}$ is the electric field. When simulating the trajectory of multiple electrons this system of equations has to be solved for each electron, which is achieved by numerical integration. The deterministic trajectory is stochastically interrupted by collisions with atoms or molecules (denoted by M). The probability of having a collision is specified by the respective cross section, as explained in section 1.2.1. When a collision occurs the electron either attaches to a molecule M or its direction is changed randomly as it 'bounces' on M. If ionization occurs

then an additional electron is liberated which will embark on its own stochastic path through the gas. Additionally, after each collision the velocity of the original electron is reduced in accordance with the energy and momentum transfer associated with the collision.

An advantage of particle models is that they contain relatively few assumptions. Additionally, particle models can realistically describe fluctuations due to the random nature of individual electrons. This becomes important in chapter 3 where we show that such fluctuations influence positive streamer branching, especially in gasses with suppressed photoionization such as air-methane. A disadvantage of particle models is that they become computationally expensive for a large number of electrons. In many discharge conditions this poses severe limitations on the effectiveness of particle models.

1.2.3   Electron avalanches

In the previous sections we discussed individual collisions and the motion of an electron. Now we zoom out and consider the behaviour of an ensemble of electrons that undergo acceleration and repeated collisions.

In sufficiently high electric fields an electron is more likely to ionize than attach. Under these conditions a free electron sets off a chain reaction: as it collides it liberates more electrons by impact ionization which in turn accelerate and cause further ionization and so on. The result is an exponentially increasing number of electrons, each of which moves erratically through the gas as it repeatedly collides and is scattered in random directions. The ensemble of electrons is called an electron avalanche. Even though the path of individual electrons is stochastic the properties of the avalanche are more deterministic. It turns out that in simple conditions we can describe the evolution of the avalanche using only three coefficients:

1. The drift velocity $\mathbf{v}_{dr}$ is the velocity of the center of mass of the avalanche.

2. The diffusion coefficient D accounts for the gradual spreading of the avalanche.

3. The ionization and attachment coefficients α and η indicate the rate at which electrons ionize or attach to molecules. These two can often be combined to the effective ionization coefficient $\alpha_{eff} = \alpha - \eta$. It represents the net growth (or decay) of the avalanche.

These so-called transport and reaction coefficients can be calculated from cross section data by solving some simplified form of the Boltzmann equation [14] or by tracking the motion of individual electrons by Monte-Carlo methods [15] as explained in section 1.2.2. By doing this we have effectively described the collective behaviour of possibly millions of

electrons that undergo many more collisions by only three coefficients. Although a substantial simplification of the problem, this description is only valid when the average velocity of the electrons is in equilibrium with the electric field. This is, strictly speaking, only valid for the simplest of discharge conditions, e.g. when the electric field is constant. Moreover, as the avalanche grows it gains electrons and separates charge up to the point that the the avalanche itself starts to change the electric field. The Raether-Meek criterion is a rule of thumb that states that this situation arises once the avalanche consists of about 10^8 to 10^9 electrons in standard temperature and pressure [16, 17], which is easily reached in many discharge phenomena. Clearly, more sophisticated models are needed to describe the development of the discharge after the Raether-Meek criterion is reached.

1.2.4   Plasma fluid model

Next we introduce the plasma[2] fluid model. The central idea is that electrons and ions can be described as densities n_e and n_i, respectively. Then n_e will drift, diffuse and react under the influence of the electric field E. Ions are considered immobile here and are created by impact ionization. Additionally, it is commonly assumed that the average electron velocity is always instantly in equilibrium with the *local* electric field (even though the electric field might be varying in space and time). This is called the local field approximation and it generalizes the use of the transport and reaction coefficients to describe the local evolution of the plasma. The change of n_e, n_i and E can then be described in terms of transport and reaction coefficients similar to $\mathbf{v}_{dr}$, D and α_{eff} (In fact, there are two fundamental types of transport coefficients: bulk and flux. Bulk coefficients describe the dynamics of a group of electrons, such as an electron avalanche. On the other hand, flux coefficients characterize the properties of individual electrons which is required for plasma fluid models [18]. As a consequence we have to discern the two types of coefficients. In this chapter, we add an apostrophe whenever we refer to a flux coefficient, e.g. D'). A set of drift-diffusion-reaction equations that describes the evolution of a plasma is then given by

$$\begin{cases} \partial_t n_e = \nabla \cdot (D' \nabla n_e - \mathbf{v}'_{dr} n_e) + |\mathbf{v}'_{dr}| \alpha'_{eff} n_e, \\ \partial_t n_i = |\mathbf{v}'_{dr}| \alpha'_{eff} n_e, \\ \phi = -\nabla \mathbf{E}, \quad \epsilon_0 \nabla^2 \phi = -e(n_i - n_e), \end{cases} \tag{1.3}$$

---

[2]A *plasma* is a state of matter characterized by the presence of charged particles, such as ions and free electrons, that exhibit long-range interactions through electric and magnetic fields. Electric gas discharges are plasmas.
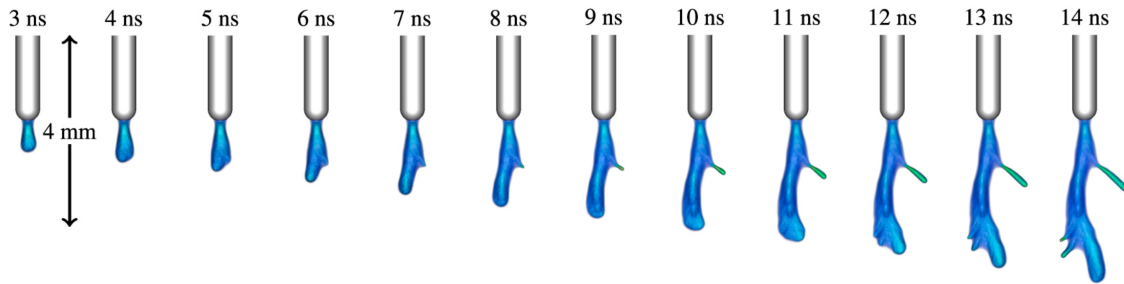
Fig. 1.4 Simulation of a streamer growing from an electrode using a plasma fluid model. The blue-green colors indicate the electron density. The streamer grows as it ionizes the gas at the extremities of the filaments. The number of filaments can increase due to branching. Image taken from [19]

where e is the elementary charge and ϕ is the electrostatic potential. The last line of equation (1.3) is Poisson's equation, it describes how the charges of the plasma itself generate an electrostatic potential and electric field.

The plasma fluid model describes a broad range of discharge phenomena. Its use is widespread and there are many variants of this model that account for additional physical mechanism such as: photoionization, secondary chemical reactions, gas dynamics, surface interactions and so on.

The fluid model can describe the electron avalanche past the Raether-Meek criterion. As the electrons drift forward they leave positive ions behind that were produced by impact ionization. This causes a separation of charge, similar to an electric dipole, that is strong enough to affect E. Because the dipole is aligned with the applied electric field it enhances E at its poles which intensifies the ionization coefficient there. Eventually a streamer emerges from this self-intensifying process. A streamer is a plasma filament that grows as it ionizes the gas at its extremity, also called the head, due to the local enhancement of the electric field. In figure 1.4 we show a numerical simulation of a streamer using a fluid model.

1.2.5   Axial approximations and streamer tree models

Streamers rarely come alone because they have a tendency to branch. Repeated branching events give rise to a tree-like structure of multiple filaments. The streamer heads interact through the electric field and possibly photoionization. In principle we can simulate and study streamer trees using the fluid model. An example is shown in the left panel of figure 1.5. This simulation of a streamer tree with a height of 15 mm required two days of calculation
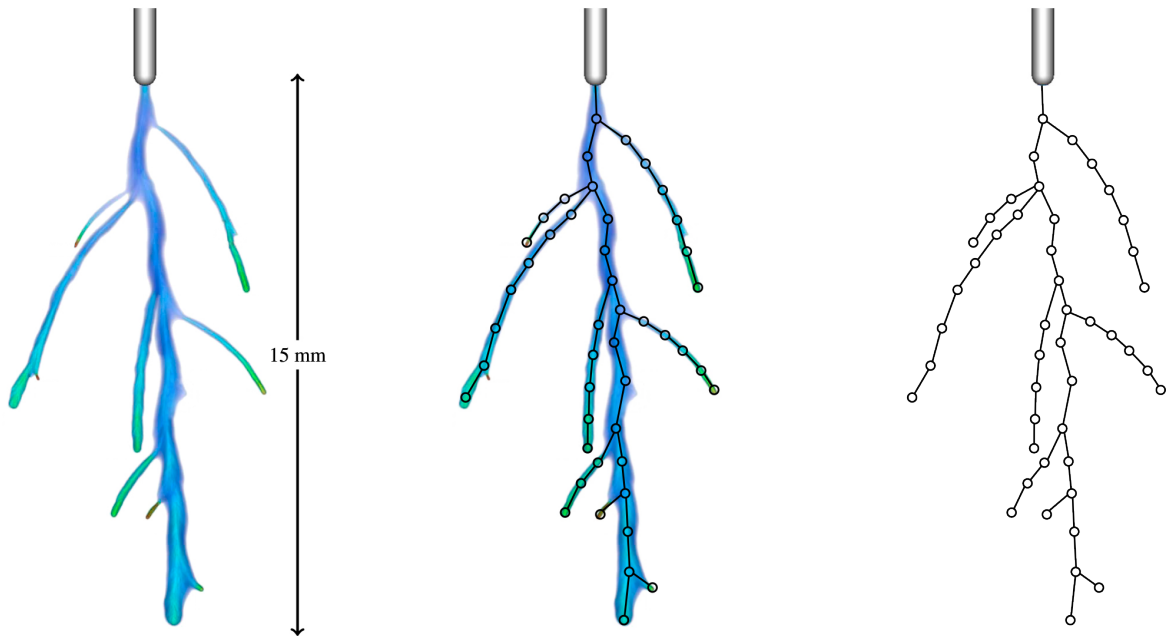
Fig. 1.5 A simulation of a streamer tree (left) and a macroscopic representation as a network of wires (right). Image in the left panel is taken from [19].

on a supercomputer[3]. The computational effort increases drastically as the size and number of branches increase. For applications in atmospheric electricity, streamer trees can be composed of an enormous amount of streamer heads (cf. figure 1.2). Simulating this with the fluid model is practically impossible.

We therefore zoom out one last time and introduce the macroscopic streamer tree model. We remark that the individual filaments are thin and roughly axially symmetric. This allows a substantial simplification without neglecting important physics, namely we represent the streamer tree as a growing network of conducting one-dimensional wires, see figure 1.5. The current flowing through each wire is an approximation of the actual current in the streamer branch. Additionally each wire grows with a velocity equal to that of the streamer. This transforms the streamer tree into a structure of one-dimensional objects. This alternative representation (if one can derive it!) is simulated much more conveniently, which potentially allows us to investigate large and complex streamers trees efficiently.

Macroscopic streamer tree models are appealing, but significant unresolved issues remain. One major challenge is the absence of a fundamental method for the calculation of streamer

---

[3]Computation time is highly dependent on factors such as: simulation settings, number of dimensions considered, performance of the software, the number of cores, *etc*. We can not give one conclusive estimate for the computing time of all simulations. Nevertheless computing times of several days up to a week are not uncommon, even when using powerful supercomputers.

velocities and radii. In fact, this is a classic open question in the field of streamer physics. One of the earliest proposed analytic relations dates back to 1965 [20], although the early works on filamentary discharge propagation go back as early as 1935 [21, 22, 16, 23]. Since then the analytic modelling of streamers has been drastically improved, as is for instance exemplified by the 'order-of-magnitude' approximations of macroscopic parameters [24, 25] (1988) and an approximate velocity-radius relationship [26] (2009). However, some ideas proposed in these earlier works fail to agree with modern numerical simulations. Hence improved models with a proper microscopic basis are needed to give a full quantitative description of the macroscopic parameters of streamers. Without answers to such fundamental questions it is not possible to give a physical basis for macroscopic models, which is why they are only phenomenological at present. In chapters 4 and 5 we focus extensively on these fundamental questions and we derive a new approach to approximating macroscopic parameters, thereby overcoming previous limitations.

1.3   Topics of this thesis

In this thesis we traverse the whole hierarchy of models for streamers as outlined in the previous section. Additionally, in the first two chapters we focus on discharges containing methane (CH_4) as we aim to characterize streamers for plasma-assisted combustion. Our efforts are divided into three parts: the micro-, meso- and macroscopic scales. We start with describing electron scattering with CH_4 and then zoom out to the mesoscopic scale where simulations with particle-in-cell and plasma fluid models are feasible. We then continue on the macroscopic level where we focus on deriving quantitative approximations for macroscopic parameters of streamers, which are also validated against the previously mentioned numerical simulations with a fluid model. These insights culminate in the derivation of an axial model of steady streamers where velocity, radius and other macroscopic parameters are derived from the underlying microphysics. This novel method also forms a stepping-stone for the development of more sophisticated macroscopic models, for instance involving accelerating or branching streamers. In the remainder of this section we shall summarize our research questions in more detail.

On the microscopic scale we address the question:

- **What are the electron scattering cross sections of methane? (Chapter 2)** We review the available literature on this topic and highlight an inconsistency in the data regarding neutral dissociation, e.g. $e + CH_4 \rightarrow e + CH_3 + H$. We show that such processes are

essential to include and explore the validity of phenomenological approximations available in literature.

On the mesoscopic scale we address the question:

- **How do streamers propagate in stoichiometric fuel mixtures? (Chapter 3)** In a stoichiometric fuel mixture there is 9.5% methane, the rest is dry air. We conduct three-dimensional simulations using a particle model to investigate how such concentrations of methane influence positive streamer propagation and branching. Additionally we quantitatively characterize the plasma-chemical activation of the gas by an air-methane streamer, which is relevant for applications involving plasma-assisted combustion.

On the macroscopic scale we address the questions:

- **What are the important macroscopic parameters of a streamer? (Chapter 4)** For the development of accurate streamer tree models, such as discussed in section 1.2.5, we need to know how to describe streamers using only a handful of macroscopic parameters. For the simple case of single positive streamers in air we identify 8 parameters that are important. We investigate how they influence electron dynamics and how they are coupled to each other. We present our model such that we can estimate 4 difficult-to-measure macroscopic parameters based on 4 parameters that are accessible through experimental observation.

- **How to calculate the macroscopic parameters of positive steady streamers? (Chapter 5)** In low electric fields ($\sim 4.5 \, \text{kV cm}^{-1}$ in atmospheric pressure air) streamers can propagate at a constant velocity without changing shape and length. We refer to these as *steady* streamers. We focus on steady streamers because they are a mathematically convenient test case. We derive a macroscopic model for positive steady streamers in air. In order to do so we investigate how to calculate all macroscopic parameters as a function of only the background field E_{bg}, for the special case of positive steady streamers. The main improvement on the approach of Chapter 4 is that we characterize steady streamers without relying on additional input besides the operating conditions (i.e. E_{bg} and gas-specific coefficients).

Chapter 2

Neutral dissociation of methane by electron impact and a complete and consistent cross section set

We present cross sections for the neutral dissociation of methane, in a large part obtained through analytical approximations. With these cross sections the work of Song *et al.* [J. Phys. Chem. Ref. Data, **44**, 023101, (2015)] can be extended which results in a complete and consistent set of cross sections for the collision of electrons with up to 100 eV energy with methane molecules. Notably, the resulting cross section set does not require any data fitting to produce bulk swarm parameters that match with experiments. Therefore consistency can be considered an inherent trait of the set, since swarm parameters are used exclusively for validation of the cross sections. Neutral dissociation of methane is essential to include (1) because it is a crucial electron energy sink in methane plasma, and (2) because it largely contributes to the production of hydrogen radicals that can be vital for plasma-chemical processes. Finally, we compare the production rates of hydrogen species for a swarm-fitted data set with ours. The two consistent cross section sets predict different production rates, with differences of 45% (at 100 Td) and 125% (at 50 Td) for production of H_2 and a similar trend for production of H. With this comparison we underline that the swarm-fitting procedure, used to ensure consistency of the electron swarm parameters, can possibly deteriorate the accuracy with which chemical production rates are estimated. This is of particular importance for applications with an emphasis on plasma-chemical activation of the gas.

2.1   Introduction

2.1.1   Methane-containing plasmas

There are many types of plasma that contain methane (CH_4). Proper models of their properties require cross sections for the collisions of electrons with methane molecules. The present study was particularly motivated by applications such as plasma-assisted combustion of air-methane mixtures, where electron impact dissociation accounts for most of the plasma-produced radicals during the discharge phase [28, 8]. Another combustion-related application is the production of hydrogen fuel through electron impact dissociation, referred to as low-temperature methane conversion [29]. Furthermore, methane plasmas are found in a variety of thin film applications, such as diamond synthesis by plasma-assisted vapour deposition [30]. Other applications range from modelling lightning in methane-containing atmospheres (such as Titan [31, 32]) to studies of carbon-impurities inside a tokamak [33].

2.1.2   Demands on cross sections

Theoretical and computational studies that underlie and enable the aforementioned applications all require a set of cross sections of electron collisions as model input. Although the requirements that are placed on a cross section data set can vary between applications, in general a set is required to be complete and consistent. Within the framework of low-temperature plasma modelling these properties are often defined according to Pitchford *et al.* [34] as:

- *Complete* cross section sets accurately represent all electron energy and momentum losses as well as the electron number changing processes such as ionization and attachment.

- *Consistent* cross section sets are able to reproduce measured values of swarm parameters within an order of ten percent, when used as an input to evaluate the electron energy distribution function from a Boltzmann solver.

Note that these definitions only apply to the behaviour of electron swarms. Other important demands on cross sections, such as the correct approximation of the production rates for chemical species, are not addressed.

When compiling a data set it is often found that experimental data alone is insufficient to ensure completeness and consistency, as data for crucial processes might be missing or measurements from different studies might disagree. The existence of such gaps in the literature can typically be attributed to the challenging nature of measurements for scattering

processes such as: rotational and electronic excitation, dissociative attachment and, most notably, neutral dissociation [35]. Although theoretical cross section calculations can be used to supplement the experiments, such results are often constrained to specific energy ranges and are limited to simple molecules with low atom numbers. Within the framework of low-temperature plasma modelling a common method to overcome the limitations imposed by missing data is to fit presumably incorrect cross sections in order to have better agreement with measured swarm parameters [36], c.f. the IST-Lisbon data set [37]. Such data-fitting techniques are immensely enabling for their ability to produce consistent data sets in the absence of reliable measurements. However by fitting cross section data the scope of applicability of a data set is limited to describing the electron swarm behaviour of a plasma, as the rates of individual processes may have been altered significantly and the resulting cross section set can be non-unique [36, 38, 39]. In other words, plasma models using such *swarm-fitted* data sets are not guaranteed to predict production rates of individual chemical species with a high degree of accuracy.

With an eye on accurately predicting the production of reactive species, it would be a highly attractive property for a cross section set to reproduce swarm parameters without the need for any fitting procedures. For such a set consistency is an inherent trait, i.e. independent of the limitations imposed by the swarm-fitting procedure. This would be especially attractive for applications that focus on the plasma-chemical activation of the gas, since the absence of a fitting procedure gives greater confidence that the individual cross sections are close to their 'true' value. Moreover, an unfitted and consistent cross section set could be used in any plasma-modelling approach (e.g. hydrodynamic, multi-term Boltzmann or Monte-Carlo/PIC).

2.1.3   Goal of the paper

The goal of this paper is to derive cross sections for the neutral dissociation of the ground state of CH_4 by electron impact. Secondly, we want to show that these cross sections in combination with data on other relevant scattering processes in CH_4 produces a complete and consistent data set without the need for any data fitting. Our efforts are documented in two parts: in section 2.2, we will review experimental and theoretical literature on the electron collision cross sections of CH_4. We highlight a gap in the literature corresponding to the neutral dissociation processes. In order to fill in this gap we propose a blend of empirical and analytical cross sections for the neutral dissociation processes in the energy range up to 100 eV. In section 2.3 we show that the addition of our cross sections to the recommendations of Song *et al.* [40] produces a complete and consistent data set *without* the need for any

data-fitting techniques. By performing a Boltzmann analysis in pure methane we show that the agreement between calculated and measured swarm parameters is within error margins.

Finally, in section 2.4 we compare the production of hydrogen species as given by our cross section set and the IST-Lisbon data set [37]. The observed differences underline the issue regarding the non-uniqueness of swarm-fitted cross section sets.

2.1.4   Relation to earlier work

An extensive data evaluation regarding electron scattering with CH_4 was published by Song *et al.* [40]. In their work they recommend cross section values for most of the electron-neutral collisions: momentum-transfer [41–45], vibrational excitation [45], ionization [46] and dissociative electron attachment [47]. However, recommendations for the neutral dissociation processes have explicitly not been made due to inconsistencies in the available data. In section 2.3 we demonstrate, by performing a Boltzmann analysis in pure methane, that simply neglecting these processes results in an ionization rate that is a factor ten larger than experimentally observed (This behaviour has also been documented in [48]). The reason for this is that neutral dissociation processes are an important sink of electron energy that must be incorporated.

Approximations for the missing cross sections of the electron impact dissociation processes are also presented by Gadoum and Benyoucef [48]. In essence, they employ a variation of the approximation technique formulated by Erwin and Kunc [49, 50]. The latter is also thoroughly discussed and evaluated in this study. The variant that Gadoum and Benyoucef [48] have used contains more fitting parameters in their low-energy approximation. Also by reordering the formulae, their variant requires the total (neutral and ionizing) cross sections into CH_3 as an input parameter (which they have obtained from Motlagh and Moore [51]) instead of the total neutral dissociation. To avoid having to discuss two variants of the same approximation technique we have chosen to only include the original approximation technique formulated by Erwin and Kunc [49, 50] in our analysis.

Data for a wider range of hydrocarbon collision processes in a near-wall fusion plasma have been assembled by Janev and Reiter [52, 53]. The interest in that work is the complete breakdown chain of methane, ethane and propane, so including neutral and charged dissociation cross sections for electron impact on C_xH_y with $1 \leq x \leq 3$ and $1 \leq y \leq 2x + 2$. Because of the paucity of data the emphasis in the work of Janev and Reiter, especially in the more recent work [53] for the case of neutral dissociation, is on the development of physically plausible functional forms for the cross sections for all target hydrocarbons. The data in

[52, 53] are valuable and widely used for simulations of fusion plasma with carbon-based wall material where collisions involving many distinct hydrocarbon radical fragments are important. For our application to collisions with CH$_4$ alone the data in [52, 53] are lacking validation and uncertainty estimates, so for us the starting point is Song *et al.* [40] which we supplement with neutral dissociation cross sections validated to swarm data.

2.2 Compilation of unfitted cross sections for neutral dissociation of CH$_4$

We will start by evaluating the literature regarding neutral dissociation. We address the same inconsistencies as were found by Song *et al.* [40], but for energies as high as 100 eV. We then proceed by formulating our approximation for the cross sections of this process. We will lay an emphasis on the energy range of up to 100 eV, relevant for low temperature plasmas. Note that some of our proposed cross sections extend up to 500 eV, however such high energies are not shown because they have a negligible contribution on the computation of swarm parameters in numerical swarm experiments, which we will use to evaluate these approximations in section 2.3.

2.2.1 Neutral dissociation of CH$_4$

The dissociation processes of methane generally occur through electronic excitation of the molecule to an intermediate state[54]. All of the electronically excited states of methane are short-lived and are dissociative or subject to auto-ionization, hence the intermediate electronic excited state can generally be omitted from consideration [40]. For the excitations that lead to neutral dissociation several channels have to be considered

$$e + CH_4 \rightarrow e + CH_4^* \rightarrow \begin{cases} e + CH_3 + \dots & (2.1) \\ e + CH_2 + \dots & (2.2) \\ e + CH + \dots & (2.3) \\ e + C + \dots & (2.4) \end{cases}$$
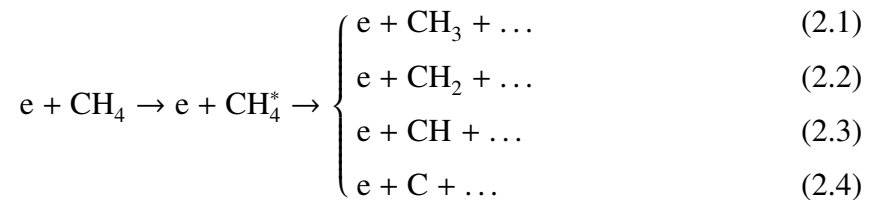
The cross sections of these neutral dissociation processes are denoted by σ_i with i representing the particular dissociated methane fragment: CH$_3$, CH$_2$, etc.

The body of literature regarding the neutral dissociation cross sections is sparse. For instance, no direct measurements below 100 eV exist for σ_{CH} and σ_C. However, cross sections for the neutral dissociation into specific excited states, e.g. CH($A^2\Delta$) and CH($B^2\Sigma^-$), have been
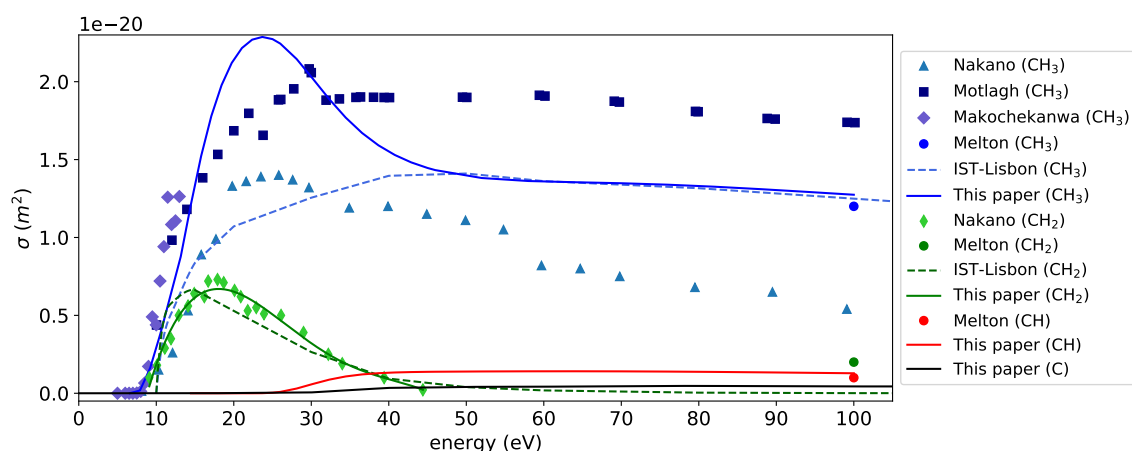
Fig. 2.1 An overview of experimental values for neutral dissociation cross sections of each channel together with the fitted values from IST-Lisbon [37] and our proposed values, within the considered energy range up to 100 eV. The shown measurements are from: Nakano *et al.* [55, 56], Motlagh and Moore [51], Makochekanwa *et al.* [57] and Melton and Rudolph [58]. Note that these measurements do not agree with each other.

(a) CH_3

(b) CH_2
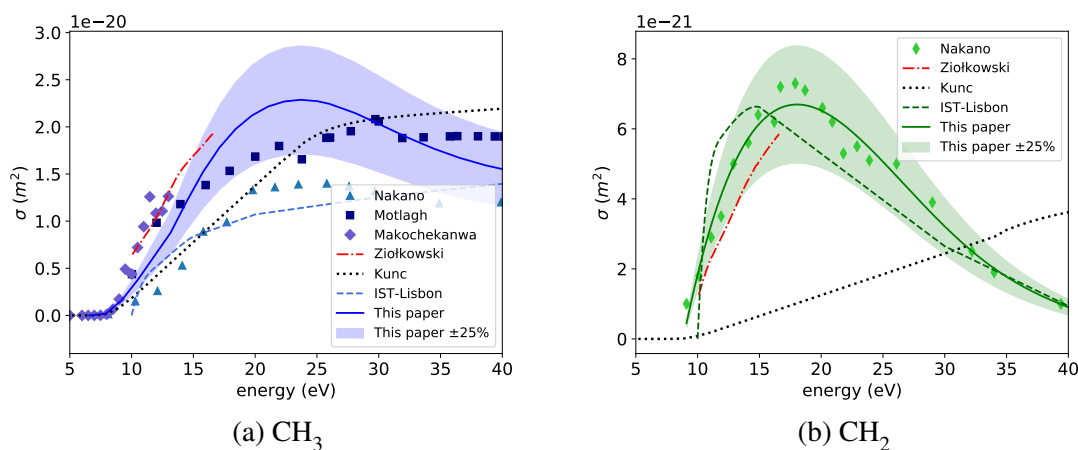
Fig. 2.2 A zoom on the low-energy range of the cross sections of neutral dissociation together with our recommendations (including a ±25% deviation). The shown values are obtained *experimentally*: Nakano *et al.* [55, 56], Motlagh and Moore [51] and Makochekanwa *et al.* [57], *theoretically*: Ziołkowski *et al.* [54], by *semi-empirical approximations*: Erwin and Kunc [49, 50] or by *swarm fitting*: IST-Lisbon [37].

determined by Šašić *et al.* [59]. For the remaining dissociation processes, the experimental observations are in disagreement and theoretical results are only available for a narrow energy range of 10 eV to 16.5 eV. In figure 2.1 we have shown a selection of the experimental results evaluated by Song *et al.* of σ_{CH_3} and σ_{CH_2} for electron energies up to 100 eV. The relative experimental uncertainty accompanying these measurements are ±100% for Nakano *et al.* [55, 56], ±30% for Motlagh and Moore [51] and ±20% for Makochekanwa *et al.* [57]. In this figure we have also supplied the fitted cross sections from the IST-Lisbon data set [37], our recommendations which are derived at the end of this section and the isolated measurements of Melton and Rudolph [58] for σ_{CH_3}, σ_{CH_2} and σ_{CH} at 100 eV. No measure of uncertainty was supplied for the measurements by Melton and Rudolph.

In figure 2.2a we zoom in and compare the values of σ_{CH_3} up to 40 eV from the experimental observations mentioned above with the results from theoretical calculations by Ziołkowski *et al.* [54] and with the approximations from Erwin and Kunc [49, 50]. Note the agreement between recent experimental and theoretical results from Makochekanwa *et al.* [57] and Ziołkowski *et al.* [54] which shows a sharp increasing cross section in the near-threshold region. Based on this agreement and the fundamental nature of their work, Ziołkowski *et al.*[54] conclude that their prediction and the measurements of Makochekanwa *et al.* [57] of σ_{CH_3} are more reliable than the results of Nakano *et al.* [55, 56] and Erwin and Kunc [49, 50]. Furthermore, Ziołkowski *et al.* [54] observe that within their considered energy range, 10 to 16.5 eV, their predictions match with Motlagh and Moore [51]. However when transposing their measured relative cross sections to an absolute scale, Motlagh and Moore only considered neutral dissociation into CH_3. This means that the contributions due to σ_{CH_2}, σ_{CH} and $\sigma_C$ are neglected. Although these cross sections are not known exactly we estimate, based on the measurements of Nakano *et al.* [55, 56], that the cross sections for σ_{CH_2} are considerable in the region between the threshold energy (which can be estimated to lie around 7.5 eV) and 20 eV. For this reason we do not use the measured cross sections for neutral dissociation into CH_3 from Motlagh and Moore [51].

A zoomed-in view of σ_{CH_2} is shown in figure 2.2b. In this case the only experimental observation for energies below 40 eV are reported by Nakano *et al.* [55, 56]. Contrary to their results for σ_{CH_3}, the values of σ_{CH_2} are in excellent agreement with the theoretical predictions from Ziołkowski *et al.* [54] in the near-threshold energy region. Moreover, the approximation by Erwin and Kunc [50] deviates significantly from the aforementioned results, as it does not portray the sharp rise for low energies. This qualitative difference might be attributed to the absence of any data calibration, aside from fixing a threshold energy, of the low-energy (< 50 eV) approximation of Erwin and Kunc [50]. For these reasons,

Ziołkowski *et al.* [54] conclude that their results and the measurements of Nakano *et al.* [55, 56] for the dissociation into CH_2 are more reliable.

2.2.2   Our proposed cross sections

In the previous section it was discussed, relying on the advancements regarding neutral dissociation cross sections in the low-energy regime [57, 54], that the only available measurements for dissociation into CH_3 across a wide energy range (i.e. Motlagh and Moore [51] and Nakano *et al.* [55, 56]) are unsatisfactory.

For this reason we resort to an alternative method to obtain cross sections for neutral dissociation into CH_3, following Janev and Reiter [52] and Erwin and Kunc [49] with support from measurements of Winters [60]. Winters [60] observed that for energies above 50 eV the total dissociation cross section is split equally between neutral and ionizing dissociation, suggesting a common mechanism. Janev and Reiter [52] describe the common mechanism as: "[...] excitation of a dissociative state which lies in the ionization continuum. Autoionization of this state leads to dissociative ionization, while its survival leads to dissociation to neutrals." They conclude from this that cross section branching ratios within the neutral dissociation channel should match cross section branching ratios within the ionized dissociation channel. Erwin and Kunc [49] treat these branching ratios in a similar manner. Therefore, consistent with Janev and Reiter [52] and with Erwin and Kunc [49] we chose to employ for electron impact energies above the threshold for ionizing dissociation the following functional approximation for σ_{CH_3}

$$\sigma_{CH_3} = \frac{\sigma_{ND}}{\sigma_{ID}}(\sigma_{[CH_3^+ + H]} + \sigma_{[CH_3 + H^+]}),$$
$$\text{for } \epsilon \geq \epsilon_c, \tag{2.5}$$

with σ_{ID} the cross section for total ionizing dissociation, σ_{ND} the cross section for total neutral dissociation, $\sigma_{[CH_3^+ + H]}$ and $\sigma_{[CH_3 + H^+]}$ correspond to cross sections of specific ionizing dissociation by electron impact and ϵ_c is the lowest energy at which "reliable" experimental cross sections are available. For ionization processes we adopted the cross sections reported by Lindsay and Mangan [46], as is recommended in Song *et al.* [40]. Furthermore, the value of σ_{ND} can be obtained by subtracting the total ionizing dissociation from the total dissociation

$$\sigma_{ND} = \sigma_{TD} - \sigma_{ID}, \tag{2.6}$$

Table 2.1 The parameters used for the low-energy approximations of our proposed cross sections.

	ϵ_{ND} (eV)	ϵ_b (eV)	ϵ_c (eV)	$\sigma_i^{(2)}(\epsilon_c)$ (m^2)	a (m^2)	p
σ_{CH_3}	7.5	10.5	13.16	$8.8 \cdot 10^{-21}$	$1.5 \cdot 10^{-20}$	1.5
σ_{CH}	15.5	18.5	22.37	$2.9 \cdot 10^{-27}$	$1.3 \cdot 10^{-26}$	1.6
σ_C	15.5	18.5	22.37	$6.8 \cdot 10^{-29}$	$3.1 \cdot 10^{-28}$	1.6

with σ_{TD} the cross section for the total dissociation reported by Winters [60]. Fitting functions reported in Shirai *et al.* [61] were used for σ_{TD}, all ionizing dissociation cross sections, and the dissociative electron attachment cross sections. More details on these fitting functions and their parameters can be found in 2.A. We can recover the initial observation of Winters by taking $\sigma_{ND} = \sigma_{ID}$, which generally holds for energies above 50 eV. Note that the approximation from equation 2.5 only holds for energies above the threshold energies of the corresponding ionizing dissociation reactions.

However, neutral dissociation reactions have a lower threshold energy than their respective ionizing reactions and therefore also occur at energies below the ionization threshold. Thus for energies below the respective ionizing dissociation thresholds we apply the low-energy approximation method of Erwin and Kunc. Here we only present the final result applied to σ_{CH_3} used in our work, for a detailed discussion we refer to the original work [50]. In this method the below-ionization energy range is divided in a near-threshold range, $\epsilon_{ND} \leq \epsilon \leq \epsilon_b$, and a linear-growth range $\epsilon_b \leq \epsilon \leq \epsilon_c$. Here ϵ_{ND} represents the threshold energy for neutral dissociation, ϵ_b represents the energy value separating the near-threshold range from the linear growth range. Then the near-threshold cross section is given by

$$\sigma_{CH_3} = a \left(\frac{\epsilon}{\epsilon_{ND}} - 1 \right)^p,$$
$$\text{for } \epsilon_{ND} \leq \epsilon \leq \epsilon_b, \tag{2.7}$$

with a and p positive constants. For the linear-growth range the cross section are blended with the relation from equation (2.7) as follows

$$\sigma_{CH_3} = \sigma_{CH_3}^{(1)}(\epsilon_b) + \frac{\sigma_{CH_3}^{(2)}(\epsilon_c) - \sigma_{CH_3}^{(1)}(\epsilon_b)}{\epsilon_c - \epsilon_b}(\epsilon - \epsilon_b),$$
$$\text{for } \epsilon_b \leq \epsilon \leq \epsilon_c, \tag{2.8}$$

with blending-parameter $\sigma_{CH_3}^{(1)}(\epsilon_b)$ representing the value of the cross section evaluated at ϵ_b as calculated from equation (2.7), and $\sigma_{CH_3}^{(2)}(\epsilon_c)$ the value of the experimentally-obtained cross section at corresponding energy ϵ_c corresponding to equation (2.5). As can be seen, equations (2.5)-(2.8) determine the cross section for neutral dissociation into CH_3 for the whole energy range.

The cross sections for the neutral dissociation into CH and C are obtained analogously. The values for the parameters ϵ_{ND}, ϵ_b, ϵ_c, $\sigma_i^{(2)}(\epsilon_c)$, a and p used in our work are given in table 2.1. The parameters for σ_C are not covered by Erwin and Kunc [50], but here they are obtained following the same reasoning for the parameters of CH.

Although the approximations defined in equations (2.5)-(2.8) can be used for any of the neutral dissociation channels, they are only used for σ_{CH_3}, σ_{CH} and σ_C. For the remaining neutral dissociation process, σ_{CH_2}, relying on the experimental observations by Nakano *et al.* [55, 56] is preferred over the application of a similar approximation, due to the agreement with theoretical predictions by Ziołkowski *et al.* [54]. Thus, in this study we take σ_{CH_2} to be given by a fourth-order polynomial fit through the measurements of Nakano *et al.*. We refer to 2.A for the fitting parameters.

Our proposed cross sections for the neutral dissociation processes are shown in figures 2.1-2.2b. For σ_{CH_3} the qualitative trend of our proposed cross section is similar to the results from Makochekanwa *et al.* [57] and Ziołkowski *et al.* [54] in the near-threshold energy region, although it appears shifted to higher energies by around 1.5 eV. Our proposed cross sections have a maximum value of $2.29 \cdot 10^{-20}$ m^2 at 24 eV, which is higher than any of the experimental results. After attaining this maximum the value decays and eventually agrees with the isolated measurement of Melton and Rudolph [58] at 100 eV. Note also that for energies above 50 eV our proposed value corresponds to the fitted values from the IST-Lisbon set [37]. Our proposed values for σ_{CH_2}, based on the measurements of Nakano *et al.* [55, 56], vanish for energies above 45 eV. This contradicts with the measurements from Melton and Rudolph [58], which suggest that the cross section should be around $1.95 \cdot 10^{-21}$ m^2 at 100 eV. This difference is also recognized by Nakano *et al.* [55, 56]. To the best of our knowledge, there is currently no straightforward method to reconcile these two observations. Moreover, our proposed cross sections agree (qualitatively) with the fitted counterparts from the IST-Lisbon set [37], although the latter appears to have shifted the peak to lower energies by approximately 4 eV. For σ_{CH} and σ_C there is little literature to compare with aside from observing that our approximation of σ_{CH} agrees with the isolated measurement of Melton and Rudolph at 100 eV. Furthermore, we can compare our values of σ_{CH} with the results for the neutral dissociation into the excited fragments $CH(A^2\Delta)$ and $CH(B^2\Sigma^-)$
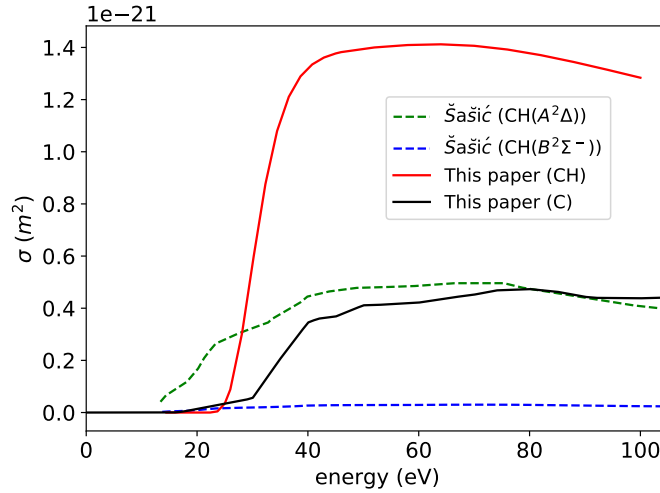
Fig. 2.3 The cross sections σ_{CH} and σ_{C} used in our work alongside the experimentally-derived cross sections into specific excited fragments by Šašić *et al.* [59]. The latter should always be smaller than σ_{CH}. This holds in general, aside from a small discrepancy in the vicinity of the threshold, i.e. below 25 eV.

which have been determined by Šašić *et al.* [59]. It should hold that the dissociation into specific excited fragments is lower than σ_{CH}. As shown in figure 2.3 this behaviour generally holds. Only in the vicinity of the threshold, i.e. below 25 eV, do we observe that the cross sections for dissociation into excited fragments are higher than our proposed value. However, this discrepancy is small compared to the dominant inelastic scattering processes and will therefore be negligible within the context of the swarm experiments that are presented in the following sections.

2.3 Comparison of calculated and measured swarm parameters

Within the framework of low-temperature plasma modelling, a computation of swarm parameters is performed routinely, typically for reduced electric fields (E/N) between 0.1 Td and 1000 Td, with E representing the electric field and N the number density of the gas. In a fluid description of electron swarms (e.g. [62] and references therein) the electrons are described by their density only and this density obeys a reaction-drift-diffusion equation governed by swarm parameters: diffusion coefficient D, mobility μ and by coefficients for ionization α and attachment η. Moreover, the characteristic energy D/μ, reduced mobility μN and reduced Townsend ionization coefficient α/N are functions of the reduced electric

field E/N only (for a not too large electric fields). These swarm parameters can be obtained, given the gas composition and a cross section data set, by solving the Boltzmann equation [63].

In this section we will use the difference between computed and measured swarm parameters as an implicit metric to evaluate the cross sections for neutral dissociation in conjunction with the recommendations from Song *et al.* [40] (neglecting rotational excitations since these are already accounted for in the elastic momentum-transfer cross section). Note that explicit evaluation of the cross sections for neutral dissociation processes is not possible due to disagreement in the available literature, as was shown in section 2.2.1. On the other hand, the swarm parameters of a methane plasma are well-known, with the exception of the attachment coefficient. This can be seen from a compilation made in Alves [37] of measurements containing observations for reduced mobility μN, characteristic energy D/μ, and the reduced Townsend ionization coefficient α/N [64–74]. Assuming that the recommendations by Song *et al.* have a sufficiently low error margin, any disagreement between calculated and measured swarm parameters must imply that the remaining cross sections, i.e. the neutral dissociation processes, are inaccurate. We will compare bulk swarm parameters as computed by a Monte-Carlo solver [75] based on the modelling framework presented in [76]. The simulations are performed at standard temperature and pressure. We emphasize that we show the bulk coefficients and that the characteristic energy is based on the transversal diffusion coefficient. The swarm parameters have been computed for four cross section data sets:

1. the *swarm-fitted* IST-Lisbon database [37],

2. the recommendations by Song *et al.* [40] (lacking any neutral dissociation process),

3. the recommendations by Song *et al.* in conjunction with the original approximations by Erwin and Kunc [49, 50] for neutral dissociation,

4. the recommendations by Song *et al.* in conjunction with our approximations for neutral dissociation.

Moreover, for data set (4) we have included the effect of varying our proposed cross sections for neutral dissociation by ±25%. This results in an upper and lower bound for the reproduced swarm parameters. These bounds define a range which we will refer to as the sensitivity interval. This interval is included to illustrate the effect that possible errors on the cross sections for neutral dissociation might impose on the computed swarm parameters.
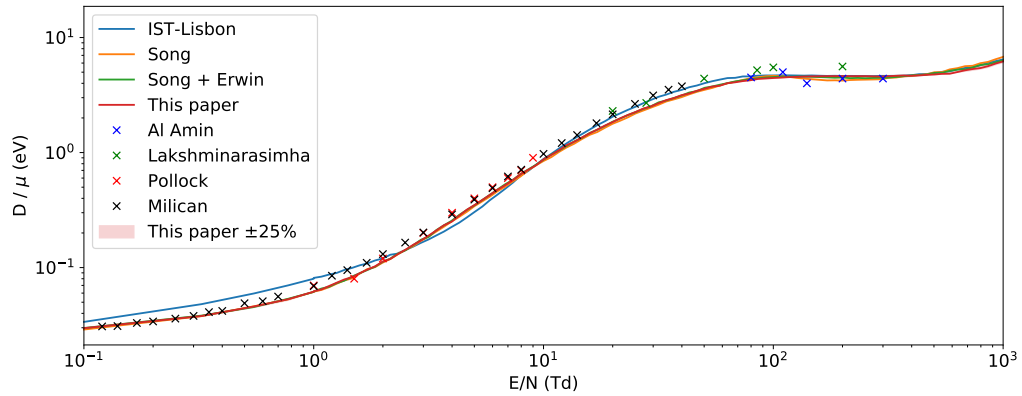
(a) characteristic energy D/μ
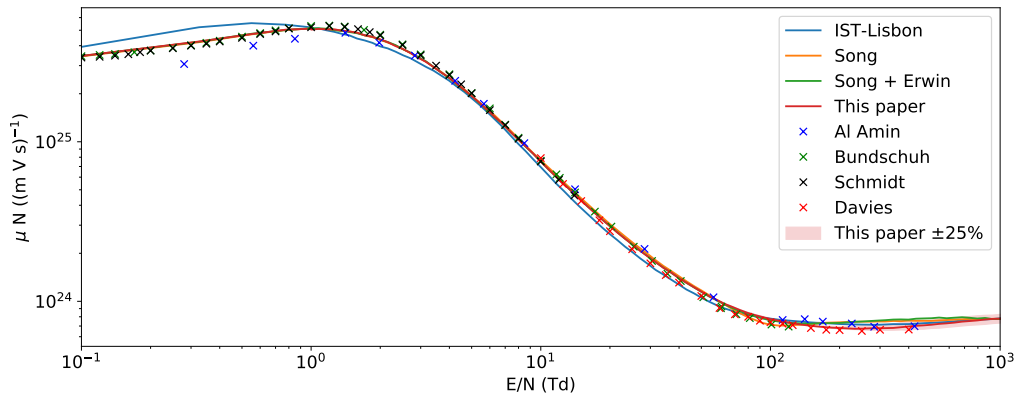
(b) reduced mobility μN
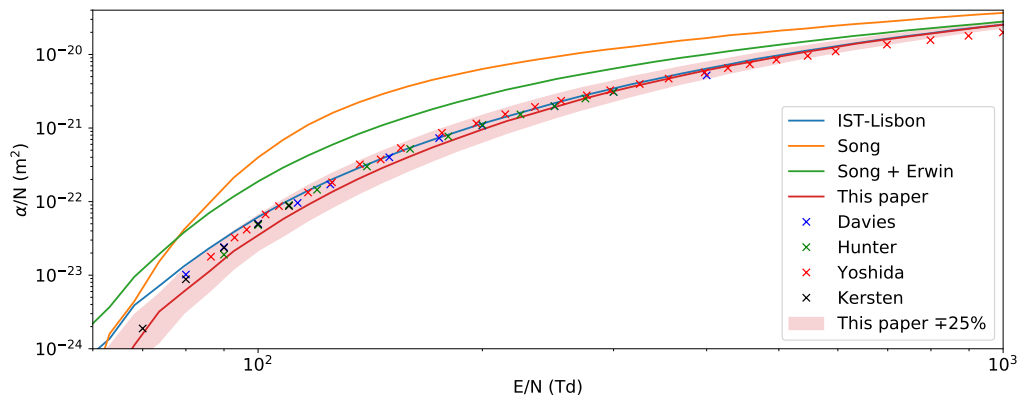
(c) reduced Townsend ionization coefficient α/N

Fig. 2.4 Measured and calculated values of the swarm parameters in pure methane. The shaded red region corresponds to the sensitivity interval, obtained by including a ±25% deviation on the neutral dissociation processes. Overestimating the neutral dissociation leads to underestimating the ionization, and vice versa, hence the use of the '∓' sign in 2.4c. Our cross section set reproduces swarm parameters within a few tens of percent.

In figures 2.4a-2.4c we have respectively shown the characteristic energy, mobility and ionization from numerical and experimental studies on a double logarithmic scale. All of the considered data sets reproduce the characteristic energy within an error margin of 20% and the mobility within an error margin of 7.5%, as can be seen in figures 2.4a and 2.4b. One exception to this can be found at reduced electric fields below 10 Td. Where data set (1) exhibits deviations from the measured values (and the respective error margins) of the characteristic energy (25%) and the mobility (15% between 1 Td and 10 Td and 30% below 1 Td). On the other hand the ionization coefficient, in figure 2.4c, varies strongly between different data sets. Data set (2) overshoots the measured values by as much as a factor of ten. Clearly the neutral dissociation of methane plays a vital role in determining the electron number changing processes and must be incorporated. Even though adding the cross sections for neutral dissociation from Erwin and Kunc reduces this discrepancy, the corresponding data set (3) still exhibits notable discrepancies with measured ionization coefficients. Given the high values of the ionization coefficient it appears that data sets (2) and (3) critically underestimate the sinks for electron energy. This can be explained by considering that the underestimation of energy losses means that an electron is more likely to obtain energies above the ionization potential and subsequently the rate of ionization increases. By inspecting figures 2.2a and 2.2b, one can observe that for electron energies below 25 eV the values from Erwin and Kunc are lower than (most of) the other reported values. This behaviour is especially pronounced for dissociation into CH_2. For swarm experiments in general, the electrons in this energy regime play a dominant role in determining swarm parameters as the abundance of electrons typically reduces strongly for higher electron energies. Therefore the effect of omitting or underestimating the neutral dissociation processes as is done in data sets (2) and (3) can be expected to introduce large discrepancies in the computed ionization coefficient, as is also seen in figure 2.4c.

Such an overestimation of the ionization coefficient is not present for the other considered data sets. The swarm-fitted data set (1) reproduces the ionization coefficient with a maximum deviation of 25% in the region between 100 Td and 800 Td. However below 100 Td the deviations starts to increase. For instance, at 90 Td this deviation exceeds 40%. The large accuracy between 100 Td and 800 Td is to be expected from data sets which employ fitting procedures to ensure completeness and consistency. At 1000 Td the deviation is around 35%. The reproduction of the ionization coefficient is also observed for our approximations in conjunction with Song *et al.*, data set (4), with a maximum deviation up to 35% (at 100 Td). This is somewhat larger than observed for data set (1). For reduced electric fields below 100 Td our reduced Townsend ionization coefficient is closer to measurements than data set (1). Notably, up to 500 Td it can be observed that our reduced Townsend ionization

(a) Low E/N (b) High E/N
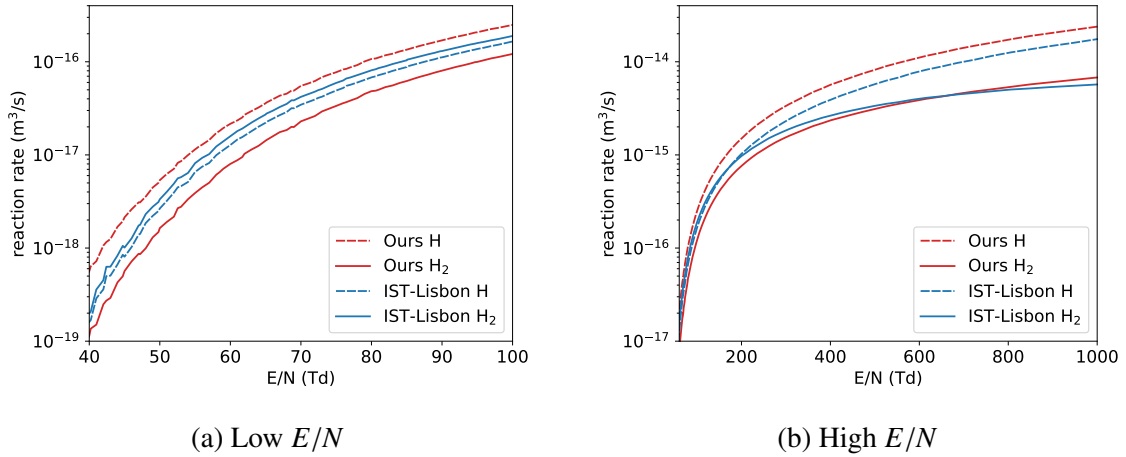
Fig. 2.5 The predicted reaction rates for the production of the hydrogen species H and H_2 for the (swarm-fitted) IST-Lisbon set and Ours (unfitted). Although both cross section sets can be considered consistent (which refers to behaviour of electron swarms only), they exhibit clear differences in the prediction of hydrogen species production.

coefficient is consistently lower than experimentally observed ionization coefficient. This indicates, if one assumes that the ionizing cross sections are sufficiently accurate, that the sum of all non-ionizing inelastic cross sections used here is probably an overestimation.

Furthermore, from the sensitivity interval corresponding to data set (4) we can conclude that the reproduction of characteristic energy and mobility is almost completely independent of the neutral dissociation processes. In contrast, the sensitivity interval for the ionization coefficient shows a significant spread. This again underlies that neutral dissociation processes are an important electron energy sink, at least within the context of low-temperature plasmas. Moreover, the measured values of the reduced Townsend ionization coefficient lie within the sensitivity interval, indicating that a small adjustment ($< 25\%$) of the proposed cross sections can account for the observed deviations regarding this swarm parameter.

2.4 Production rates for hydrogen radicals

In the previous section we have introduced two consistent data sets: IST-Lisbon (1) and Ours (4). The fundamental difference between these two sets is that (4) is unfitted and consistent, whereas (1) employs a fitting procedure to ensure reproduction of swarm parameters. The use of such data-fitting techniques has already been discussed in section 2.1.2. Here we will illustrate how both data sets predict the production of atomic and molecular hydrogen by inspecting the sum of the reaction rates of hydrogen-producing electron collisions as

calculated by a Monte-Carlo solver [75] based on the modelling framework presented in [76]. The simulations are performed at standard temperature and pressure.

In order to make such a comparison we need ratios regarding the by-products of dissociative electron collisions. However, such data is virtually non-existent. For example: there are no cross sections which distinguish the neutral dissociation processes

$$e + CH_4 \rightarrow \begin{cases} e + CH_2 + H_2 & (2.9) \\ e + CH_2 + 2H & (2.10) \end{cases}$$
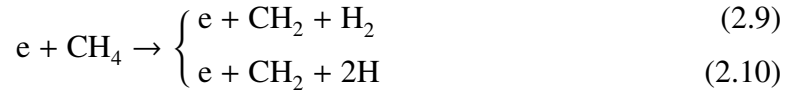
It is known that the dissociation energy of the relatively strong hydrogen bond is 4.52 eV, therefore it can be expected that due to this additional energy barrier the reaction rate of equation (2.10) will be lower than equation (2.9). However, without direct observations such arguments will always remain qualitative. For the current purpose of comparing the radical yields of the two data sets, we will assume that the composition of hydrogen products will always be in the lowest energy state. In other words, we assume that reactions like equation (2.10), which requires additional energy for dissociation, will not occur. The effect is that we will underestimate atomic hydrogen yield, and subsequently overestimate the production of molecular hydrogen.

With this assumption, the reaction rates for hydrogen production have been calculated for both data sets; they are shown in figure 2.5. It can be seen that data set (1) predicts atomic hydrogen yields, approximately 35% lower than (4) above 100 Td. Similar deviations are also observed for the molecular hydrogen production. For instance, above 100 Td the maximum deviation is 45%. However, for reduced electric fields below 100 Td the deviations between the predictions of production rates for molecular hydrogen are increasing. For instance, at 50 Td data set (1) predicts a molecular hydrogen yield which is 125% higher than data set (4). For atomic hydrogen we find a difference around 50% at 50 Td.

These deviations between the production rates of chemical species of two consistent sets clearly illustrate the non-uniqueness of swarm-fitted data sets. Whether the errors on the production rates for chemical species introduced by relying on data-fitting are tolerable is always dependent on the application and the extent of adjustments performed. However, given the highly reactive nature of atomic hydrogen and the nonlinear nature of plasma-chemical applications, such deviations have to be treated with care.

2.5   Summary and outlook

2.5.1   Summary

The main contribution of this article are the cross sections for the neutral dissociation of the ground state of CH_4 by electron impact. Secondly, we have used these values to arrive at a complete and consistent cross sections for electron collisions with methane for reduced electric fields between 0.1 Td and 1000 Td, without relying on any data-fitting techniques. This data set is largely based on the recommendations of Song *et al.* [40], with the addition of a blend of empirical and analytical cross sections for the remaining neutral dissociation processes.

Furthermore this work includes a Boltzmann analysis using a Monte-Carlo solver. We have shown that the presented set of cross sections reproduces measured swarm parameters with maximum deviations of: 35% for ionization, 7.5% for mobility and 20% for characteristic energy.

The presented cross section set distinguishes itself from other data sets by not relying on any data-fitting techniques to ensure consistency. This feature makes our cross section set independent of the limitations imposed by the swarm-fitting procedure. This can be especially attractive for applications that focus on plasma-chemical activation of the gas, such as plasma-assisted vapour deposition, low-temperature methane reforming, etc. Moreover, the absence of any data fitting means that the presented cross section set can be used in a variety of plasma-modelling approaches (e.g. hydrodynamic, multi-term Boltzmann or Monte-Carlo/PIC).

2.5.2   Outlook

The validity of the cross sections proposed in this work has been considered by comparing measured and calculated swarm parameters. In principle this is an implicit metric, since the set of cross sections as a whole is considered as opposed to individual cross sections. However, in section 2.3 we have assumed that the recommendations of Song *et al.* [40] have a sufficiently low error margin such that deviations in the reduced Townsend ionization coefficient can be primarily attributed to the proposed cross sections for neutral dissociation. Although this assumption enables much of the steps taken in this work, it does not give explicit certainty. One way to improve on this is by studying the swarm parameters of mixtures of methane with rare gases [36]. For example, the swarm parameters in Ar-CH_4 mixtures are studied by Sebastian and Wadehra [77]. Still, benchmark experiments for

individual cross sections remain highly desirable if the difficulty of diagnosing neutral radical fragments can be overcome.

On the side of computation it would be very desirable to see work in the style of Ziołkowski *et al.* [54] (based on R-matrix calculations of electron excitation of methane followed by quasi-classical trajectory simulations with surface hopping) extended to higher electron collision energy than 17 eV. The work of Brigg *et al.* [78] highlights some electronic structure issues with these computations and in particular they recommend a multi-reference configuration interaction approach to deal with the multiply-excited target states that are important at high impact energy. (However, the neutral dissociation cross section calculations in Brigg *et al.* [78] are limited to electron impact energies below 15 eV and they do not supplant the results from Ziołkowski *et al.* [54]). Such R-matrix calculations and trajectory simulations would naturally predict branching ratios between 2H and H_2 channels as well, although an assessment of the importance of zero-point energy (quantized vibrational energy in molecular fragments) should be made. However, there are tools (such as ring polymer Molecular Dynamics [79]) to incorporate this quantum effect into trajectory calculations.

Appendix 2.A   Fitting functions and parameters

The cross sections for total neutral dissociation, all dissociative ionization processes, and dissociative electron attachment were obtained from fits through the data points reported in tables by Song *et al.* [39]. The functions used were those reported in Shirai *et al.* [61]. The fitting parameters were obtained again for this paper.

2.A.1   Basis functions

Shirai *et al.* [61] used 3 basis functions from which the fitting functions were created

$$f_1(x) = \sigma_0 a_1 \left(\frac{x}{\epsilon_R}\right)^{a_2}, \tag{2.11}$$

$$f_2(x) = \frac{f_1(x)}{\left[1 + \left(\frac{x}{a_3}\right)^{a_2+a_4}\right]}, \tag{2.12}$$

$$f_3(x) = \frac{f_1(x)}{\left[1 + \left(\frac{x}{a_3}\right)^{a_2+a_4} + \left(\frac{x}{a_5}\right)^{a_2+a_6}\right]}, \tag{2.13}$$

with $\sigma_0 = 1 \cdot 10^{-20}$ m^2, $\epsilon_R = 1.361 \cdot 10^{-2}$ keV (Rydberg constant), and a_i the parameters which will be obtained for each specific reaction by fitting the data points.

Fig. 2.6 The cross sections of the dissociative ionization reactions of CH_4. The solid lines are the result of fitting equation (2.14) to the tabulated cross sections for these reactions from Song *et al.* [39] which are represented by filled circles in the same color.

Table 2.2 Parameters obtained by fitting equation (2.14) to the tabulated cross sections of Song *et al.* [39] for dissociative ionization reactions

	ϵ_{th} (eV)	a_1	a_2	a_3	a_4	a_5	a_6
CH_3^+	12.63	5.5333	2.7119	0.0071	-0.2619	0.0194	0.8917
CH_2^+	16.20	0.2575	2.9997	0.0141	-0.2828	0.0289	1.0172
CH^+	22.20	0.295	3.4235	0.0207	0.9925	0.0100	-0.5789
C^+	22.00	0.0392	4.6413	0.0243	1.1558	0.0125	-0.7372
H_2^+	22.30	0.0134	5.0600	0.0147	-0.7746	0.0242	1.0240
H^+	21.10	0.0985	2.7831	0.0210	-0.6691	0.0403	1.0503

2.A.2   Dissociative Ionization

The fitting function reported by Shirai *et al.* [61] to be used for the dissociative ionization reactions is the following

$$\sigma_i(\epsilon) = f_3(\epsilon_1),\tag{2.14}$$

with ϵ the incident electron energy in keV, $\epsilon_1 = \epsilon - \epsilon_{th}$, and ϵ_{th} the threshold energy of the reaction in keV. Equation 2.14 was fitted through the tabulated cross sections and threshold energies for the dissociative ionization reactions reported in Song *et al.* [39]. The used data points and resulting fits are shown up to 100 eV in figure 2.6. The fitting parameters are tabulated in table 2.2
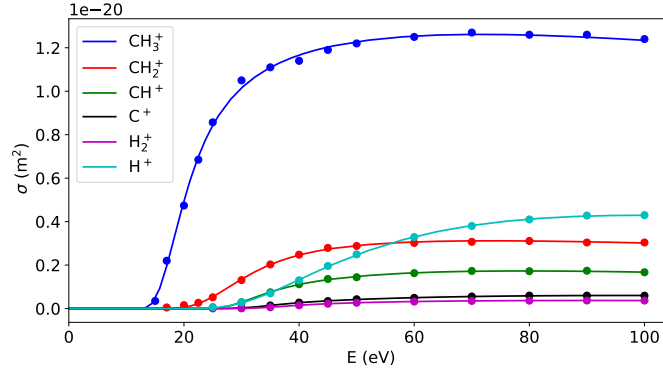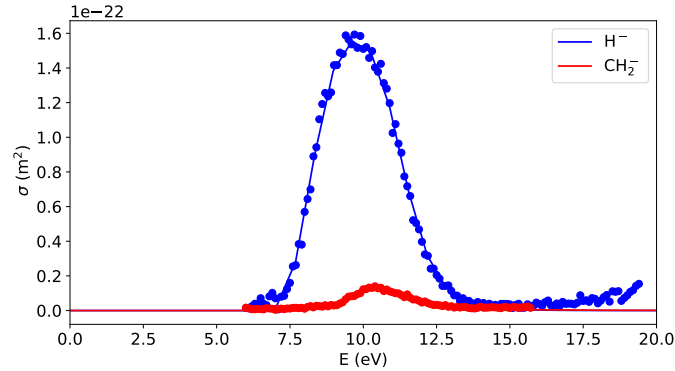
Fig. 2.7 The cross sections of the dissociative electron attachment reactions of CH_4. The solid lines are the result of fitting equation (2.14) to the tabulated cross sections for these reactions from Song *et al.* [39] which are represented as filled circles in the same color.

Table 2.3 Parameters obtained by fitting equation (2.14) to the tabulated cross sections of Song *et al.* [39] for dissociative electron attachment

	ϵ_{th} (eV)	a_1	a_2	a_3	a_4	a_5	a_6
H^-	6.0	128.0817	5.0736	0.0024	0.1908	0.0041	10.1747
CH_2^-	6.0	1.5496	$3.1405 \cdot 10^{-5}$	0.0012	4.8957	0.0164	-4.8826

2.A.3 Dissociative Electron Attachment

Shirai *et al.* [61] use the same fitting function for dissociative ionization, equation (2.14), as for fitting the dissociative electron attachment cross sections (including the same definition for ϵ_1). We use this fitting function to fit the tabulated cross sections for dissociative electron attachment reactions from Song *et al.* [39]. The fits and corresponding data points are shown in figure 2.7 and the fitting parameters are reported in table 2.3.

2.A.4 Total Dissociation

The fitting function for the total dissociation used by Shirai *et al.* [61] is given by

$$\sigma_{\text{TD}}(\epsilon) = f_2(\epsilon_1) + a_5 \cdot f_2\left(\frac{\epsilon_1}{a_6}\right), \tag{2.15}$$

where ϵ_1 again has the same definition as for equation (2.14). The total dissociation cross section was measured by Winters [60] and Perrin *et al.* [80]. We have obtained data points for both measurements by extracting them from the published graphs using WebPlotDigitizer [81]. The fits and the data points for both measurements as well as equation (2.15) using
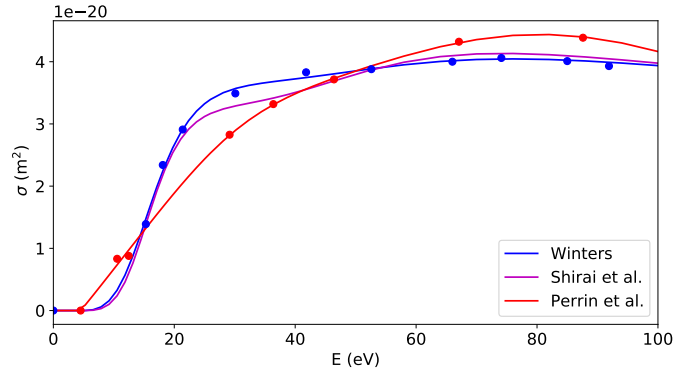
Fig. 2.8 The total dissociation cross sections as measured by Winters [60] (filled blue circles), and by Perrin *et al.* [80] (filled red circles). The solid lines in the same colors as the measurement points are the fits done in this paper using equation (2.15). The solid line of Shirai *et al.* [61] is obtained by using their reported fitting parameters with equation (2.15).

Table 2.4 Parameters obtained by fitting equation (2.15) to the measured cross sections of Winters [60] for total dissociation.

ϵ_{th} (eV)	4.51
a_1	4.1200
a_2	3.0594
a_3	0.0142
a_4	0.3606
a_5	0.4630
a_6	3.8830

the fitting parameters reported by Shirai *et al.* [61] for total dissociation are shown in figure 2.8. Deviations up to 20% can arise due to different fitting parameters and fitted data points. These deviations in the total dissociation will propagate to the cross sections of the individual neutral dissociation reactions. Increasing the cross section of the neutral dissociation cross sections has the effect of reducing the Townsend ionization coefficient α. In this paper we have used the data points of Winters [60] and the fitting parameters as reported in table 2.4.

2.A.5   Neutral Dissociation to CH$_2$

In this paper we have taken the measured cross sections for neutral dissociation into CH$_2$ from Nakano *et al.* [55, 56]. To smooth the data we have fitted a fourth order polynomial
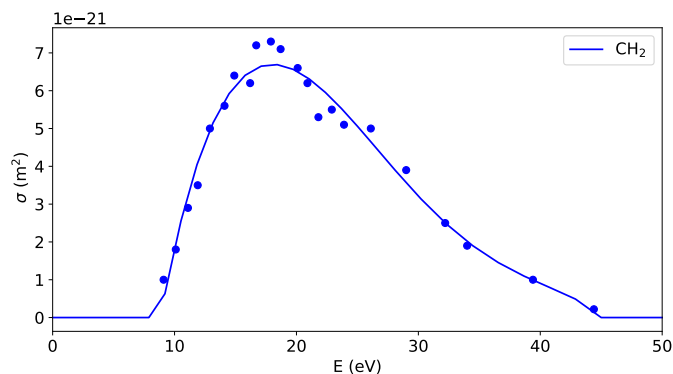
Fig. 2.9 The cross sections for neutral dissociation to CH_2 as measured by Nakano *et al.* [55, 56] and the corresponding fit obtained by equation (2.16) combined with the fitting parameters in table 2.5

Table 2.5 Parameters obtained by fitting equation (2.16) to the measured cross sections of Nakano *et al.*[55, 56] for neutral dissociation to CH_2

a_0	$-3.0203 \cdot 10^{-20}$
a_1	$5.4772 \cdot 10^{-21}$
a_2	$-2.8119 \cdot 10^{-22}$
a_3	$5.8213 \cdot 10^{-24}$
a_4	$-4.3221 \cdot 10^{-26}$

through the data points

$$f(\epsilon) = a_0 + a_1\epsilon + a_2\epsilon^2 + a_3\epsilon^3 + a_4\epsilon^4, \tag{2.16}$$

with fitting parameters a_i, and ϵ the incident electron energy in eV. Note that this function is only valid within the bounds of the measurement energies i.e. $9.1 \text{ eV} \leq \epsilon \leq 44.4 \text{ eV}$. The fit and the corresponding data points are shown in figure 2.9. The fitting parameters are reported in table 2.5.

Chapter 3

3D particle simulations of positive air-methane streamers for combustion

Streamer discharges can be used as a primary source of reactive species for plasma-assisted combustion. In this research we investigate positive streamers in a stoichiometric air-methane mixture at 1 bar and 300 K with a three-dimensional particle-in-cell model for the electrons. We first discuss suitable electron scattering cross sections and an extension of the photoionization mechanism to air-methane mixtures. We discuss that the addition of 9.5% methane leaves electron transport and reaction coefficients essentially unchanged, but it largely suppresses photoionization and shortens the photon mean free path. This leads to (1) accelerated streamer branching, (2) higher electric field enhancement at the streamer head, (3) lower internal electric fields, and (4) higher electron densities in the streamer channel. We also calculate the time-integrated energy density deposited during the evolution of positive streamers in background electric fields of 12.5 and 20 kV cm^{-1}. We find typical values of the deposited energy density in the range of $0.5 - 2.5$ kJ m^{-3} within the ionized interior of streamers with a length of 5 mm; this value is rather independent of the electric fields applied here. Finally we find that the energy deposited in the inelastic electron scattering processes mainly produces reactive nitrogen species: N_2 triplet states and N, but also O and H radicals. The production of H_2 and O_2 singlet states also occurs albeit less pronounced. Our calculation of the primary production of reactive species can for example be used in global chemistry models.

3.1   Introduction

Streamers are transient gas discharges consisting of growing plasma filaments with field enhancement at the tip. A review covering a wide range of investigations into streamer dynamics is presented in [9]. In industry, mainly positive streamer discharges are found in a variety of applications such as: plasma medicine [6], industrial surface treatment [5] and air-pollution control [83]. In particular, positive streamers in combustible mixtures are relevant for plasma-assisted combustion, as will be discussed in section 3.1.2.

3.1.1   Streamer dynamics in varying gases

The properties of streamers are determined by the electron dynamics which in turn are governed by gas-specific photoionization, and by transport and reaction coefficients. There are numerous investigations on streamers in different gases which illustrate this gas-dependency, for example: CO_2 [84], N_2:CH_4 [32], air with artificially increased electron attachment or reduced photoionization [85, 86], N_2-O_2 mixtures in various ratios [76, 87], the atmospheres of Venus and Jupiter [88], and mixtures resembling the atmosphere of the primordial Earth [89].

Specific to N_2-O_2 mixtures it was shown experimentally that streamers tend to branch more frequently for decreasing oxygen concentrations [1, 90]. Decreasing the oxygen concentration gives different photoionization characteristics due to a longer photon mean free path, while the number of photoionization events stays essentially unchanged. In mixtures with low oxygen concentrations ($< 0.2\%$) stochastic fluctuations associated with the discrete nature of photoionization then accelerate branching.

In an air-methane mixture, however, methane largely absorbs photons without ionizing, and it also quenches excited N_2 that otherwise could emit photons. So the rate of ionizing photoabsorption decreases, and the photon mean free path decreases as well [91]. As we will show, these two effects combined also enhance the stochastic fluctuations in the leading edge of the streamer. In simulations where the single-electron dynamics in the leading edge are sufficiently resolved (e.g. in a 3D PIC-MCC model) this will ultimately accelerate streamer branching.

3.1.2   Plasma-assisted combustion

In plasma-assisted combustion there is an interest in positive streamers propagating through combustible mixtures, such as air-methane [28, 8, 92]. In a streamer discharge one finds

electrons with energies that exceed the gas temperature by orders of magnitude. These energetic electrons produce excited nitrogen states, hydrogen- and oxygen-radicals, fuel fragments and other reactive species through collisions with neutral gas molecules. The resulting non-equilibrium distribution of reactive species is then available for plasma- and combustion-chemical processes taking place on slower time scales. These processes have been studied numerically. For instance in [91] the effect of a streamer discharge on the reduction in ignition delay was studied with an axisymmetric fluid model. In [93, 94] a two-dimensional cartesian fluid approach was used to investigate radical production by streamers in air-methane (without correcting the photoionization). In [95] a similar model was used (2D cartesian without correcting the photoionization and also without electron attachment) to investigate the production of radicals for air-methane streamers at 10 bar and 600 K. An overview of multiscale modelling for plasma-assisted combustion is presented in [96]. Finally a comparison between 0D and axisymmetric models for the simulation of air-methane streamers (without photoionization) is presented in [97]. The application of low-temperature plasmas is found to have favourable effects such as: ultra-lean combustion for emission reduction [98], increased flame propagation speed [99, 100] and flame stabilization [101]. In a single-pulse discharge the generation of reactive species can, under the right conditions, lead to a reduction of ignition delay time [102].

3.1.3   Content of the paper

We simulate positive streamers in a stoichiometric air-methane mixture at 1 bar and 300 K in background electric fields of 12.5 kV cm^{-1} and 20 kV cm^{-1} in an 8 mm gap. Such conditions are relevant for the initial stages of plasma-assisted ignition. We will analyze the simulations from two different viewpoints. First we will analyze how the addition of methane affects the fundamental properties of the discharge, such as streamer branching, electric field enhancement and electron densities and energies. Second, we analyze the streamer discharge within the context of plasma-assisted combustion. We will study the deposited energy density and the G-values, i.e. the efficiency with which primary reactive species are produced. The production of these primary species can represent an initial condition of plasma-chemical and ignition-chemical calculations.

In section 3.2 we describe the particle-in-cell model, cross section sets, simulation conditions and we correct for the suppressing influence of CH_4 on the photoionization mechanism. In section 3.3 we compare the dynamic properties of a positive streamer in air and air-methane. Finally, in section 3.4 we address the plasma-chemical activation of a stoichiometric air-methane mixture by a positive streamer.

3.2 Simulation method

We simulate a positive streamer discharge using a 3D Particle-In-Cell model with Monte-Carlo Collisions (PIC-MCC). Our implementation is based on the model described in [76]. Here we present a short summary and describe the photoionization model used for discharges in air-methane mixtures.

3.2.1 Description of PIC-MCC model

Within a PIC-MCC model electrons are represented by super-particles. One super-particle represents a variable number of physical electrons, represented by the weight w as is further elaborated in section 3.2.2. The motion of electrons is then governed by an acceleration due to the electric field combined with isotropic scattering processes due to collisions with the gas molecules. Ions are included as a density and are assumed to be immobile on the considered short streamer time scale. The neutral gas particles are taken as a homogeneous background density with which the electrons can stochastically collide. Electron collisions with ions, excited/dissociated molecules and other electrons can be omitted since the ionization degree is low, around 10^{-4} to 10^{-5}.

An advantage of a PIC-MCC model over the conventional fluid models is that the electron energy distribution function (EEDF) is approximated explicitly and without the need for assumptions such as the local field approximation. For plasma-chemical streamer applications a good approximation of electron energies is important as this quantity determines the production rate of reactive species. Another advantage of using PIC-MCC models is that it is better equipped to deal with single-electron fluctuations. In air, it is known that electron density fluctuations, in particular due to stochastic photoionization, accelerate streamer branching [86, 103, 18]. In the case of air-methane mixtures there is less photoionization and the photon mean free path is shorter (see section 3.2.4). As a result single-electron fluctuations occur in the active zone, i.e. the region where the electric field is above breakdown. In order to properly resolve the influence of these single-electron fluctuations we perform simulations with the PIC-MCC model.

The main drawback of PIC-MCC models is a high computational cost associated with the use of a large number of particles, especially in three dimensions. For example, typical computing times for our simulations are on the order of days (performed on one node of Cartesius, the Dutch national supercomputer), whereas a two-dimensional fluid simulation performed on an 'average' desktop typically only requires several minutes of computation. More details about such a comparison are found in the appendix of [18].

3.2.2   Particle weight

In a streamer discharge the number of free electrons increases rapidly to the point where it becomes computationally infeasible to simulate every electron individually. To overcome this limitation the weight ($w \geq 1$) of a computer particle is dynamically updated, thereby allowing one particle to represent one or many physical electrons. This technique, called *adaptive particle management*, ensures that the computational complexity of the simulation remains tractable at the cost of an artificial noise on the electron density. Details on the implementation and performance of this algorithm can be found in [104]. The central idea is that particles are merged and/or split between time steps, thereby changing their weights in order to bring them close to a desired weight w_d

$$w_d = \frac{n_e \Delta x^3}{N_{\text{ppc}}},$$ (3.1)

where n_e is the local electron density, Δx^3 is the volume of the cell containing the particle and N_{ppc} is the desired number of particles per cell, which we have chosen at 100.

Now we focus on the influence of artificial noise introduced by super-particles before estimating that for our parameters this effect is small. To that end we note that electron density fluctuations accelerate branching. This was shown, for example, in [103] using a stochastic fluid model. A similar conclusion was drawn in [86] and later in [18] by combining a conventional fluid model with a stochastic version of the Zhelezniak photoionization model. Therefore with super-particles (with $w > 1$) it is inevitable that electron density fluctuations are more prevalent compared to using only single particles ($w = 1$). As a result streamer branching would occur more often, especially when compared with fluid models which neglect physical density fluctuations. However, by choosing a small cell volume and a high N_{ppc} one can ensure that the artificial noise introduced by super-particles does not dominate the fluctuations introduced by physical mechanisms in the leading edge (such as photoionization). For example, in our simulations the smallest cell volume, which is used in the high-field region at the streamer head, equals $(4.0\,\mu\text{m})^3$. Thus electron avalanches on the finest grid with densities below $1.6 \cdot 10^{18}$ m^{-3} are simulated using particles with unit weight. In section 3.3.1 we show that this is sufficiently accurate in order to resolve the single-electron fluctuations in the leading edge.

3.2.3   Cross sections for electron collisions

A set of cross sections for the dominant scattering processes is required to describe the electron kinetics. Many of the available sets have adjusted individual cross sections in
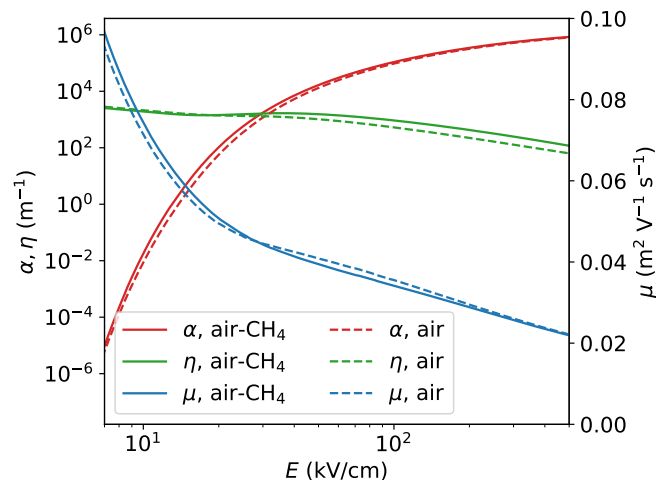
Fig. 3.1 The transport and reaction coefficients for air and stoichiometric air-methane at 1 bar and 300 K. The axis for the mobility μ is linear, whereas the axis for ionization and attachment coefficients α and η, respectively, is logarithmic. We conclude that a gas fraction of 9.5% CH_4 introduces only minor changes to these coefficients.

order to ensure that electron transport and reaction coefficients are correctly reproduced in numerical swarm experiments. A downside of this procedure is that adjusting cross sections can lead to incorrect reaction rates. Thus the swarm-fitting procedure is limited by non-uniqueness [36], since different modifications to inelastic cross sections can result in the same swarm parameters but with different reaction rates. In Chapter 2, we defined an unfitted cross section set and addressed the issue of non-uniqueness for the case of CH_4.

Given our focus on accurately predicting the produced reactive species we only use unfitted cross section sets. For N_2 we adopt the cross section set of Kawaguchi *et al.* [105], but neglect the inter-rotational (de-)excitation which is only relevant at low reduced electric fields. For O_2 we adopt the cross sections recommended by Itikawa *et al.* [106]. Electron attachment by three-body collisions with O_2 are taken from [107]. For CH_4 we adopt the cross section set proposed in Chapter 2 which are based on the recommendations by Song *et al.* [108] combined with cross sections for the neutral dissociation processes. Finally, all scattering processes are assumed to be isotropic.

For a stoichiometric air-methane mixture (71.5% N_2, 19% O_2 and 9.5% CH_4) at 300 K and 1 bar we compared the ionization and attachment coefficients α, η and the electron mobility μ with air, in figure 3.1. These coefficients are calculated using BOLSIG+ (desktop version of 2019) using the temporal growth setting and assuming isotropic scattering [14, 109]. This relatively small fraction of CH_4 introduces only minor quantitative differences. Furthermore,

we remind the reader that the coefficients depicted here are only used for the purpose of illustration. Within a PIC-MCC model the electron kinetics is directly determined by the cross sections.

3.2.4   Photoionization in air-methane mixtures

Naidis [91] approximated the influence of CH_4 on photoionization in air-methane by including an extra absorption factor in the classical Zhelezniak photoionization model [13]. In that work, however, no corrections were made for the changing effective quenching pressure due to the addition of methane. An alternative to the Zhelezniak photoionization model (in air) is discussed in [19, 110]. Here we follow the reasoning of [91] as we extend the Monte-Carlo Zhelezniak photoionization model, such as presented in [76, 111], to air-methane mixtures. We formulate necessary corrections to include photon-loss due to non-ionizing photoabsorption and, notably, quenching.

Quenching:

In dry air, it is well-established that radiative transitions of excited states of N_2 emit photons in the energy range that is associated with the photoionization of O_2, namely $12.1 - 12.65$ eV. On the contrary, the excited states of CH_4 are all dissociative [108] and do not emit photons with energies that can ionize O_2. Thus, photons in the relevant energy range are produced in air-methane mixtures only by the excited states of N_2. However, CH_4 does suppress the total number of photons by quenching the excited states of N_2. The effective quenching pressure p_q^{eff} can be written as

$$\frac{1}{p_q^{\text{eff}}} = \frac{\chi^{O_2}}{p_q^{O_2}} + \frac{\chi^{N_2}}{p_q^{N_2}} + \frac{\chi^{CH_4}}{p_q^{CH_4}}, \tag{3.2}$$

where χ denotes the respective gas number fraction. The quenching pressures are reported in [112] to be: $p_q^{O_2} = 3.8$ torr, $p_q^{N_2} = 91$ torr and $p_q^{CH_4} = 1.8$ torr. According to the Zhelezniak model, the average number of photons $\bar{\eta}$ produced per impact ionization of an air molecule (i.e. N_2 or O_2) is given by

$$\bar{\eta} = \frac{p_q^{\text{eff}}}{p_q^{\text{eff}} + p} \xi, \tag{3.3}$$

with the pressure p and the factor ξ relating the radiative de-excitation rate of N_2 to the ionization rate. The dependence of ξ on the local electric field is only partially tabulated in [13], so we have for simplicity taken the constant value $\xi = 0.05$. This value is within the ranges considered in [86, 113], where it was shown that that deviations by a factor two
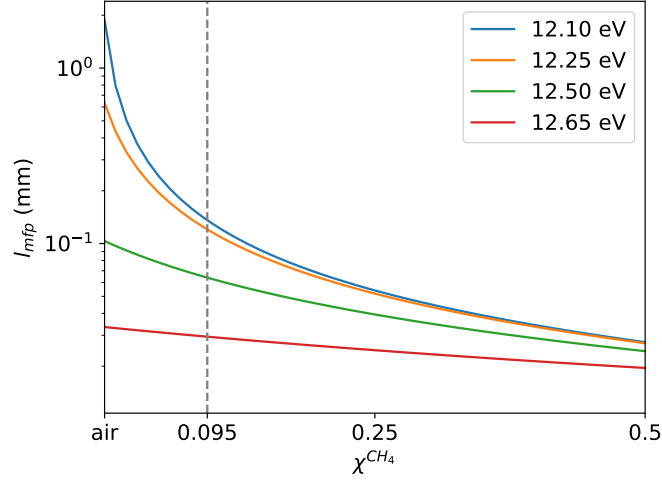
Fig. 3.2 The photon mean free path as a function of the CH_4 fraction χ^{CH_4} in air-methane mixtures for various photon energies. Stoichiometric conditions are denoted by the dashed grey line. Adding methane shortens the photon mean free path.

have little influence on most streamer properties, although lower values can increase the probability of streamer branching.

Photoabsorption:

The absorption of photons is determined by the photoabsorption cross sections σ. Kameta *et al.* [114] have determined the photoabsorption cross sections for CH_4. In the energy range relevant for the ionization of oxygen, $12.1 - 12.65$ eV, they found that the cross section for photoionization of CH_4 is negligble compared to non-ionizing photoabsorption of CH_4 (and also to the photoionization of O_2). Furthermore, in this energy region the value of σ^{CH_4} is roughly constant at $3.0 \cdot 10^{-17}$ cm^2. On top of that, we only have to consider the cross section for ionizing photoabsorption of O_2 in this energy range. σ^{O_2} is typically described as a power function of photon energy γ, whereas the cross sections for N_2 can be neglected [115]. This allows us to write the mean free path of a photon with an energy γ in interval $12.1 - 12.65$ eV as

$$l_{\mathrm{mfp}}(\gamma) = \left(\sigma^{CH_4} n^{CH_4} + \sigma^{O_2}(\gamma) n^{O_2} \right)^{-1}, \qquad (3.4)$$

with n representing the number density of a gas component (the number density N of an ideal gas is $2.4 \cdot 10^{25}$ m^{-3} at 1 bar and 300 K). The mean free path plays an important role in the dynamics of electron density fluctuations which are a result of stochastic photoionization. For that reason we have illustrated the dependency of l_{mfp} on the gas fraction of CH_4 in figure
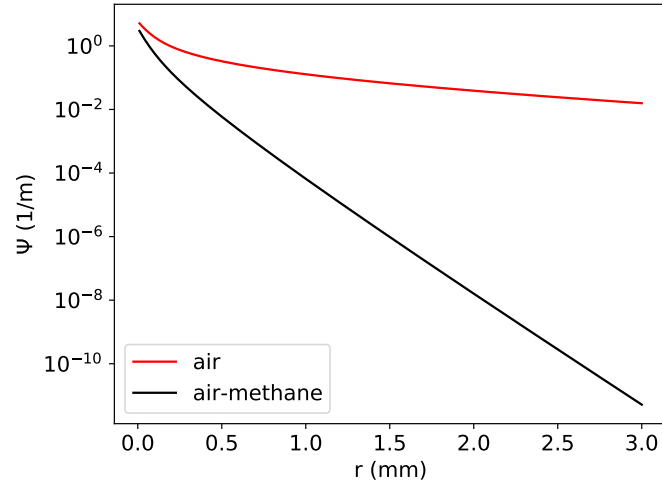
Fig. 3.3 The absorption function Ψ for air and an air-methane mixture containing 9.5% methane. This function illustrates the damping influence of methane on the photoionization mechanism.

3.2. The gas composition was determined by keeping the ratio between N_2 and O_2 fixed at 79 : 21 while varying the fraction of CH_4.

Finally, we formulate the probability of a photon to ionize O_2 (as opposed to being lost due to absorption by CH_4)

$$P(\gamma) = \frac{\sigma^{O_2}(\gamma)n^{O_2}}{\sigma^{CH_4}n^{CH_4} + \sigma^{O_2}(\gamma)n^{O_2}}. \tag{3.5}$$

Implementation:

The photoionization procedure in air-methane mixtures is implemented as follows: if a super-particle with weight w ionizes an N_2 or O_2 molecule (note that our choice for the parameter ξ in the Zhelezniak model corresponds to air), then that produces a random number of photons which are sampled from a Poisson distribution with mean $\bar{\eta}w$. Each of these photons are produced individually, i.e. the use of super-photons is excluded, and are assigned a random energy γ. Since the energy interval for ionization of O_2 is assumed to be uniformly populated, we take γ as a uniform random variable in the interval $12.1 - 12.65$ eV. Then a Bernoulli trial with probability $P(\gamma)$ determines whether the photon is lost due to absorption by CH_4. If not, the photon is emitted isotropically with a travel distance drawn from an exponential distribution with mean $l_{\mathrm{mfp}}(\gamma)$ upon which it ionizes an O_2 molecule.

Interpretation:

Now we illustrate the influence of CH_4 on photoionization. We do this by computing the absorption function Ψ, which can be expressed by the absorption function in air, Ψ_{air} as

$$\Psi = e^{-r\mu^{CH_4}}\Psi_{air}, \tag{3.6}$$

$$= e^{-r\mu^{CH_4}} \cdot \frac{e^{-r\mu_{min}} - e^{-r\mu_{max}}}{r\ln(\mu_{max}/\mu_{min})}, \tag{3.7}$$

with μ^{CH_4} the (constant) absorption coefficient due to methane, and μ_{min} and μ_{max} the absorption coefficients of dry air at 300 K and 1 bar according to [13, 115]. This function has been calculated for air and an 9.5% air-methane mixture (with $N_2 : O_2$ as 79 : 21) and shown in figure 3.3. Note that for the purpose of this illustration we have assumed that ξ is constant for both mixtures. Clearly, the addition of methane leads to a strong decay of the absorption function on the millimeter length scale. This length scale is relevant for the leading edge dynamics of the streamers considered in this research. Note that Ψ is not directly used in the PIC-MCC model, since photoionization events follow from sampling of relevant distributions as described in the previous section. Here, Ψ is only used for the purpose of illustration.

3.2.5   Computational domain and initial conditions

The simulated domain consists of a cube with a length of 10 mm for each Cartesian coordinate. The domain is filled with air or an air-methane mixture, consisting of 71.5% N_2, 19% O_2 and 9.5% CH_4, at 300 K and 1 bar. Such number fractions correspond to stoichiometric burning conditions of methane (i.e. $CH_4 : O_2$ as 1 : 2 and $N_2 : O_2$ as 79 : 21).

We are considering a plate-to-plate geometry with a grounded plate at the bottom of the domain and a high-voltage plate at the top. Furthermore the high-voltage electrode contains an axisymmetric protrusion with length of 1.8 mm and a radius of 200 μm. The tip of this needle-electrode is a hemisphere with the same radius, giving the electrode a total length of 2 mm. To solve for the electrostatic potential, we use the multigrid solver described in [116] which was recently generalized to include irregular boundaries. On the top electrode (including protrusion) a constant voltage ϕ of 12.5 kV or 20 kV is applied. Due to field enhancement near the needle the electric field is locally above breakdown. Far away from the needle the field relaxes to 12.5 kV cm^{-1} and 20 kV cm^{-1} respectively, which we will refer to as the background field E_0. The electric field is calculated by applying Dirichlet boundary conditions for the electric potential on the electrodes. The boundary conditions of the electric potential on the sides of the domain are given by homogeneous Neumann
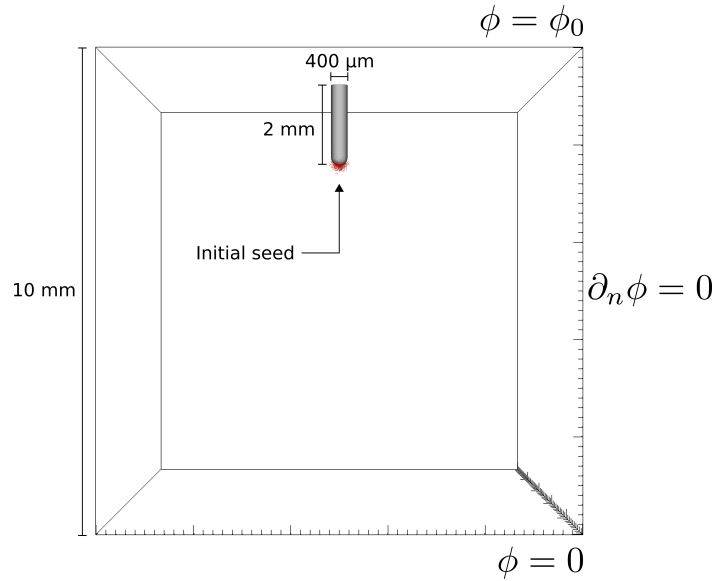
Fig. 3.4 The computational domain consists of a Cartesian cube with a length of 10 mm in each coordinate. The initial seed electrons are shown in red.

conditions, i.e. the field is parallel to the boundary. Moreover, super-particles are removed from the simulation if they are transported into the needle-electrode or out of the domain. Furthermore, the numerical grid is provided by the Afivo-framework [116] which utilizes adaptive mesh-refinement (AMR) with a minimum cell size of 4.0 μm. This cell size is sufficiently small in order to resolve the dynamics in the thin space-charge layer. Moreover, in [18] it was found that the particle model is less sensitive to the cell size than a fluid model, at least when comparing streamer velocities.

For all simulations in this work we use the same initial conditions consisting of a neutral seed around the electron tip. The seed consists of 1000 electron-ion pairs at coordinates that are drawn from a Gaussian distribution centered at the tip of the electrode with a variance of 125 μm^2. Coordinates coinciding with the interior of the needle-electrode are rejected. The electrons are represented by particles with unit weight whereas the ions are represented as a density. Such a neutral seed is convenient when comparing discharges under different conditions as it leads to fast inception which is not highly stochastic (studying inception is not the focus of this work). The electron density of the initial seed is illustrated in figure 3.4 in red.
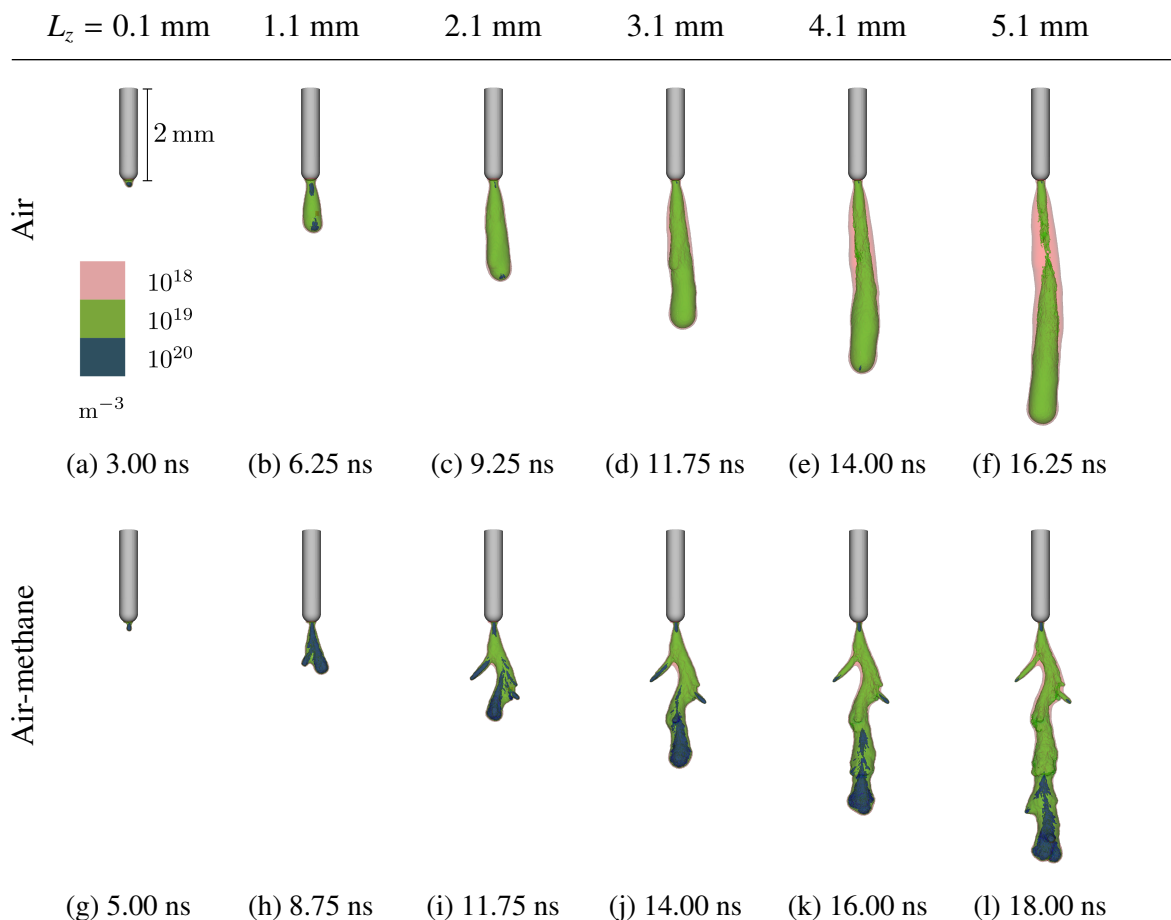
Fig. 3.5 Evolution of the electron density for positive streamers as a function of streamer length. Streamers propagate in a background field of $E_0 = 12.5$ kV cm^{-1} in air (top) and air-methane (bottom). The corresponding simulated times are supplied in the sub-caption. Visualization is performed with three partially-transparent contour surfaces. We observe that shape of the air streamer is smooth whereas the air-methane streamer is more erratic.

3.3   Comparison of air and air-methane streamers

Here we study how the addition of methane changes streamer properties. We focus on branching, electric field enhancement and electron energies.

3.3.1   Streamer branching

We will now study the influence of methane on streamer branching. To that end we have performed simulations in air and a stoichiometric air-methane mixture under the conditions described in section 3.2.5. The background electric field was taken as $E_0 = 12.5$ kV cm^{-1}. Furthermore the comparison will be performed for streamers of equal (vertical) length L_z. L_z

(a) Air   (b) Air-methane
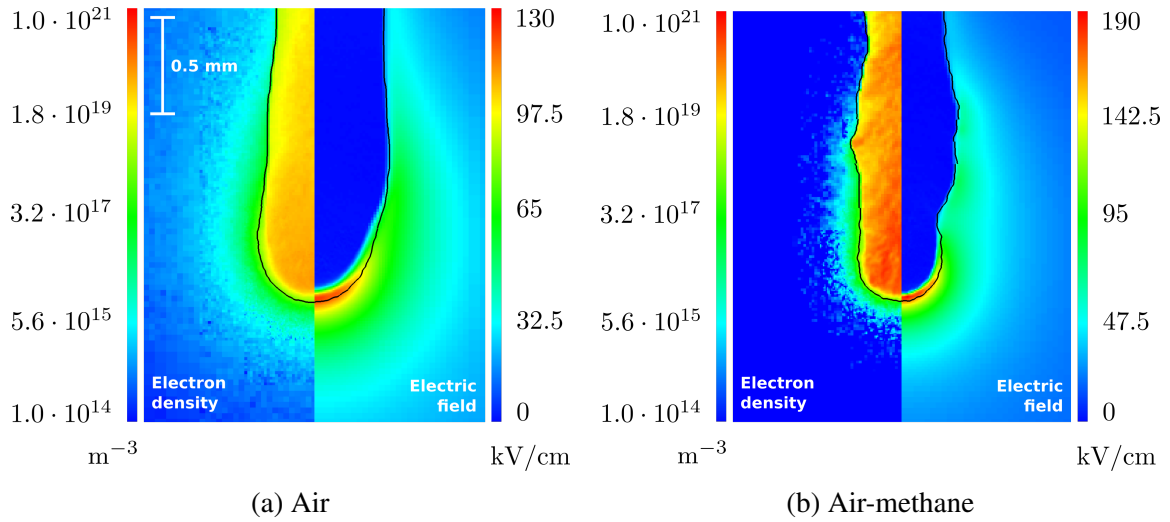
Fig. 3.6 Zoom into the electron density and the electric field on a cross section through the streamer head, of the discharges shown in figure 3.5. In all images, the contour line corresponding to an electron density of $1.6 \cdot 10^{18}$ m^{-3} is indicated. Electrons outside this contour are represented by individual particles (on the finest grid). Note the varying color scheme for the electric field which are matched to the electric field of the streamer tips. In air-methane we observe a smaller size of the electron cloud surrounding the streamer and a higher electric field at the tip than in air.

is obtained by calculating the maximum vertical distance between the electrode and each point in the domain where the electron density exceeds 10^{19} m^{-3}. We have chosen this threshold value because such densities are typically obtained in (or very near) the space-charge layer around the streamer tip. We visualize the streamer by plotting three partially-transparent contour surfaces.

In figure 3.5 we show the time evolution of positive streamers in both gases. We observe that the initial streamer formation takes about 2 ns longer in air-methane than in air (for $L_z = 0.1$ m), but that the main branch of both streamers then propagates at approximately the same instantaneous velocity (0.47 mm ns^{-1} for both gasses at 5.1 mm). For a discharge in air no branching occurs. However, in these conditions we do observe that the streamer does not propagate in a straight line but in a meandering fashion. Its counterpart in air-methane is more irregular. The first branching event occurred about 3.75 ns after inception (figure 3.5h). Further stochastic fluctuations occur throughout the evolution of the discharge which give the streamer an erratic shape.

The erratic streamer shape due to the addition of methane can be attributed to the suppression of photoionization. In section 3.2.4 we have shown that a gas fraction of 9.5% methane already significantly reduced the rate of photoionization and the photon mean free path while

only having a minor influence on the transport and reaction coefficients, as is also observed in [91]. This has a pronounced effect on the electron density ahead of the ionization front, as is shown in figure 3.6. In this figure we see slices of the electron density and electric field along the axis of propagation for both streamers after 3.7 mm. Electron densities are shown on the same logarithmic color scale, with maximum densities in the channel of $7.5 \cdot 10^{19}$ m^{-3} for air and $25 \cdot 10^{19}$ m^{-3} for air-methane. Electric fields are shown on different linear color scales, which are matched to the electric field at the streamer tip (130 kV cm^{-1} in air and 190 kV cm^{-1} in air-methane). In both gases we observe that the electron density in the leading edge decreases as we move farther away from the ionization front. However, for a streamer in air the electron density extends further ahead of the ionization front than its counterpart in air-methane. This is due to the difference in the longest photon mean free path. For sufficiently large distances r we find that the asymptotic behaviour of the function Ψ satisfies

$$\Psi(r) \propto r^{-1} e^{-r/l_{\max}}, \tag{3.8}$$

with $l_{\max}$ the longest photon mean free path (cf. figure 3.2 at 12.1 eV). Concretely, the characteristic length of the leading edge electron density, which is dominated by photoionization away from the streamer tip, is thus determined only by the longest photoionization length. Adding methane shortens the leading edge. Then, the electron density fluctuations ahead of the streamer tip, which are due to the discrete nature of photons, evolve due to impact ionization in the high electric field near the streamer tip. When these stochastically distributed electron avalanches reach the ionization front they accelerate branching [103].

In section 3.2.2 we have mentioned how to mitigate the influence of artificial noise introduced by super-particles. We also argued that on the finest grid we simulate leading-edge electron densities up to $1.6 \cdot 10^{18}$ m^{-3} with single particles only. This threshold density is denoted in figure 3.6 by a black contour line. Since this contour line is close to the space-charge layer we conclude that the leading edge dynamics are properly resolved. Thus, the observed stochastic fluctuations and their influence on streamer branching are physical.

3.3.2   Volume distributions of E and n_e

We will analyze the quantitative difference in the electric field and electron density between the air and air-methane streamers presented in the previous section. From figure 3.5 one can already note that the electron density in the tips of the air-methane streamers is higher. Furthermore, figure 3.6 shows that electric field enhancement is higher at the main branch of the air-methane streamer. A more complete illustration of the electric fields is shown in figure 3.7. There we have shown cross sections of electric fields on a logarithmic scale for
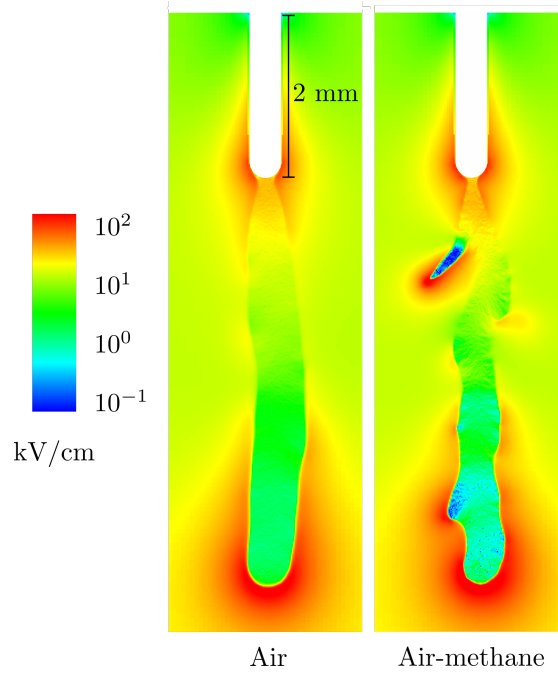
Fig. 3.7 Cross sections of the electric fields of discharges shown in figures 3.5f and 3.5l on a logarithmic scale. Internal electric fields in the streamer are lower in air-methane than in air. The thin stagnated side-branch has the lowest internal electric field.

streamers in both gases at 5.1 mm. These cross sections have the same perspective as in figure 3.5 and slice through the middle of the electrode. Because the streamers are not perfectly axisymmetric, sometimes streamer branches or other parts of the channel fall outside of the plane. Nevertheless, these images convey typical behaviour of the electric fields inside the streamer channel. In air, we observe that the electric field just after the streamer tip is around 1.5 kV cm^{-1} and gradually increases to around 25 kV cm^{-1} at the point of connection with the electrode. In air-methane typical electric fields inside the channel are slightly lower, in the range between $0.75 - 25$ kV cm^{-1}. Exceptions are the thin stagnated side-branches in air-methane, where the smallest internal electric fields lie around 0.1 kV cm^{-1}.

We will make these observations quantitative by introducing the volume-normalized distribution of the electric field strength $f_V(E)$

$$f_V(E) = \frac{1}{V_{\text{total}}} \frac{V(E) - V(E + \Delta E)}{\Delta E}, \tag{3.9}$$

where $V(E)$ is the volume in which the electric field strength exceeds E, and V_{total} is the total volume. So $f_V(E)$ denotes the volume of the domain where the electric field strength lies

(a) Electric field
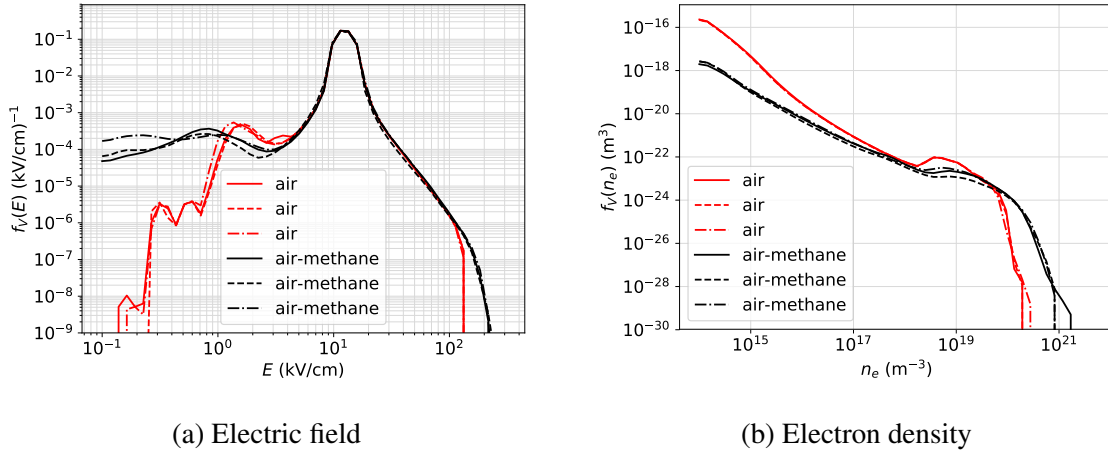
(b) Electron density

Fig. 3.8 The volume distribution $f_V(E)$ of the electric field strength and $f_V(n_e)$ of the electron density. We have shown three air streamers and three air-methane streamers at a length of 5.1 mm under conditions corresponding to figure 3.5. Air-methane streamers exhibit stronger electric field enhancement and higher electron densities.

within the small interval within E and $E + \Delta E$ which is then divided by ΔE and normalized with respect to the total volume.

$f_V(E)$ is shown in figure 3.8a for three simulations per gas mixture with different random seeds for streamers of 5.1 mm length. We use log-spaced bin sizes ΔE (for computational efficiency). The region with values below 5 kV cm^{-1}, corresponds to internal electric fields as shown in figure 3.7. The very low fields $0.1 - 0.5$ kV cm^{-1} are due to small side branches. Since the streamers in air that we consider have not branched these regions are non-existent (up to stochastic fluctuations). In the main channel of the discharge we find values of 1.5 kV cm^{-1} in air and 0.75 kV cm^{-1} in air-methane (in figure 3.7 it is shown that internal electric fields gradually increase to 25 kV cm^{-1} near the electrode). This is reflected in the distribution function by peaks at the associated values. Moving to higher fields, we find a large volume of the domain with fields ranging from $10 - 15$ kV cm^{-1}. This interval is dominated by the region away from the streamer, where the background electric field persists. Moving to even higher fields, we find the region that corresponds to the active zone induced by the discharge. Here we observe that air-methane streamers exhibit higher values for the electric field in its active zone. The maximum electric field is around 215 kV cm^{-1} in air-methane whereas in air we find a maximum value around 120 kV cm^{-1}. The maximal field in air-methane corresponds to the thin stagnated side-branch on the left (see figure 3.5l).

Analogously we show the volume distribution of the electron density

$$f_V(n_e) = \frac{1}{V_{\text{total}}} \frac{V(n_e) - V(n_e + \Delta n_e)}{\Delta n_e} \tag{3.10}$$

in figure 3.8b. Here $V(n_e)$ is the volume in which the electron density exceeds n_e. Air-methane streamers typically exhibit higher electron densities, which is probably due to a higher electric field at the tip. Furthermore, the low electron density region, say below 10^{16} m^{-3}, corresponds to the electron 'cloud' surrounding a streamer which is a result of photoionization. We observe that in air this electron cloud fills a much larger volume than in air-methane. In air-methane, the size of the cloud is reduced because CH_4 shortens the photon mean free path. Thus we find that a smaller part of the discharge is associated with this region.

To conclude, positive streamers in air-methane compared to air: (1) have smaller electron cloud surrounding the streamer, (2) have electric fields at the tips of their ionization fronts which are higher by a factor 1.5, (3) have internal electric fields that are lower by a factor two and (4) have higher electron densities that are higher by a factor three.

3.3.3   Electron energy distribution

In figure 3.9 we show a comparison of the electron energy distribution function (EEDF) of positive streamers in air and a stoichiometric air-methane mixture. The distribution was calculated in both gases when the streamer reached a length of 5.1 mm. This corresponds to figures 3.5l and 3.5f. The EEDF was obtained by calculating the kinetic energy of each super-particle and making a histogram with a bin size of 0.75 eV.

For both gases we observe similar qualitative behaviour of the EEDF: most of the electrons have energies below 5 eV and only a few electrons have energies sufficiently high to ionize neutral gas molecules (e.g. the lowest ionization threshold is 12.1 eV corresponding to O_2). These electrons are most likely to be situated in the region where ionization occurs, namely the ionization front and the part of the channel close to the electrode. For both gases we also find electrons with energies above 100 eV. For air-methane we even observe an electron energy exceeding 160 eV, which can be considered high for positive streamers. Electrons with such high energies are approaching the cold-electron runaway regime [117] and challenge the assumption of isotropic scattering, which is also made in our model.

A distinction between the two gases is that the tail of the distribution is more enhanced in the air-methane mixture. This is to be expected due to the higher electric field at the tip of the
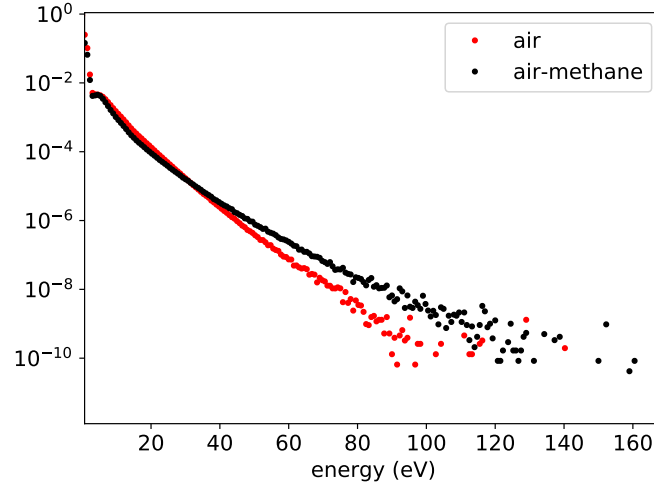
Fig. 3.9 The EEDF of streamers presented in section 3.3.1 with a length of 5.1 mm. A higher E_{max} in the case of air-methane leads to higher electron acceleration which enhances the tail.

streamer, as was shown in section 3.3.2, combined with the fact that electron energy losses in the tail hardly change by the addition of methane [32], cf. figure 3.1.

3.4   Plasma-chemical activation

Here we will investigate the energy deposition and the production of reactive species. These streamer properties are relevant for plasma-assisted combustion. Furthermore we highlight that these properties are comparatively insensitive to the considered electric fields.

3.4.1   Deposited energy density

We will now investigate the energy that a positive streamer deposits to the gas molecules in a stoichiometric air-methane mixture. To this end, we have performed simulations under the conditions shown in figure 3.4 for two background fields: $E_0 = 12.5$ and 20 kV cm^{-1} (named 'low field' and 'high field', respectively). From these simulations we have extracted the deposited energy density by electron scattering ε_{dep}. Note that this quantity is integrated over time. The deposited energy density is calculated by cumulatively interpolating the energy losses of all the inelastic scattering events for each time step to the grid. Since inelastic electron scattering is the dominant contribution to the deposited energy density, this term represents the conversion of kinetic electron energy to chemical activation. In a fluid approach, the deposited energy density described above corresponds to the term $\int_0^T j \cdot E \, dt$, where j is the electric current density and T is the time. Similarly we also calculate the power
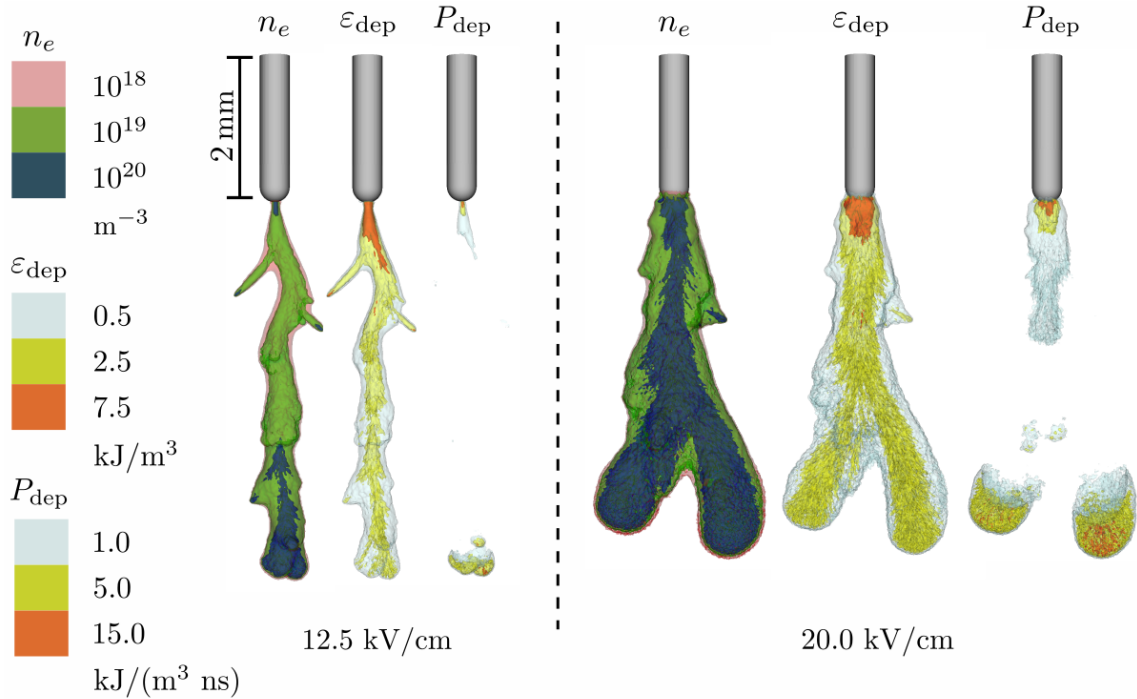
Fig. 3.10 Contour surfaces of the electron density, the deposited energy density and the power density deposition within 0.25 ns. We show air-methane streamers with a length of $L_z = 4.8$ mm in two background fields. Due to a higher velocity in higher electric fields, the contribution of the ionization front to P_{dep} appears more smeared out.

density deposition P_{dep}, which is the instantaneous energy density deposition. This quantity is obtained by calculating the numerical time derivative of ε_{dep} with a time step of 0.25 ns. Since the high field streamers have a higher velocity, the contribution corresponding to the moving ionization front appears to be more smeared out compared to the low field.

In figure 3.10 we have shown the contour surfaces of the electron density n_e, the time-integrated deposited energy density ε_{dep} and the power density deposition P_{dep} for both applied electric fields. Both streamers have an equal length of $L_z = 4.8$ mm. In the low field the discharge developed to this size in 18 ns whereas in the high field only 4.25 ns was needed. A result of the difference in the timescales is that the effects of electron loss in the channel due to attachment are visible in the low field but not in the high field. For the ε_{dep} we observe a peak in deposited energy in a small region close to the electrode in both fields. In that region the energy density ranges from 10 to 100 kJ m^{-3} (not shown) and keeps growing over time. Such interactions between the streamer channel and the needle electrode are not uncommon, see [118, 113] for example. Away from the needle we have a typical deposited energy density between 0.5 and 2.5 kJ m^{-3} that is comparatively insensitive to the applied

electric field. However, for thin branches (as one can see on the sides of the discharge in the low field) the deposited energy is higher: around 5.0 kJ m^{-3}. These thin side-branches have a higher deposited energy density than the thicker main streamers due to a higher electric field enhancement at the streamer tip. For the contour surfaces of P_{dep}, we have chosen the contour values such that they correspond to the deposited energy density within the time step of 0.25 ns. From this we can see that energy is mainly deposited by the ionization front and the small region near the electrode. As the ionization front propagates, it leaves behind energy in the new region of the channel. Moreover, as the streamer grows further a current continuously flows through the channel which also contributes to the deposited energy density, but these illustrations indicate that this contribution is only minor. Furthermore, the large power density deposition near the electrode shows that the deposited energy in this region grows over time.

In figure 3.11 the normalized volume distribution of the deposited energy density $f_V(\varepsilon_{\mathrm{dep}})$ is shown for three simulations per applied electric field. This quantity is defined analogously to equation (3.10) but with $V_{\mathrm{total}} = V(\varepsilon_{\mathrm{dep}} > 10^{-2}$ kJ m$^{-3})$. In other words we normalize with respect to the volume treated by the discharge, which is taken as the volume where the deposited energy density exceeds 10^{-2} kJ m^{-3}. This leaves the volume distribution invariant to differences in amount of volume treated by the discharge. This is convenient when comparing discharges that have different radii as is the case for streamers in different electric fields. From this graph we can conclude that a higher applied electric field does not necessarily lead to a higher deposited energy density, as the distributions of both fields (up to 10 kJ m^{-3}) practically coincide. Note that the high field discharge does in fact treat a larger volume of the gas, but that distribution functions are invariant to such differences due to normalization. Since the deposited energy density below 10 kJ m^{-3} is associated with the ionization front, cf. the contour surfaces of figure 3.10, These results indicate that the deposited energy density dynamics of the ionization front are quite insensitive to the applied electric fields considered here.

Furthermore, for deposited energy density values above 10 kJ m^{-3} (which are associated to the region close to the needle electrode) the distribution is actually higher in the low electric field. One aspect that contributes to this difference is that the width of the channel that is connected to the electrode is much smaller for the streamer in the low field. Hence the current density that flows through the channel of the streamer is higher near the electrode which leads to a larger deposited energy density.
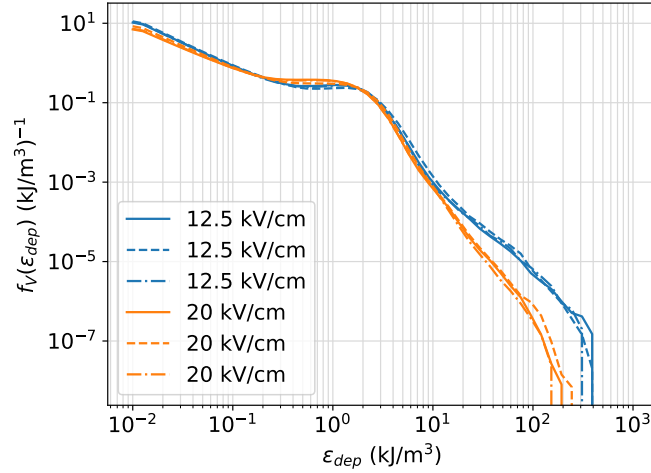
Fig. 3.11 Volume distribution of the deposited energy density for air-methane streamers with $L_z = 4.8$ mm. For each applied electric field we have performed three simulations.

In conclusion: Away from the electrode, streamers in both fields considered here have a similar deposited energy density. However, the high field streamers are generally wider and therefore treat a larger volume of the gas.

3.4.2   G-values for the production of reactive species

A positive streamer produces various reactive species that are of interest to plasma-assisted combustion. For example, electron-impact can directly dissociate a molecule and hence produce radicals. Moreover, the electronically excited states can also lead to further radical production by auto-dissociation, dissociative quenching of another molecule or through chemical reactions [119].

In this section we will calculate the efficiency with which specific primary species are generated. With 'primary' we mean that we only consider the production that follows directly from electron impact due to the streamer. The efficiency is expressed as the number of reactive particles created per 100 eV of input energy, named the G-value (with units 1/(100 eV)). In order to calculate this we have cumulatively recorded the number of excitations that have occurred for each type of collision. The spatial coordinates of an excitation event are not stored, as that would significantly affect computation time.

The G-values corresponding to individual species are shown in 3.A. In this section, the species are grouped into:

- the oxygen singlet states $O_2(a^1\Delta_g, b^1\Sigma_g^+)$,
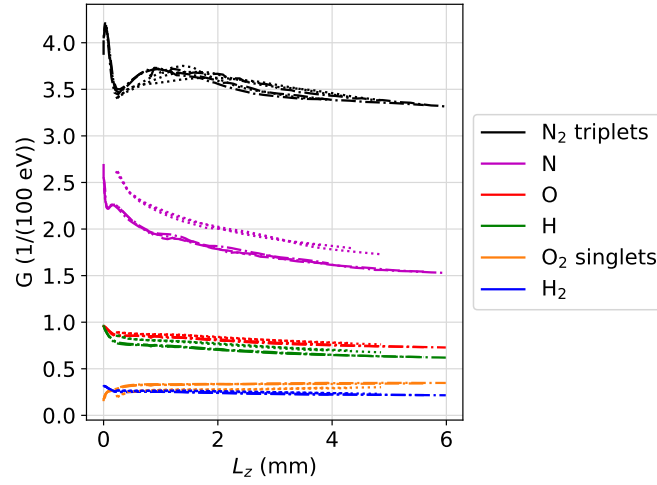
Fig. 3.12 The G-values (i.e. number of particles produced per 100 eV) of various groups of reactive species as a function of streamer length L_z. Dash-dotted corresponds to the low background field of 12.5 kV cm^{-1}. Dotted corresponds to the high background field of 20.0 kV cm^{-1}.

- the nitrogen triplet states N$_2$($A^3\Sigma_u^+$, $B^3\Pi_g$, $C^3\Pi_u$, $B'^3\Sigma_u^-$, $E^3\Sigma_g^+$, $F^3\Pi_u$, $G^3\Pi_u$, $W^3\Delta_u$), and

- the radicals N, O, H and H$_2$ that are directly created by electron impact dissociation.

The spatial profile of the densities of all species (not shown) is similar to that of the energy deposition depicted in section 3.4.1. In the region near the needle-electrode we will find high values of the densities. Away from the needle the reactive species are produced in comparatively fixed densities.

In figure 3.12 we show the G-values produced by the discharges presented in section 3.4.1, for the background fields $E_0 = 12.5$ and 20.0 kV cm^{-1}. The G-values are calculated for the whole discharge evolution until the streamer has reached the vertical length L_z, and they are plotted as a function of L_z. Similar to the results of the average energy deposition, we find that the G-values for the production of reactive species are comparatively insensitive to the applied electric field and do not change greatly as the streamers grow. Similar observations were made regarding the calculated G-values in flue-gases [120]. The highest G-value corresponds to nitrogen triplet states, where 3.3 particles are produced per 100 eV (at a length of 5 mm). Direct electron impact dissociation of molecules nitrogen and oxygen is also prevalent, with G-values of $1.5 - 1.7$ and 0.7, respectively. Furthermore, under these conditions the electron-impact dissociation of methane produces atomic and molecular hydrogen radicals

with a typical G-value of 0.6 and 0.2, respectively. Finally, the low-threshold singlet states of oxygen have a comparatively low G-value of around 0.3.

These G-values show that positive streamers in stoichiometric air-methane mixtures primarily produce large amounts of reactive nitrogen species. This leads to further dissociation of O_2, CH_4 and H_2 in the plasma-afterglow (which is not accounted for here). For O_2, we observe that direct dissociation by electron impact is much more prevalent than excitation to the low-lying singlet states. Finally, the dissociation of CH_4 predominantly produces atomic hydrogen, in amounts which are approximately equal to atomic oxygen.

In plasma-assisted combustion there is an interest in a broad range of operating conditions, with notable emphasis on high pressures and temperatures. In order to address that interest we sketch how to generalize our results to a wider parameter regime. We do so by relying on scaling laws for electric discharges, as is explained in [9]. Discharges at different pressures and temperatures are physically similar if the reduced electric field E/N is the same. Note then that high pressure and temperature can partially compensate each other as the relevant quantity in discharge physics is the gas density N. The G-values reported here are quite insensitive to the (reduced) electric field, suggesting that they might be representative for a larger range of pressures and temperatures than was considered in this work. Having said all that, it is known that the applicability of scaling laws is limited by a number of effects. For instance, at standard temperature and pressure the three-body attachment of electrons and the suppression of photon emission by collisional quenching violate these scaling laws. Thus electron loss and the production of photoelectrons do not scale with E/N. Another limiting factor is that we assume that electrons collide only with ground-state molecules. However, for very high temperatures or partially burnt mixtures electron scattering with fragmented or excited species will no longer be negligible.

Our results are relevant for studies using global (i.e. quasi-0D) kinetic models. These models are used to simulated the time evolution of hundreds of species using detailed chemical reaction mechanisms within reasonable computation time. However, such models can not resolve the streamer discharge phase which is strongly non-uniform, both spatially and temporally. The G-values reported here provide insight into the initial (practically instantaneous) production of reactive species. In this regard we mention other modelling studies that have reported on the production of reactive species in air-methane mixtures by a streamer discharge [93, 94, 91, 95, 97, 121, 96]. However, as far as the authors are aware the G-values for the primary production phase have not been computed with the level of detail and as complete as they have been reported here.

3.5   Summary and discussion

3.5.1   Summary

We have performed three-dimensional particle-in-cell simulations of positive streamers in air and in stoichiometric air-methane. In order to do so, we first extended the stochastic photoionization model by Zelezniak *et al.* [13] to account for quenching and non-ionizing photoabsorption due to methane. It follows that 9.5% methane already significantly suppresses photoionization in air, decreasing both number and mean free path of photons within the relevant energy interval significantly. Subsequently this influences streamer properties. This model allowed us to show that:

1. air-methane streamers branch more often than their counterparts in air. We have attributed this to the decreased photoionization, while mobility and effective ionization coefficients stay essentially unchanged.

2. under the same conditions streamers in air-methane have a higher field enhancement than in air, lower internal electric fields, a higher electron density in the streamer channel, and higher electron energies.

On the side of plasma-assisted combustion we have shown that:

3. the ionization front in air-methane streamers in background fields of 12.5 and 20.0 kV cm^{-1} typically deposits around $0.5 - 2.5$ kJ m^{-3} into plasma-chemical activation of the gas. This quantity appeared to be quite insensitive to the considered applied electric fields.

4. similar to the deposited energy density, the streamers produce typical densities of reactive species within the streamers that appear to be quite insensitive to the electric fields applied in this study. We calculated the G-values for the production of these species which are primarily N$_2$ triplet states, but also N, O and H radicals.

5. aside from aforementioned similarities, the high field streamers have larger radii (thus they treat a larger volume) and propagate faster.

3.5.2   Discussion

Our comparison of streamers in air and in a stoichiometric air-methane mixture shows that it is important to correct the photoionization properties for the presence of methane. However, the importance of a suppressed photoionization mechanism diminishes in situations with considerable degrees of background ionization, for instance in a pulsed discharge with a high repetition frequency.

On the side of plasma-assisted combustion, our model represents only the initial source of reactive species that arises due to direct electron impact or photoionization in the streamer discharge. Important secondary production of radicals due to chemical reactions occurs on slower time scales. The G-values presented in this work could be used in a combustion model adapted to resolve the subsequent chemical processes and thereby account for the non-equilibrium excitation of the gas by a streamer. In this context we have shown that, away from the needle-electrode, the streamer produces reactive species in comparatively fixed densities which suggest that a volume-averaged modelling approach with a parametrization of the streamer phase can be considered. We refer the reader to [97] for a deeper discussion into the use of global models.

Appendix 3.A   Tabulated G-values per excited species

In section 3.4.2 and in figure 3.12 the G-values of groups of excited species were given. Here we resolve the G-values per excited species in tables 3.1, 3.2 and 3.3 for N_2, O_2 and CH_4, respectively. The G-values are the number of excitation events per 100 eV that generate a particular excited species or group of species. Note that to convert back to the G-values per grouped species, the values corresponding to processes that produce multiple particles first have to be properly weighted, e.g. the reaction

$$e + N_2 \rightarrow e + N + N,$$
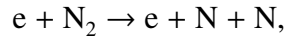
produces two nitrogen atoms and therefore has a weight of two. For convenience we have also supplied the activation energy ϵ_a for each scattering process. Moreover, since the streamers in both electric fields are similar we only give the G-values corresponding to streamers in 12.5 kV cm^{-1} when they have reached a length of 6 mm.

Table 3.1 The G-values for the generation of excited states of N_2. The excitation energies of the species are given as well.

	G (1/(100 eV))	ϵ_a (eV)
$N_2(A^3\Sigma_u^+)$	1.055	6.169
$N_2(B'^3\Sigma_u^-)$	0.104	8.166
$N_2(B^3\Pi_g)$	1.007	7.354
$N_2(C^3\Pi_u)$	0.741	11.033
$N_2(E^3\Sigma_g^+)$	0.019	11.872
$N_2(F^3\Pi_u)$	0.013	12.986
$N_2(G^3\Pi_u)$	0.028	12.811
$N_2(W^3\Delta_u)$	0.365	7.363
$N_2(a''^1\Sigma_g^+)$	0.059	12.256
$N_2(a'^1\Sigma_u^-)$	0.065	8.399
$N_2(a^1\Pi_g)$	0.371	8.550
$N_2(b'^1\Sigma_u^+)$	0.065	12.855
$N_2(b^1\Pi_u)$	0.140	12.501
$N_2(c_3^1\Pi_u)$	0.055	12.913
$N_2(c_4^1\Sigma_u^+)$	0.038	12.935
$N_2(o_3^1\Pi_u)$	0.034	13.104
$N_2(w^1\Delta_u)$	0.063	8.896
$N_2(J = 2)$	34.406	0.002
$N_2(v = 1)$	13.834	0.288
$N_2(v = 2)$	6.337	0.573
$N_2(v = 3)$	3.368	0.855
$N_2(v = 4)$	1.731	1.133
$N_2(v = 5)$	0.822	1.408
$N_2(v = 6)$	0.365	1.679
$N_2(v = 7)$	0.152	1.947
$N_2(v = 8)$	0.059	2.211
$N_2(v = 9)$	0.021	2.471
$N_2(v = 10)$	0.007	2.728
N + N	0.749	9.754
N_2^+	0.260	15.582
$N_2^+(A^2\Pi_u)$	0.182	16.700
$N_2^+(B^2\Sigma_u^+)$	0.040	18.752
N + N$^+$	0.023	24.342
N + N^{++}	$3.5 \cdot 10^{-6}$	69.505

Table 3.2 The G-values for the generation of excited states of O_2. The excitation energies of the species are given as well.

	G $(1/(100 \text{ eV}))$	ϵ_a (eV)
$O_2(2B)$	0.003	15.001
$O_2(A^3\Sigma_u^+, \; A'^3\Delta_u, \; c^1\Delta_u)$	0.170	4.200
$O_2(B^3\Sigma_u^-)$	0.594	6.120
$O_2(LB)$	0.022	15.001
$O_2(a^1\Delta_g)$	0.276	0.977
$O_2(b^1\Sigma_g^+)$	0.066	1.627
$O_2(v = 1)$	51.701	0.214
$O_2(v = 2)$	7.296	0.460
$O_2(v = 3)$	0.150	0.696
$O + O$	0.341	5.100
O_2^-	0.520	0.000
$O + O^-$	0.012	0.000
O_2^+	0.113	12.071
$O + O^+$	0.013	23.002
$O + O^{++}$	$1.3 \cdot 10^{-6}$	73.006

Table 3.3 The G-values for the generation of excited states of CH_4. The excitation energies of the species are given as well.

	G (1/(100 eV))	ϵ_a (eV)
$CH_4(v = 1, v = 3)$	2.299	0.362
$CH_4(v = 2, v = 4)$	4.621	0.162
$CH_3 + H$	0.526	7.501
$CH_2 + H_2$	0.205	9.101
$CH + H_2 + H$	0.003	15.501
$C + H_2 + H_2$	$5.5 \cdot 10^{-4}$	15.501
$CH_3 + H^-$	0.004	0.000
$H_2 + CH_2^-$	$2.5 \cdot 10^{-4}$	0.000
CH_4^+	0.144	12.631
$CH_3 + H^+$	0.002	21.102
$H + CH_3^+$	0.089	12.631
$CH_2 + H_2^+$	$2.4 \cdot 10^{-4}$	22.302
$H_2 + CH_2^+$	0.007	16.201
$H + H_2 + CH^+$	0.002	22.202
$H_2 + H_2 + C^+$	0.000	22.002

Chapter 4

Estimating the properties of single positive air streamers from measurable parameters

We develop an axial model for single steadily propagating positive streamers in air. It uses observable parameters to estimate quantities that are difficult to measure. More specifically, for given velocity, radius, length and applied background field, our model approximates the ionization density, the maximal electric field, the channel electric field, and the width of the charge layer. These parameters determine the primary excitations of molecules and the internal currents. Our approach is to first analytically approximate electron dynamics and electric fields in different regions of a uniformly-translating streamer head, then we match the solutions on the boundaries of the different regions to model the streamer as a whole, and we use conservation laws to determine unknown quantities. We find good agreement with numerical simulations for a range of streamer lengths and background electric fields, even if they do not propagate in a steady manner. Therefore quantities that are difficult to access experimentally can be estimated from more easily measurable quantities and our approximations. The theoretical approximations also form a stepping stone towards efficient axial multi-streamer models.

4.1 Introduction

4.1.1 The challenge of model reduction

Streamer discharges occur widely in nature and technology [9]. The most commonly encountered and studied streamers appear in air and carry positive net charge at their heads. They are the topic of the present study.

The inner structure of a streamer consists of a thin moving curved space charge layer around a weakly ionized channel with strong field enhancement and steep electron density gradients at the tip. This is challenging to simulate numerically, even for a single axisymmetric streamer in a long gap and a low background electric field [123]. On the other hand many discharge phenomena consist of numerous interacting streamers [9, 2, 124–126]. This poses a strong motivation to reduce the model while not giving up the physical basis and the model validation achieved in recent years [123, 113, 127, 128].

Streamer discharges consist of clearly distinguishable regions where different physical mechanisms are dominating the behaviour: (i) a non-ionized outer area where the electrostatic Poisson equation has to be solved, (ii) the avalanche zone where photoionization creates many growing electron avalanches, (iii) the moving streamer heads with an active space charge layer where ionization increases rapidly and the field is highest, and (iv) ionized channels with charges and currents and dynamically changing conductivity. Since the regions are governed by different mechanisms we will analyse them separately. Later we match the different regions at their boundaries.

For the channel region an axial approximation has been formulated in [10, 129], but for the streamer head the problem is open. In this work we will concentrate on the heads. To allow for comparison between numerical simulations of the fluid model and analytical approximations, we constrain the analysis to single streamers in a uniform field and mostly to steady propagation.

4.1.2 Steady streamers as a test case

In sufficiently low electric fields a streamer can propagate at a constant velocity without changing shape [85, 130–132]. Such streamers leave no charge behind and their channel electric fields decay back to the applied background field. From now on we will refer to these as *steady*, because in a co-moving coordinate system such uniformly translating streamers are in a steady state. The properties of positive steady streamers can be considered extreme, with

velocities as low as $3 \cdot 10^4$ m s^{-1}, electric fields enhanced to values as high as 222 kV cm^{-1}, steep gradients and a strongly curved thin charge layer [131].

The analysis presented in this work focuses heavily on steady streamers, since it is mathematically convenient to consider steady state solutions, as they have no explicit time dependence in a co-moving frame. Furthermore, we validate our approximations by comparing them to simulated results of a steady streamer. It must be noted that such a steady state approach could also be considered for accelerating streamers, since their properties typically change slowly with respect to other relevant time scales [133]. To that end we also compare our approximations to simulations of three accelerating streamers.

4.1.3   Earlier work

A classical challenge is to develop equations of motion where the head is characterized by a few numbers like radius R and velocity v. One of the first proposed analytic relations between R and v date back to 1965 [20] and an 'order-of-magnitude' model for the parameters of streamers was given in 1988 [24, 25]. A later experimental investigation proposed a data fit where the velocity depends on the radius squared, i.e. $v \sim R^2$ [134], and in [26] an approximate relation based on [20] was proposed where the velocity is also a function of the maximum electric field at the tip E_{max}, i.e. $v = v(R, E_{max})$. Other important theoretical results are: an approximation for the ionization density [25, 135, 136], energy efficiency estimates for radical production [137], an analytic investigation of the avalanche zone dynamics [138], 1.5D models that require a prescribed radius [133, 139] and an estimate for charge layer width based on the notion of an effective ionization length [140]. An application of streamer theory is to infer difficult-to-measure properties, such as E_{max}, from measurable parameters. For example, in [141] the authors estimate a parameter range for E_{max} on the basis of observed radius and velocity. Another example is [138], where an analysis of the avalanche zone gives an approximate relation between R, E_{max} and the head potential.

These theoretical results have improved our understanding of streamer dynamics and illustrated complex relations between different parameters. However, some ideas proposed in earlier works fail to agree with results from numerical simulations. At several instances throughout this work we will provide an in-depth evaluation of earlier work and propose improvements.

4.1.4   Content of the paper

In this work we develop semi-analytic approximations for the fluid model of single positive streamers that estimate difficult-to-measure quantities based on observable parameters. Specifically, we will show how velocity v, radius of curvature R, length L and background field E_{bg} determine ionization density $n_{i,ch}$, charge layer width ℓ and the maximum and channel electric fields E_{max} and E_{ch}, respectively

$$(v,\ R,\ L,\ E_{bg}) \rightarrow (n_{i,ch},\ \ell,\ E_{max},\ E_{ch}) \tag{4.1}$$

The derivation of our model starts by first defining different regions where specific physical mechanisms dominate. Then we provide analytic approximations for each of these regions separately. Finally we match the different regions at their boundaries and implement a self-consistent solution method. This results in a self-contained axial model which agrees well with numerical simulations. This means that our framework can complement experimental measurements when important streamer characteristics, i.e. the parameters on the right-hand side of equation (4.1), are difficult to measure precisely.

In section 4.2 we outline the classical fluid streamer model and the numerical implementation used for axisymmetric simulations. Furthermore, we discuss the results of numerical simulations in detail and introduce important definitions and conventions. In section 4.3 we integrate through the charge layer and obtain an analytic formula for the ionization density. In section 4.4 we give an analysis of the electron avalanche dynamics in the region ahead of the streamer. In section 4.5 we explore the notion of the streamer head potential. In section 4.6 we describe our solution method and validate our approximations with numerical results of the fluid model.

4.2   Model description, definitions and conventions

In this section we will present the classical fluid model for positive streamers in air at standard temperature and pressure. We discuss the numerical implementation, used to obtain reference solutions in homogeneous background electric fields below the breakdown value. The same implementation was used in [85, 130] to study steady streamers. Furthermore, we will also give definitions of macroscopic parameters and clarify other conventions and terminology.

4.2.1 Description of the model

Basic equations

We employ the classic fluid streamer model with local field approximation and without ion mobility. We only account for two charged species: the electron density n_e and the net ion density $n_i = n_+ - n_-$, with $n_\pm$ denoting the number density of all positive or negative ions. One can use just one ion density n_i instead of several ion species in regions where ion drift, electron detachment, and electron ion recombination can be neglected, as is the case in the streamer head. The electron density evolves according to a drift-diffusion-reaction equation while ions are considered immobile

$$\partial_t n_e = \nabla \cdot (\mu n_e \mathbf{E} + D\nabla n_e) + S_i + S_{ph}, \tag{4.2}$$

$$\partial_t n_i = S_i + S_{ph}, \tag{4.3}$$

with $\mathbf{E}$ the electric field, $\mu(E)$ the electron mobility, and $D(E)$ the electron diffusion coefficient. S_i and S_{ph} are the source terms for the effective impact ionization and photo-ionization respectively. We neglect electron diffusion, which is typically a good approximation except in low E_{bg} where we have steep gradients in the charge layer. Effective impact ionization is given by

$$S_i = |\mathbf{j}_e|\alpha_{\text{eff}}, \tag{4.4}$$

where $\mathbf{j}_e = -\mu n_e \mathbf{E}$ is the drift current density of electrons, $\mathbf{j} = -e\mathbf{j}_e$ is the electric current density, e is the elementary charge, and $\alpha_{\text{eff}}(E)$ is the effective ionization coefficient. The data for the transport and reaction coefficients are discussed in the next section. The photo-ionization source term in a volume V is given by

$$S_{ph}(\mathbf{r}) = \iiint_V \frac{I(\mathbf{r}')f(|\mathbf{r} - \mathbf{r}'|)}{4\pi|\mathbf{r} - \mathbf{r}'|^2}d^3r', \tag{4.5}$$

with $I(\mathbf{r}')$ the source of ionizing photons, $f(r)$ the absorption function and $4\pi|\mathbf{r} - \mathbf{r}'|^2$ is a geometric factor. Following Zheleznyak's model [13, 115], $I(\mathbf{r})$ can be expressed as

$$I(\mathbf{r}) = \frac{p_q}{p + p_q}\xi S_i(\mathbf{r}), \tag{4.6}$$

with p the actual pressure, $p_q = 40$ mbar the quenching pressure of the gas-mixture, and $\xi = 0.075$ a proportionality factor relating impact excitation to impact ionization S_i. The

absorption function $f(r)$ is given by

$$f(r) = \frac{\exp(-\chi_{\min} p_{O_2} r) - \exp(-\chi_{\max} p_{O_2} r)}{r \ln(\chi_{\max}/\chi_{\min})}, \tag{4.7}$$

with $\chi_{\max} = 150$ (mm bar)$^{-1}$, $\chi_{\min} = 2.6/$ (mm bar)$^{-1}$, and p_{O_2} is the partial pressure of oxygen. For air at 300 K and 1 bar, the corresponding absorption lengths are 33 μm and 1.9 mm.

The electric field follows from Poisson's equation for the electric potential ϕ

$$\epsilon_0 \nabla^2 \phi = -e n_q, \tag{4.8}$$

$$\mathbf{E} = -\nabla\phi, \tag{4.9}$$

with ϵ_0 the dielectric constant, e the elementary charge, and $n_q = n_i - n_e$ the charge number density.

Implementation of axisymmetric simulations

In this work we compare our axial analytical approximations with the axisymmetric solutions of equations (4.3) - (4.9) obtained by numerical simulation. The numerical model uses the afivo-streamer code [142, 116]. The computational setup is the same as in earlier studies [85, 130] to which we refer for an in-depth discussion.

The transport and reaction coefficients are calculated by Bolsig+ [14] (version 12/2019) using cross sections from the Phelps database [143] under the assumption that the evolution of the electron density follows an exponential temporal growth or decay [18]. We use the same data for the analytical and the numerical models. Additionally, the numerical model for the axisymmetric simulations uses continuity equations for a number of species such as O_2^+, O_2^-, N_2^+, N_4^+, *etc.* as listed in [130]. This more extended plasma chemistry model helps stabilizing the steady streamer at the lowest background electric field, and it is consistent with the two-species model for n_e and n_i in the streamer head, as recalled above.

The photo-ionization integral in equation (4.5) is approximated by a set of Helmholtz differential equations with Bourdon's three-term approximation [144]. This approximation introduces small changes the photon absorption lengths. However, in [18, 86] it was shown this has essentially no measurable influence on streamer discharge propagation in air.

Computational domain

The computational domain consists of a cylinder with 40 mm length and 20 mm radius, and planar electrodes on top and below. We impose cylindrical symmetry for domain and streamers; and we call the longitudinal coordinate ζ, and the radial coordinate r. An electric field is applied in the ζ-direction by fixing an electric potential difference between the electrodes. We use homogeneous Neumann boundary conditions for the potential in the r-direction, which means that the electric field is parallel to the lateral boundary. Homogeneous Neumann boundary conditions are also used for the electron density on all boundaries.

Initial conditions

For the initiation of a streamer discharge, we placed two neutral seeds composed of electrons and positive ions at the upper boundary of the domain. The uppermost seed creates a region of field enhancement, and the seed below it supplies the initial electrons ahead of the forming streamer, before photo-ionization sets in. More details on the seeds — their densities, coordinates, and sizes — can be found in [85, 130].

In low electric fields, an initial transient electric field is needed to ensure the inception of a streamer discharge. In this research we will consider homogeneous background electric fields from 4.5 to 24 kV cm^{-1}, all below the breakdown value of 28 kV cm^{-1}. At 4.5 kV cm^{-1}, a streamer propagating at constant velocity and shape was obtained using the velocity control method [131]. At 10 kV cm^{-1} we adopt the same initial transient electric field as discussed in [130].

To accommodate for the relatively small size of the steady streamer we used a grid with a minimum cell width of 0.6 μm. For the accelerating streamers, the mesh refinement routines are identical to those in [130].

4.2.2   Description of axisymmetric simulation results

The steady streamer in detail

In this section we will discuss one of these simulations in detail, the steady streamer at a background electric field of 4.5 kV cm^{-1}. We recall that a steady streamer [130, 85, 131, 132] looses its conductivity at its back end due to electron attachment and electron ion recombination, that it leaves no electric charge behind, but carries a fixed amount of charge along, and that it propagates with constant velocity and shape. Figure 4.1 zooms into the front part of this streamer and shows four important quantities: the electron density n_e, the
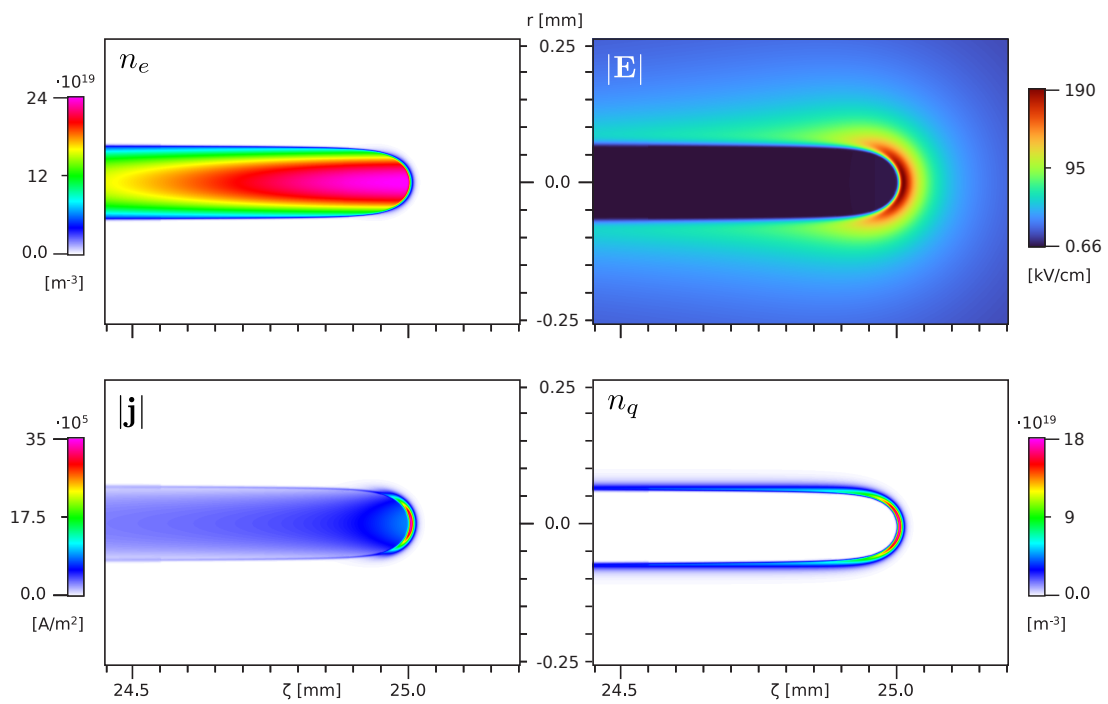
Fig. 4.1 Electron density n_e, electric field strength $|\mathbf{E}|$, strength of the electric current density $|\mathbf{j}|$ and charge number density n_q of a steadily propagating streamer in a background field E_{bg} of 4.5 kV cm^{-1}. The figure zooms into the area around the streamer head.

magnitude $|\mathbf{E}|$ of the electric field, the magnitude $|\mathbf{j}|$ of the electric current density and the charge number density n_q. From these quantities we can distinguish three regions with different dynamics:

1. *The channel* is the conductive interior of the streamer. We have a high electron density here and the plasma is quasi-neutral, $n_q \approx 0$. The electron density in the low axial electric field gives rise to an electric current flowing along the channel.

2. *The charge layer* is a layer of (positive) charge which surrounds and partially screens the channel. At the streamer head, the curvature of the charge layer leads to high electric field enhancement ahead of the front. In fact, we find the maximum electric field $E_{\max}$ here, with its location denoted by ζ_{tip}. As the electron density is high as well, we here have a high impact ionization rate and large currents resulting in the movement of the streamer head. The charge layer in the streamer head is also referred to as the ionization front. The width ℓ of the charge layer is much smaller than its radius R of curvature; this is required for the strong field enhancement ahead of the layer.

3. *The avalanche zone* of a positive streamer is the region ahead of the charge layer, so the electric charges in this region have a negligible effect on the electric field distribution. Without photo-ionization or some background electron density it could be neglected, but for positive streamers in air the photo-ionization creates many growing electron avalanches moving towards the charge layer. Close to the layer there is a high electric field, which means that a significant electron current is created which maintains the active ionization front. Specifically in air without background ionization, the electron density vanishes with an asymptotic decay dictated by photon absorption (Chapter 3)

$$n_e(\zeta) \propto \zeta^{-1} e^{-k\zeta} \text{ with } k = \chi_{\min} p_{O_2},$$
$$\text{for } \zeta \gg \zeta_{\mathrm{tip}}. \tag{4.10}$$

Directions of currents and fields

In figure 4.2 we zoom further into the ionization front and highlight important geometric features. We show the charge number density n_q and the magnitude of the electric current density $|\mathbf{j}|$ again in color-coding, but additionally we have visualized the direction of the current density by normalized arrows in the lower half of the plot, and the equipotential lines in the upper half of the plot. Note that in the avalanche zone the direction of the electron current $\mathbf{j}_e$ is radially inwards in a nearly spherical geometry, whereas in the channel the electron drift is homogeneously directed backwards parallel to the axis of propagation.
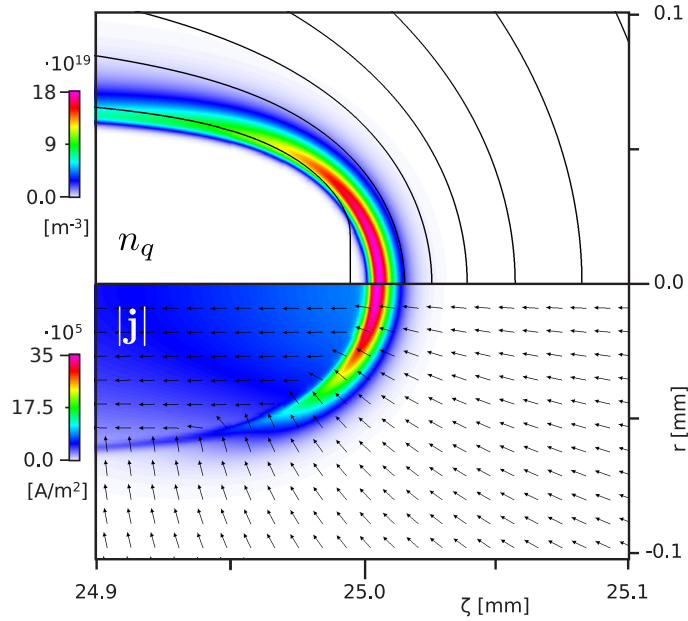
Fig. 4.2 Charge number density n_q and magnitude of the electric current density $|\mathbf{j}|$ of the steady streamer in a field of 4.5 kV cm^{-1} in color-coding. In the upper half of the plot, equipotential lines are laid over the charge number density. In the lower half, the arrows show the normalized direction of the electron drift $\mathbf{j}_e = -\mathbf{j}/e$.

Furthermore, the equipotential lines are very well aligned with the charge layer. This means that the electric current is essentially perpendicular to the layer in this region.

Streamers in different fields

In figure 4.3 we show current densities, electric fields and electron and charge densities on the streamer axis, now not only for the steady streamer in the field of 4.5 kV cm^{-1}, but also for accelerating streamers in background fields of 14 and 24 kV cm^{-1} when the streamer heads reached $\zeta = 15$ mm. In more detail, the upper plots show the electric current density. The middle plots show the electric field (solid line) with our approximation (dashed line) of section 4.3.2, and the lower plots show n_e, n_i and n_q.

4.2.3   Definitions and conventions

In this paper we develop an axial model for the dynamics in charge layer and avalanche zone, based on analytical approximations. Here we introduce definitions and conventions for this purpose. A schematic is given in figure 4.4.

(a) 4.5 kV cm^{-1} (b) 14 kV cm^{-1} (c) 24 kV cm^{-1}
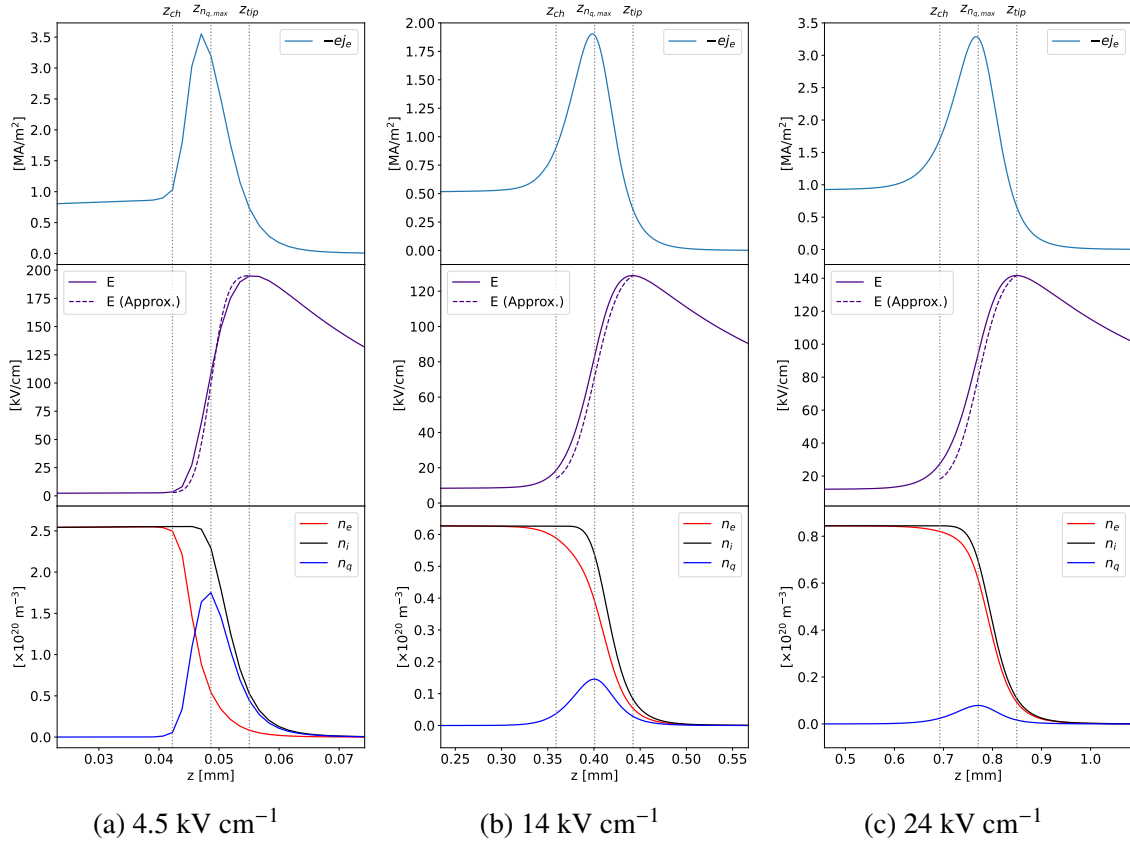
Fig. 4.3 Current density, electric field and particle densities on axis for streamers in three background electric fields. All streamers are shown when the head has reached $\zeta_{\text{tip}} = 15$ mm. The origin of the coordinate system, $z = 0$, is at the centre of the hemisphere fitted through the maximum of the charge number density. The corresponding v and R are shown in figure 4.5.
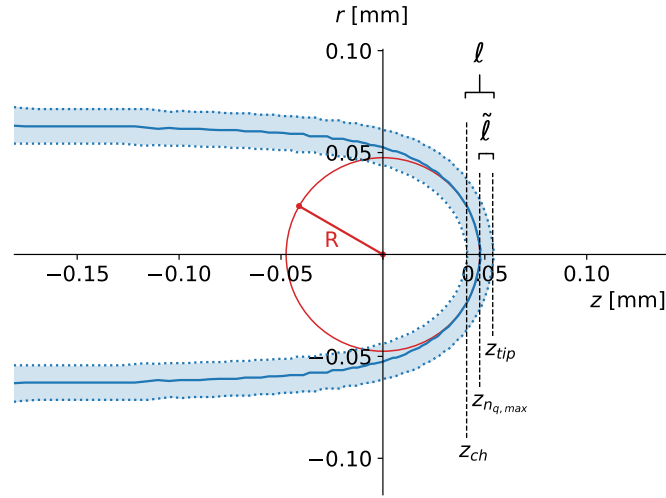
Fig. 4.4 The charge layer within the co-moving coordinate system (r, z) at $E_{bg} = 4.5 \text{ kV cm}^{-1}$. The solid blue line represents the maximum of n_q (for each z) from numerical simulation and the shaded area is the corresponding charge layer parameterized using ℓ. Also shown are: the tangent circle with radius R, $\tilde{\ell}$ and the positions z_{ch}, z_{tip} and $z_{n_{q,max}}$.

Definition of velocity and co-moving coordinate system

We define the streamer velocity v as the velocity of the location of the maximal electric field at the streamer tip

$$v(t) = \frac{d\zeta_{tip}(t)}{dt}.$$ (4.11)

The velocity extracted from simulations is shown in figure 4.5a. We introduce a coordinate system (r, z) that moves in the ζ direction with velocity v. The z coordinate can be written as

$$z = \zeta - vt.$$ (4.12)

Temporal derivatives transform to the new coordinate system as

$$\partial_t\big|_\zeta = \partial_t\big|_z - v\partial_z,$$ (4.13)

where $\partial_t\big|_z$ denotes the partial derivative ∂_t in the co-moving frame (r, z). For steady motion we thus can replace

$$\partial_t\big|_\zeta = -v\partial_z,$$ (4.14)

in the co-moving frame (r, z).

(a) Velocity   (b) Radius of curvature

Fig. 4.5 The velocity and radius as a function of the head position extracted from simulations at different background electric fields.

Parameterizing the charge layer

We will characterize the charge layer by two maxima, namely the maximum of the electric field and the maximum of the charge number density. On the streamer axis we will denote them as z_{tip} and $z_{n_{q,\text{max}}}$, and their distance as

$$\tilde{\ell} = z_{\text{tip}} - z_{n_{q,\text{max}}},$$ (4.15)

The two maxima are also illustrated in figure 4.3. There it is also shown that $z_{n_{q,\text{max}}}$ is located roughly in the middle of the charge layer and that j is approximately symmetric in the vicinity of this maximum. Therefore we define the interior boundary z_{ch} of the charge layer as

$$z_{\text{ch}} = z_{\text{tip}} - \ell \text{ with } \ell = 2\tilde{\ell}.$$ (4.16)

Definition of radius and of origin of coordinate system

We will characterize the streamer head by its radius of curvature R, defined as the radius of the circle which best approximates the curved charge layer at the streamer tip. This parameter is extracted from simulated data by fitting a semicircle through the maximum, for each z, of the charge layer, cf. figure 4.4. The extracted R is insensitive to fitting parameters provided the region is chosen sufficiently small. We therefore take this region to be $[z_{n_{q,\text{max}}} - 4\tilde{\ell}, z_{n_{q,\text{max}}}]$. The radius of curvature extracted from simulations is shown in figure 4.5b.

R is an important quantity because it determines the spatial decay of electric field and currents in the avalanche zone near the charge layer, as can be seen in figure 4.2. There

the equipotential lines trace the shape of the charge layer sufficiently close to the axis of propagation. We choose the centre of the sphere as the origin of the co-moving coordinate system, $(r, z) = (0, 0)$, as shown in Fig. 4.4.

Definition of streamer length for steady streamers

The steady positive streamers reported in [85, 130, 131] are all 'detached' from their point of inception. By this we mean that due to attachment and recombination processes the channel looses its conductivity to the point that the streamer cannot be considered as connected to an electrode or initial ionized seed. For these detached streamers it is more useful to characterize streamer length with a typical length scale for the loss of conductivity L_{loss}

$$L_{\text{loss}} = v\tau, \tag{4.17}$$

with τ the electron loss time representing the collective timescale of all conductivity loss processes. The studies [130, 131] contain investigations of L_{loss} and τ. In particular, it is analyzed how these quantities depend on the gas-composition and the electric field.

4.3   The charge layer $(z_{\text{ch}} \leq z < z_{\text{tip}})$

In this section we formulate axial approximations for the total current density and for the electron and ion densities in the space charge layer, i.e., in the region between the front end z_{ch} of the channel and the maximum of the electric field z_{tip} (cf figure 4.4). The width ℓ of this region is much smaller than the radius of curvature R, therefore this layer can approximately be treated as planar.

We can neglect photo-ionization S_{ph} in the charge layer since it is much smaller than S_i. Photo-ionization only matters in the avalanche zone due to its nonlocality. We also neglect the diffusive current assuming that it is dominated by convection.

4.3.1   Current densities in the charge layer

Due to charge conservation and the Poisson equation of electrostatics, the total current density $\mathbf{j}_{\text{tot}}$ is a conserved quantity

$$\nabla \cdot \mathbf{j}_{\text{tot}} = 0, \text{ where } \mathbf{j}_{\text{tot}} = \mathbf{j} + \epsilon_0 \partial_t \mathbf{E}. \tag{4.18}$$

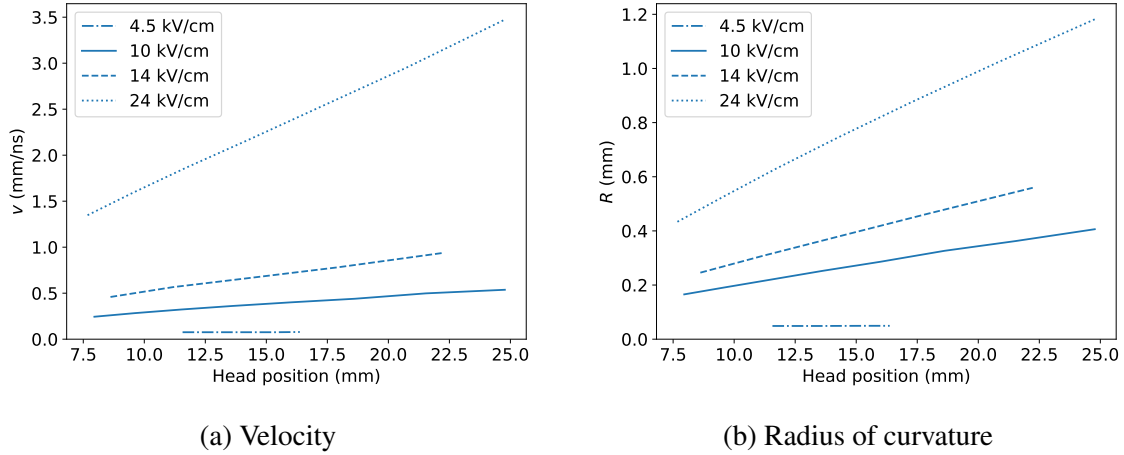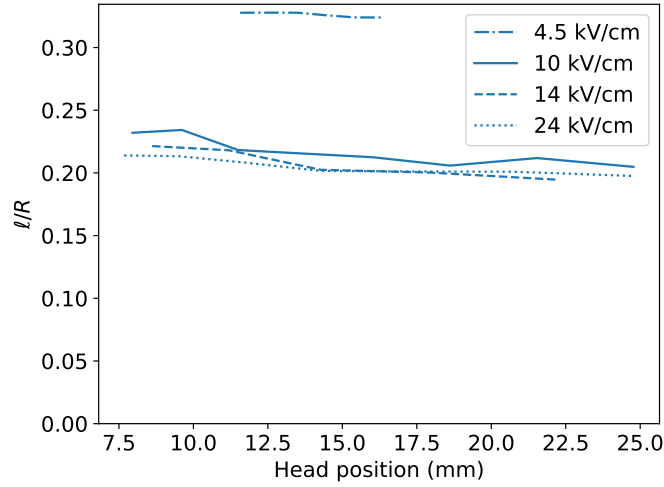Fig. 4.6 The dimensionless parameter ℓ/R as a function of the head position extracted from simulations at different background electric fields. This parameter characterizes the validity of the planar front approximation. The fluctuations observed are due to the small size of $\tilde{\ell}$ which is only a few times the smallest grid size.

For steady motion in a co-moving frame z, the total current is $\mathbf{j}_{tot} = \mathbf{j} - v\epsilon_0\partial_z\mathbf{E}$. Note that the current densities are taken in the stationary frame, $\mathbf{j} = -e\mu n_e\mathbf{E}$ expressed as a function of z.

To solve for $\mathbf{j}_{tot}$ we approximate the charge layer at the tip as a planar surface. The validity of this approximation is governed by the dimensionless parameter ℓ/R. More specifically we require $\ell/R \ll 1$, which usually holds for streamers as is shown in figure 4.6. In that case only the z-derivative of the divergence operator is non-vanishing. Then, equation (4.18) prescribes that $\mathbf{j}_{tot}$ is constant. With a boundary condition at z_{tip} this leads to the axial approximation

$$j_{tot}(z) = j_{tot}(z_{tip}). \tag{4.19}$$

Furthermore, the electric field is maximal at z_{tip}, hence $\partial_z\mathbf{E}|_{z_{tip}} = 0$ and the displacement current vanishes there

$$j_{tot}(z_{tip}) = -ej_{e,tip}, \tag{4.20}$$

where $j_{e,tip}$ is the electron current density on axis at z_{tip}. Similarly, the displacement current also vanishes approximately in the channel, where the electric field and electron density are nearly constant on-axis. This gives us

$$j_{e,ch} = j_{e,tip}, \tag{4.21}$$

where $j_{e,\text{ch}}$ is defined analogously as $j_{e,\text{tip}}$. Finally, combining this result with equation (4.19) determines $-j_{\text{tot}}/e = j_{e,\text{tip}} = j_{e,\text{ch}}$.

An analysis of the total current density at z_{ch} and z_{tip} was also proposed in [145]. They held that $j_{e,\text{tip}}$ vanishes which would mean that $j_{\text{tot}}(z_{\text{tip}})$ is completely determined by the displacement current $-v\epsilon_0 \, \partial_z \mathbf{E}|_{z_{\text{tip}}}$. However, the numerical simulations in figure 4.3 contradict this. In fact, we observe that at z_{tip} the displacement current vanishes since the electric field is maximal and conversely that $j_{e,\text{tip}}$ does not vanish, which is in line with our reasoning.

4.3.2 Ionization and electric field in the charge layer

As ions are essentially immobile within the propagating streamer head, the degree of ionization is best determined by the ion density $n_{i,\text{ch}}$ behind the charge layer. An old approximation dating back to [25, 135] is

$$n_{i,\text{ch}}^{\text{old approx}} \approx \frac{\epsilon_0}{e} \int_0^{E_{\max}} \alpha_{\text{eff}}(E) \, dE, \qquad (4.22)$$

where we use $E = |\mathbf{E}|$. In the appendix of [136] this equation is derived for planar negative streamer ionization fronts without electron diffusion or photo-ionization. The approximation is easily derived from the two following equations: equations (4.3) and (4.4) together yield

$$\partial_t n_i = |\mathbf{j}_e|\alpha_{\text{eff}}(E), \qquad (4.23)$$

and equation (4.18) reads $\epsilon_0 \partial_t E = -e j_e$, if the total current ahead of the charge layer vanishes. This is the case, if the electron density ahead of the planar front vanishes, and if the electric field ahead of the front does not change in time.

According to [136], equation (4.22) is a good approximation of the numerical solutions of planar negative ionization fronts without photo-ionization in a time independent electric field; the error is only 5 to 10%. However, in simulations of positive curved streamer fronts with photo-ionization as shown in [146, 131], the ionization density is about twice as high as given by the classical approximation (4.22) (in particular, see table B1 of [131]). In table 4.1 we make a similar comparison and confirm the discrepancy of equation (4.22) as an approximation of the ionization density of positive streamers.

A first hypothesis was that the approximation (4.22) only covers the part of the front where the electric field decays from its maximal value $E_{\max}$ to a low value inside the channel, and that it misses the avalanche zone ahead of the charge layer where the electric field increases to

Table 4.1 The ionization density $n_{i,\text{ch}}$ ($\times 10^{19}$ m^{-3}) for streamers in different background fields. All streamers are taken at $\zeta_{\text{tip}} = 15$ mm. We compare the old approximation (equation (4.22)) and our approximation (equation (4.26)) with our simulated results.

	classical eq. (4.22)	new eq. (4.26)	simulation
4.5 kV cm^{-1}	11.9	21.9	25.6
10 kV cm^{-1}	3.3	5.4	6.3
14 kV cm^{-1}	3.4	5.6	6.3
24 kV cm^{-1}	4.5	7.6	8.4

its maximum [146]. This avalanche zone is essentially absent without background ionization and photo-ionization, but very present in air. However, the ionization created in the avalanche zone contributes relatively little ionization. We discuss this later in more detail in section 4.6.2 and figure 4.8.

We will now show that the total current density $\mathbf{j}_{\text{tot}}$ from the avalanche zone into the curved charge layer contributes significantly to the ionization behind the front for positive streamers in air. The derivation of the new approximation is analogous to the earlier one in [136]. We start from (4.23) and express j_e in terms of j_{tot}

$$\partial_t n_i = \frac{1}{e} \left| \mathbf{j}_{\text{tot}} - \epsilon_0 \partial_t \mathbf{E} \right| \alpha_{\text{eff}}. \tag{4.24}$$

This can be further simplified for steady motion and because the vectors $\mathbf{j}_{\text{tot}}$ and $\mathbf{E}$ are parallel on the axis

$$\partial_z n_i = \left(\frac{\epsilon_0}{e} \partial_z E + \frac{j_{\text{tot}}}{ev} \right) \alpha_{\text{eff}}. \tag{4.25}$$

Integration through the ionization front gives

$$n_i(z) = n_{i,\text{tip}} + \frac{\epsilon_0}{e} \int_{E(z)}^{E_{\max}} \alpha_{\text{eff}}(E) \, dE + \frac{1}{ev} \int_z^{z_{\text{tip}}} \alpha_{\text{eff}}(E(z)) j_{\text{tot}} \, dz. \tag{4.26}$$

The first term is obtained after integration by substitution ($\partial_z E \, dz = dE$). It reproduces the old approximation (4.22) when it is evaluated at $z = z_{\text{ch}}$ and when $E(z_{\text{ch}})$ is approximated as vanishing. The second term requires further analysis. We approximate j_{tot} by the constant $-e j_{e,\text{tip}}$ according to equation (4.19). Furthermore, we need the spatial profile of $E(z)$ to evaluate $\alpha_{\text{eff}}(E(z))$ under the integral. Here we adopt a heuristic parametrization of E and leave further analysis to future work. In figure 4.3 we see that within the layer the charge

number densities n_q have an approximately Gaussian profile that can be parameterized as

$$n_q(z) = \frac{N_q}{\sigma\sqrt{2\pi}} \exp\left(-\frac{1}{2}\left(\frac{z-R}{\sigma}\right)^2\right), \tag{4.27}$$

with

$$N_q = \int_{z_{ch}}^{z_{tip}} n_q\,dz = \frac{\epsilon_0}{e}(E_{max} - E_{ch}), \tag{4.28}$$

an approximate normalization constant provided that $\sigma \ll \ell$.

Next, we use that over its small width the layer is only weakly curved, and we use a planar approximation $\partial_z E = e n_q/\epsilon_0$ to calculate the electric field as $E(z)$ by integrating over n_q

$$E(z) = E_{max} - \frac{e}{\epsilon_0}\int_z^{z_{tip}} n_q(z)dz. \tag{4.29}$$

This heuristic parametrization of the electric field is shown in the middle panels of figure 4.3 together with the results of the axisymmetric simulations. The parametrizations of E are in agreement with the simulated results when we choose $\sigma = \tilde{\ell}/3$ for the steady streamer and $\sigma = \tilde{\ell}/2$ for the accelerating ones. Furthermore, we remark explicitly that equation (4.27) is only used to motivate and evaluate the parameterization for E in equation (4.29).

Using equation (4.29) as an approximation for the electric field within the charge layer, we can calculate the ionization density by evaluating equation (4.26) at z_{ch}. In table 4.1 we compare this approximation, when all macroscopic parameters are extracted from simulations. We observe good agreement, with relative errors between 10-15%.

4.3.3   Electron density in the charge layer

Our derivation of the electron density within the charge layer starts from the fundamental equation of charge conservation

$$e\partial_t n_q = -\nabla \cdot \mathbf{j}. \tag{4.30}$$

Since we have uniform translation and a planar front we can write

$$vn_q = j_{e,ch} - j_e, \tag{4.31}$$

where $j_{e,ch}$ has been introduced as an integration constant. As a side note, a similar relation has also been proposed in [135, 141], but there the integration constant has been explicitly neglected. However, in figure 4.3 we see that $j_{e,ch}$ and $j_{e,tip}$ are significant. Continuing our

derivation, we use $n_q = n_i - n_e$ and rearrange the terms in this equation such that we find an expression for the electron density profile in the charge layer

$$n_e(z) = \frac{vn_i(z) - j_{e,\text{ch}}}{v + v_{\text{dr}}}, \tag{4.32}$$

with the charge drift velocity $v_{\text{dr}} = \mu E$. (Note that electrons drift with $-v_{\text{dr}}$). This determines $n_e(z)$ since $n_i(z)$ is given by equation (4.26). By evaluating this expression at z_{ch} or z_{tip} and using equation (4.21) we find quasi-neutrality: $n_{e,\text{ch}} = n_{i,\text{ch}}$ and $n_{e,\text{tip}} \approx n_{i,\text{tip}}$. Note that the implied quasi-neutrality at z_{tip} only holds as an approximation, see figure 4.3.

Moreover, integration of equation (4.31) through the charge layer and using (4.28) results in

$$\int_{z_{\text{ch}}}^{z_{\text{tip}}} e(j_{e,\text{tip}} - j_e) \, dz = v\epsilon_0(E_{\text{max}} - E_{\text{ch}}). \tag{4.33}$$

This can be interpreted as a physical connection between the movement of a positive charge layer (represented by a discontinuity in the electric field) and the separation of charge. The latter can be directly expressed by the electric current integrated through the charge layer.

4.4 The avalanche zone ($z \geq z_{\text{tip}}$)

The avalanche zone is defined as the region ahead of the space charge layer where space charges can be neglected, and where the electric field is above the breakdown value. This means that the electric field near this layer is dominated by the electric charges in the layer, and that charges in the avalanche zone move in this externally determined field, but do not contribute to it.

In the avalanche zone, different approximations have to be made than in the charge layer:

(i) As said above, the influence of the local charges on the electric field is negligible, $\nabla \cdot \mathbf{E} = 0$, so the avalanche develops in an externally determined electric field.

(ii) The dynamics inside the charge layer were described using the planar front approximation because $\ell \ll R$, but the planar front approximation is not valid in the avalanche zone. We therefore do account for the curvature of the charge layer in the avalanche zone. We do so by approximating the charge layer at the streamer tip as a hemisphere with a radius R, see figures 4.4 and 4.7.

(iii) Electron diffusion is still neglected but photoionization now needs to be included. Although the impact ionization is much stronger than the photoionization, the non-

locality of the photoionization is essential to create seed electrons in the avalanche zone.

4.4.1   Equation for electron density in the avalanche zone

The drift-diffusion-reaction equation (4.2) for the electron dynamics on the axis of the avalanche zone can be simplified as follows. First we remark that with the approximations above and with the chain-rule we can write on the axis

$$
\begin{aligned}
\nabla \cdot (\mu n_e \mathbf{E}) &= \mathbf{E} \cdot \nabla(\mu n_e) + \mu n_e \nabla \cdot \mathbf{E}, \\
&= E \partial_z(\mu n_e), \\
&= v_{\mathrm{dr}} \partial_z n_e + \frac{\partial_z \mu}{\mu} v_{\mathrm{dr}} n_e,
\end{aligned}
\tag{4.34}
$$

The electron dynamics of equation (4.2) then becomes, in the comoving frame on the axis,

$$
(v + v_{\mathrm{dr}}) \partial_z n_e + \frac{\partial_z \mu}{\mu} v_{\mathrm{dr}} n_e + S_i + S_{ph} = 0.
\tag{4.35}
$$

In the next section we derive an expression for S_{ph}.

4.4.2   Coupling between avalanche zone and charge layer

The dynamics in the avalanche zone are coupled to the other discharge regions. More precisely, the charge layer together with the channel generate the enhanced electric field in the avalanche zone, and the charge layer also emits the large majority of photons that generate photoionization and initiate the ionization avalanches in the avalanche zone.

The electric field near the charge layer and near the streamer axis are approximated by a uniformly charged sphere

$$
E(z) = \frac{z_{\mathrm{tip}}^2 (E_{\max} - E_{\mathrm{bg}})}{z^2} + E_{\mathrm{bg}},
\tag{4.36}
$$

as argued above.

For photoionization in air, the photons are mainly produced in the charge layer, because the majority of high-energy collisions occurs here, as will be shown in figure 4.8. Photons originating from the avalanche zone are therefore neglected. Moreover, since typical absorption lengths ($33-1900\,\mu$m for dry air at 1 bar and 300 K) are large compared to ℓ, cf figure 4.9, we can essentially treat the charge layer as a surface. Accordingly, we approximate equation
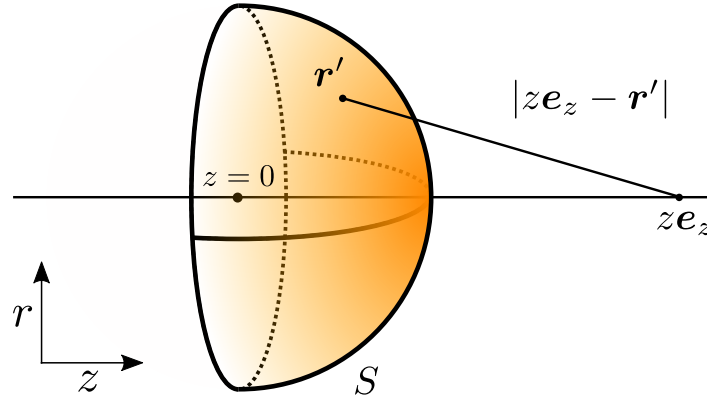
Fig. 4.7 The configuration used for computing the photo-ionization source term. The charge layer is approximated by a hemisphere S with radius R centered around $z = 0$. The color indicates that in reality the front is not radiating with uniform intensity but fades at the edges (even though we do not account for this here). Also shown is the path of a photon produced at $\mathbf{r}'$ and absorbed at $z\mathbf{e}_z$. Photoionization then creates electron avalanches that develop the local electric field. We use the avalanches on the z-axis for our approximations.

(4.5) by a surface integral

$$S_{ph}(z) = \iint_S \frac{I(\mathbf{r}')f(|z\mathbf{e}_z - \mathbf{r}'|)}{4\pi|z\mathbf{e}_z - \mathbf{r}'|^2}d^2r', \tag{4.37}$$

with $\mathbf{e}_z$ the unit vector in the z-direction, and the coordinates $\mathbf{r}'$ now lie on the surface S. For simplicity, we take S to be the surface of a hemisphere with radius R centered at $z = 0$. This is illustrated in figure 4.7.

The general photon source term from equation (4.6) is now approximated as

$$I(\mathbf{r}') = \mathcal{A}(\mathbf{r}')I^*, \tag{4.38}$$

with I^* the surface density of photon production

$$I^* = \frac{p_q}{p + p_q}\xi v n_{i,\text{ch}} \tag{4.39}$$

on the streamer axis. Here $p_q/(p + p_q)$ is the quenching factor of the photon emitting state. The excitation of the photon emitting state is approximated as impact ionization S_i times a proportionality factor ξ. Note that the impact ionization has to be integrated over the width of the charge layer $\int S_i\,dz = v(n_{i,\text{ch}} - n_{i,\text{tip}})$ which is obtained after integrating $-v\partial_z n_i = S_i$ (from equation (4.3)) across the charge layer. Finally, since $n_{i,\text{tip}} \ll n_{i,\text{ch}}$ we have omitted the dependency on $n_{i,\text{tip}}$.

$\mathcal{A}(\mathbf{r}')$ is a function that can account for the fact that the impact ionization and thus the photon radiation in the charge layer diminishes in the off-axis direction. However, for simplicity we take $\mathcal{A}(\mathbf{r}') = 1$. Naturally this will slightly overestimate photon radiation.

4.4.3   Solving the electron density in the avalanche zone

We will now solve equation (4.35). To do so we first introduce the short hand notation

$$\partial_z n_e + \lambda(z) n_e = -K(z), \tag{4.40}$$

with $\lambda(z)$ the electron avalanche growth function

$$\lambda(z) = \frac{v_{\mathrm{dr}}(E(z))}{v + v_{\mathrm{dr}}(E(z))} \left(\alpha_{\mathrm{eff}}(E(z)) + \frac{\partial_z \mu}{\mu} \right), \tag{4.41}$$

and $K(z)$ the photoelectron source term

$$K(z) = \frac{S_{ph}(z)}{v + v_{\mathrm{dr}}(E(z))}, \tag{4.42}$$

in the external electric field $E(z)$ from equation (4.36). $S_{ph}(z)$ is determined by equations (4.37) – (4.39) as a surface-integral corresponding to the parametrized charge layer. For given I^*, equation (4.40) is an ordinary differential equation for n_e that is solved as

$$n_e(z) = \int_z^\infty K(y) \, e^{\int_z^y \lambda(x) \, dx} \, dy. \tag{4.43}$$

This solution can be interpreted as a superposition of electron avalanches. The electron avalanches are continuously created by a photoelectron density K. The avalanches grow in the electric field as described by λ which contains the effects of impact ionization α_{eff} and of electron mobility $\mu(E)$.

For further evaluation, it is interesting to discuss the structure of this solution and the implications for the electron and ion densities at the front and back end of the charge layer, z_{tip} and z_{ch}. We find that equation (4.43) can be rewritten as

$$\frac{n_{e,\mathrm{tip}}}{n_{i,\mathrm{ch}}} = F(v, R, E_{\mathrm{max}}, E_{\mathrm{bg}}), \tag{4.44}$$

with an explicit equation for the function F that does not depend on any electron or ion densities. Here R, E_{max} and E_{bg} determine the electric field $E(z)$ in the avalanche zone

according to (4.36). That F does not depend on the particle densities, is due to the linear nature of the avalanche zone without local space charge effects: twice as many photons emitted from the charge layer will create twice as many avalanches and twice as many electrons arriving at z_{tip} which in turn emit twice as many photons from the charge layer.

The explicit equation for the function F is

$$F = \frac{p_q}{p + p_q} \, \xi \int_{z_{\text{tip}}}^{\infty} \frac{v}{v + v_{\text{dr}}(y)} e^{\int_{z_{\text{tip}}}^{y} \lambda(x)\,dx} \iint_S \mathcal{A}(\mathbf{r}') \frac{f(|y\mathbf{e}_z - \mathbf{r}'|)}{4\pi|y\mathbf{e}_z - \mathbf{r}'|^2} \, d^2 r' \, dy, \qquad (4.45)$$

where the first line contains the field dependent electron dynamics on the streamer axis, and the second line the field independent photon dynamics between the charge layer and the axis.

An analysis of the avalanche zone along similar lines was proposed in [138], but they only account for photons produced in the avalanche zone and neglect the contribution from the charge layer. However figure 4.3 shows that ionization in the charge layer, and therefore the associated photon production, is far more important. In our approach we do take the charge layer as the dominant photon source. The same reasoning was also given in [139, 133]. In addition to this we have derived an improved photoionization balance on the basis of consistent electrodynamics in the charge layer and avalanche zone, equation (4.44). This formula replaces the photoionization balance proposed in [138]. We finally remark that the balance between the dynamics of photons and of electron avalanches resembles a self-sustained DC discharge, with the difference that the anode is replaced by a propagating streamer head with self-consistent shape.

4.5 The electrostatic field and the head potential

4.5.1 Streamer head potential

As recalled in [9], the electrostatic approximation for the electric field $\mathbf{E} = -\nabla\varphi$ is sufficient for streamer physics. Therefore the line integral between any two points is independent of the path taken between them

$$\int_C \mathbf{E} \cdot dl = \phi(\mathbf{r}) - \phi(\mathbf{r}'), \qquad (4.46)$$

with C any continuous curve which starts at $\mathbf{r}$ and ends at $\mathbf{r}'$. This concept will be applied to derive a relation between the electrostatic properties of the channel and the head.

We shall use equation (4.46) to solve two path-integrals, the first corresponding only to the background field and the second to the field with a streamer present. In both cases C equals

the axis of propagation, i.e. ζ-axis, which gives $\mathbf{r} = 0$ and $\mathbf{r}'$ on the opposing electrode. For the streamers in this work ζ_{tip} is far away from the opposing electrode, which means that boundary effects are negligible and we can take $\mathbf{r}'$ at infinity. When we subtract the two integrals we find

$$\int_0^\infty (E(\zeta) - E_{\text{bg}})\, d\zeta = 0, \tag{4.47}$$

since the potential at $\mathbf{r}$ and $\mathbf{r}'$ is the same and therefore the right-hand side vanishes. This fundamental property has been considered by previous authors [147, 138, 132, 131, 148]. Equation (4.47) will be split in two intervals with different dynamics, namely: the streamer channel $[0, \zeta_{\text{tip}}]$ and the avalanche zone $[\zeta_{\text{tip}}, \infty)$. We shall treat each of these intervals separately.

Potential across the channel

The potential across the channel requires different treatment for steady and accelerating streamers.

For a steady streamer the channel electric field decays back to the background field. In general the profile of the channel electric field is determined by currents in the streamer channel [10, 129]. For now, modelling the charge distribution within the channel is not considered. Instead, we suggest a plausible channel electric field profile for steady streamers. In section 4.2.3 we have discussed how dynamics in the channel are related to an electron loss time scale τ, which in turn defines an electron loss length L_{loss}. We use these concepts to impose

$$E(\zeta) = E_{\text{bg}} + (E_{\text{ch}} - E_{\text{bg}}) \exp\left(\frac{\zeta - \zeta_{\text{ch}}}{L_{\text{loss}}}\right),$$

$$\text{for } \zeta < \zeta_{\text{ch}}. \tag{4.48}$$

Substituting this into equation (4.47) results in:

$$\int_0^{\zeta_{\text{ch}}} (E(\zeta) - E_{\text{bg}})\, d\zeta = L_{\text{loss}}\left(E_{\text{bg}} - E_{\text{ch}}\right). \tag{4.49}$$

For the accelerating streamers considered in this work we have $L \ll L_{\text{loss}}$, which means it is more reasonable to work with an averaged channel electric field $\bar{E}_{\text{ch}}$. By holding that

$E_{\text{ch}} = \bar{E}_{\text{ch}}$ over the length of the channel we can obtain a similar result

$$\int_0^{\zeta_{\text{ch}}} \left(E(\zeta) - E_{\text{bg}}\right) d\zeta = L\left(E_{\text{bg}} - \bar{E}_{\text{ch}}\right). \tag{4.50}$$

Potential across the avalanche zone

In the avalanche zone the electric field was approximated by that of a uniformly charged sphere, equation (4.36). Using this the potential across the avalanche zone simplifies approximately to

$$\int_{\zeta_{\text{tip}}}^{\infty} \left(E(\zeta) - E_{\text{bg}}\right) d\zeta = R(E_{\text{max}} - E_{\text{bg}}). \tag{4.51}$$

This gives the final result

$$R(E_{\text{max}} - E_{\text{bg}}) = L\left(E_{\text{bg}} - E_{\text{ch}}\right). \tag{4.52}$$

To keep notation simple we have no longer discerned between L_{loss} or $\bar{E}_{\text{ch}}$ for the separate cases of steady and accelerating streamers.

4.6   Solving the approximations

4.6.1   Solution method

We now assume that velocity v, radius of curvature R, length L and background electric field E_{bg} are given, for example by experimental measurements, and we estimate four unknowns that are much more difficult to measure: ionization density $n_{i,\text{ch}}$, maximal electric field E_{max}, channel field E_{ch}, and charge layer width ℓ. To that end we shall formulate a system of four relations from which these unknowns will be determined.

In the previous sections we have derived equations (4.21) and (4.33) by analyzing the dynamics of the charge layer $z_{\text{ch}} \leq z < z_{\text{tip}}$, where $z_{\text{tip,ch}} = R \pm \ell/2$. These are the first and second relations. On the basis of electrostatics we have related the head potential to the streamer length in equation (4.52), which is the third relation. Finally, we require that charge layer and avalanche zone electron dynamics are consistent (cf. section 4.4.3). This introduces

the last relation, namely equation (4.44). For convenience, we repeat our relations here:

$$j_{e,\text{ch}} = j_{e,\text{tip}}, \tag{4.53}$$

$$v\epsilon_0(E_{\max} - E_{\text{ch}}) = \int_{z_{\text{ch}}}^{z_{\text{tip}}} e(j_{e,\text{tip}} - j_e)\,dz, \tag{4.54}$$

$$R(E_{\max} - E_{\text{bg}}) = L\left(E_{\text{bg}} - E_{\text{ch}}\right), \tag{4.55}$$

$$\frac{n_{e,\text{tip}}}{n_{i,\text{ch}}} = F(v, R, E_{\max}, E_{\text{bg}}). \tag{4.56}$$

The function F is defined in equation (4.45) and the electron current density is defined as $j_e = -\mu n_e E$. The above system of equations has 8 independent parameters:

$$v,\ R,\ L,\ E_{\text{bg}},\ n_{i,ch},\ E_{\max},\ E_{\text{ch}}\ \text{and}\ \ell. \tag{4.57}$$

All other quantities are determined by these 8 parameters. To see this, we summarize our approximations in the two regions:

- In the avalanche zone ($z \geq z_{\text{tip}}$) the electric field and the electron density are approximated by (equations (4.36) and (4.43))

$$E(z) = \frac{z_{\text{tip}}^2(E_{\max} - E_{\text{bg}})}{z^2} + E_{\text{bg}}, \tag{4.58}$$

$$n_e(z) = \int_z^\infty K(y)\, e^{\int_z^y \lambda(x)\,dx}\,dy, \tag{4.59}$$

$$\text{for } z \geq z_{\text{tip}}.$$

Notably, the function $K(y)$ (equation (4.42)) accounts for the production of photoelectrons and is proportional to $n_{i,ch}$. The electron density and the electric field by definition give j_e and therefore $j_{e,\text{tip}}$. Finally, we have assumed that space charge effects are negligible in the entire avalanche zone. We therefore also assume quasi-neutrality at the tip $n_{i,\text{tip}} \approx n_{e,\text{tip}}$.

- In the charge layer ($z_{ch} \leq z < z_{tip}$) the electric field and densities are approximated by (equations (4.29), (4.26), (4.32))

$$E(z) = E_{max} - \frac{e}{\epsilon_0} \int_z^{z_{tip}} n_q(z)dz, \tag{4.60}$$

$$n_i(z) = n_{i,tip} + \frac{\epsilon_0}{e} \int_{E(z)}^{E_{max}} \alpha_{eff}(E)\, dE + \frac{1}{ev} \int_z^{z_{tip}} \alpha_{eff}(E(z)) j_{tot}\, dz, \tag{4.61}$$

$$n_e(z) = \frac{v n_i(z) - j_{e,ch}}{v + v_{dr}}, \tag{4.62}$$

$$\text{for } z_{ch} \leq z < z_{tip},$$

where n_q in equation (4.60) is a parametrization given in equation (4.27). The quantities $n_{i,tip}$ and $j_{e,tip}$ are determined by the avalanche zone. Quasi-neutrality in the channel gives $n_{i,ch} = n_{e,ch}$. Thus we can evaluate j_{tot} and j_e within the charge layer.

The objective is then to determine 4 parameters in (4.57), since we consider that $(v,\ R,\ L, E_{bg})$ are fixed by observations. The remaining four, which we call $m = (n_{i,ch},\ E_{max},\ E_{ch},\ \ell)$, have to satisfy our relations (4.53)-(4.56). Solving this system of equations is equivalent to finding the roots of the four-dimensional vector-function $\mathcal{S}$, which is defined as the difference between the left- and right-hand sides of equations (4.53)-(4.56). Thus m is a consistent solution if it satisfies

$$\mathcal{S}(m) = 0. \tag{4.63}$$

Due to the complexity of $\mathcal{S}$ we employ an iterative root-finding algorithm that solves equation (4.63) using a modification of the Levenberg-Marquardt algorithm [149]. Such an algorithm starts from an initial guess m^0 and produces a sequence of values m^k that converges to the root. We emphasize again that the input parameters v, R, L and E_{bg} in addition to m^k are sufficient to evaluate $\mathcal{S}(m^k)$. Moreover, changing the initial guess seems to have no effect on the obtained solution m, suggesting that the solution m is unique. We observe the same in numerical simulations [131, 132].

4.6.2   Results

Steady streamer

In this section we will compare the approximated $n_e(z)$, $n_{i,ch}$, E_{max}, E_{ch} and $\tilde{\ell}$ with numerical simulations. We shall first do this comparison for the steady streamer. To obtain these results we extracted $E_{bg} = 4.5$ kV cm^{-1}, $v = 0.076$ mm ns^{-1}, $R = 49\ \mu$m and $L_{loss} = 3.8$ mm from simulation (see figure (4.5)) and used these to solve equation (4.63).
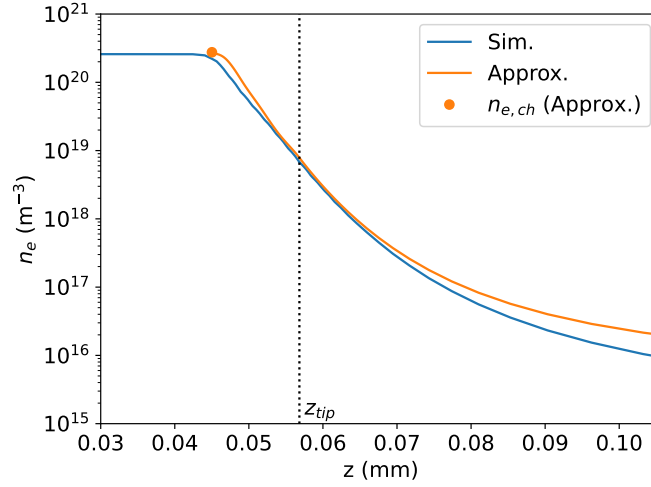
Fig. 4.8 Our approximation (orange) for the electron density compared to numerical results (blue) of a steady streamer simulation. The applied background field is 4.5 kV cm^{-1}. The approximated parameters used to make this comparison are evaluated in figure (4.9)

In figure 4.8 we show our approximation for the axial electron density of the steady streamer (equations (4.32) and (4.43)). The approximated electron density was overlaid onto the results from the numerical simulation such that the respective z_{tip} overlap. We observe that our analytic formulae for the electron density profile in the avalanche zone reproduces the profile obtained from simulation well. In this figure we can also observe that more than 95% of the ionization occurs in the charge layer. This underlines our earlier arguments that ionization predominantly occurs in the charge layer and that photons originating from the avalanche zone can be neglected.

The approximated parameters $n_{i,\text{ch}}$, E_{max}, E_{ch} and $\tilde{\ell}$ that were derived in this evaluation are shown in figure 4.9. We observe good agreement with a maximum relative error of about 30% for the prediction of $\tilde{\ell}$. The other parameters agree within 25%.

Accelerating streamers

As discussed in the introduction, we shall now apply our analysis developed for steady streamers to accelerating streamers. We include results, calculated in the same manner, for streamers at background electric fields of 10, 14 and 24 kV cm^{-1}. The corresponding velocity and radius as a function of streamer length were already shown in figure 4.5.

The approximated parameters are included in figure 4.9. In this case we also observe good agreement with relative errors of at most several tens of percent. Only at 24 kV cm^{-1} do
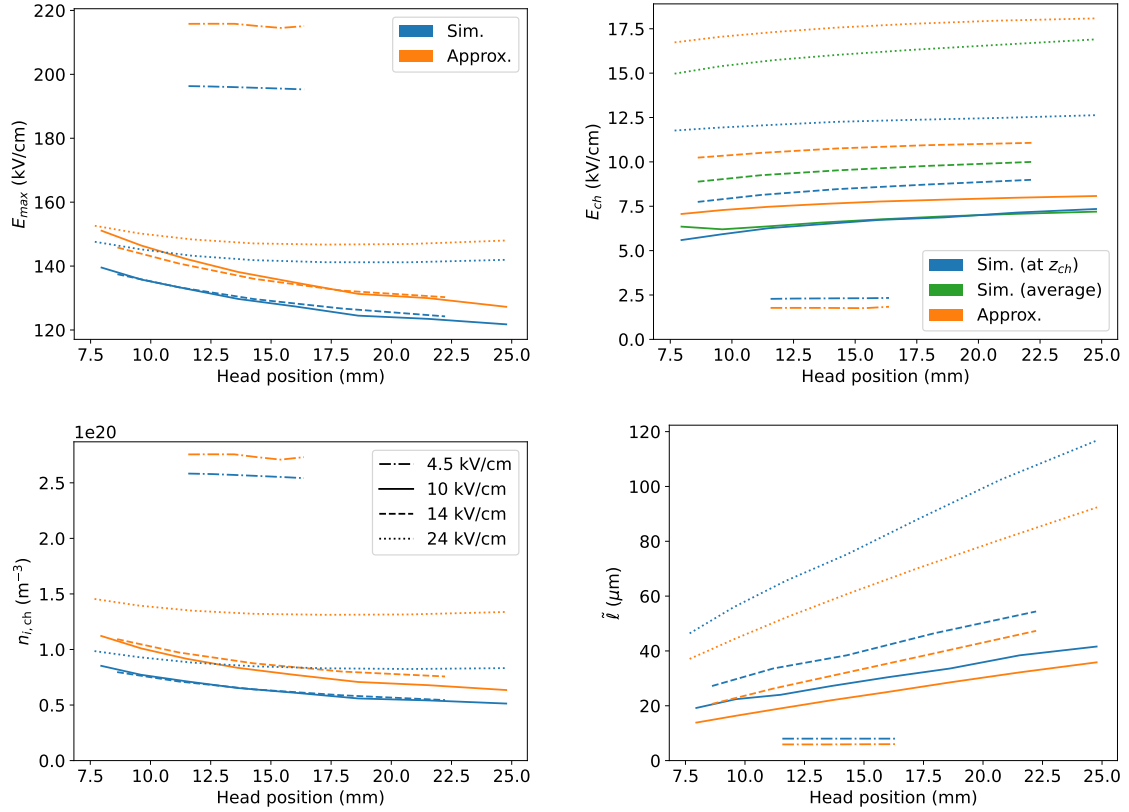
Fig. 4.9 Comparison of simulations (blue, green) and our approximations (orange) for streamers with varying head positions in different background fields E_{bg}. E_{bg}, L, R and v were taken from the simulations and used to calculate the plotted approximations from (4.63). The plotted quantities are the maximum electric field E_{max}, the (average) channel electric fields E_{ch}, the degree of ionization $n_{i,ch}$ and the charge layer width $\tilde{\ell}$. The four background electric fields E_{bg} are plotted as $-\cdot-\cdot$ for $4.5\,\mathrm{kV\,cm^{-1}}$ (steady), —— for $10\,\mathrm{kV\,cm^{-1}}$, $---$ for $14\,\mathrm{kV\,cm^{-1}}$, and $\cdots$ for $24\,\mathrm{kV\,cm^{-1}}$).

we have relative errors of about $50 - 60\%$ for the estimation of $n_{i,\mathrm{ch}}$. Furthermore, we also illustrate the error introduced by our simplified treatment of the channel electric fields. For accelerating streamers we have included both E_{ch} and the averaged $\bar{E}_{\mathrm{ch}}$ in figure 4.9. In section 4.5 we have used $E_{\mathrm{ch}} = \bar{E}_{\mathrm{ch}}$ in order to obtain an equation for the channel electric fields without resolving the entire charge transport dynamics of the channel. However, this approximation is generally not true and the accuracy is worst for the $24 \ \mathrm{kV} \ \mathrm{cm}^{-1}$ case. This has various causes, such as a persisting neutral seed (i.e. due to shorter propagation times the influence of initial conditions still persist), actual inhomogeneities in the channel or the influence of boundary conditions.

Overall, our model is also able to estimate the properties of streamers in higher background fields. Evidently, approximating the charge layers of accelerating streamer heads as planar fronts in a steady state gives reasonable results.

4.7   Summary and outlook

4.7.1   Summary

In this work we have proposed a model that characterizes a single positive air streamer on the basis of observable parameters. Overall, our approximations exhibit good agreement with numerical simulations of a steady streamer with typical relative errors below 30%. For accelerating streamers the errors are slightly higher, with a maximum deviation up to 60% in the highest considered background field.

Our most important theoretical contributions are:

- We have constructed a self-contained axial model that can approximate macroscopic properties of steady streamer heads. This model also gives good results for accelerating streamer heads.

- We have shown how the quantities $n_{i,\mathrm{ch}}$, $E_{\max}$, E_{ch} and ℓ can be determined from the more easily observable parameters R, v, L and E_{bg}.

- We have provided a formula for the ionization density of a streamer. Notably this formula contains the contribution due to a non-zero total current density and is about twice as high as the classical formula.

- We have given a self-consistent description of electron dynamics which includes the implicit contribution due to photoelectrons produced in the avalanche zone.

4.7.2   Outlook

For future work we recommend three possible improvements:

- We have not considered explicitly solving the dynamics of the charge layer. Instead we have accounted for these dynamics by heuristic parameterizations. However, a numerical approach that resolves densities and the electric field inside the charge layer can be expected to improve the accuracy. Moreover such an approach could replace a number of parameterizations, which would lead to a more precise representation of streamer dynamics.

- We have used two approaches for the channel electric fields. For accelerating streamers we have used an average value $\bar{E}_{\mathrm{ch}} = E_{\mathrm{ch}}$, and for steady streamers we have used an exponential decay with a prescribed length scale L_{loss}. These clearly have their limitations. In future work we aim to combine the insights obtained in this research with models that explicitly evaluate the dynamics of the streamer channel, such as [129].

- All derivations in this work assume that the dynamics of the charge layer can be approximated in a planar front setting, since the dimensionless parameter ℓ/R is typically small. A systematic expansion in terms of ℓ/R will likely improve the accuracy of our model.

Finally we comment on the significance of our work regarding the development of accurate streamer tree models such as [10, 129]. The current limitation of these models is that they lack a self-consistent description of velocity and radius of a streamer. These parameters are often imposed. However, our model can be combined with a tree model in order to overcome this critical limitation for positive streamers.

Chapter 5

Approximating steady positive air streamers with an axial model

We develop an axial model for single steadily propagating positive streamers in air from a plasma fluid model. We characterize the solutions of the axial model by macroscopic parameters, and we find that these parameters are fully determined by the applied background electric field E_{bg} and by the condition of steady motion. Next we calculate steady streamers in the range of $E_{bg} = 4.0 - 5.0 \, \text{kV cm}^{-1}$ and find reasonable agreement with numerical simulations. This indicates that our axial model captures the relevant physics of steady streamers using a simple macroscopic representation. Our work is a crucial step towards the development of efficient axial multi-streamer models.

5.1   Introduction

Streamer discharges commonly occur as the precursors of sparks. An overview of the physics of streamer discharges is given in [9]. In high-voltage switching, streamers are unwanted since they facilitate the formation of damaging arcs [150]. Streamers are also found in earth's atmosphere as sprites and corona bursts [2, 151, 152].

5.1.1   The need for new models

Streamer discharges are challenging to simulate due to their multiscale nature. As such there is a strong motivation to reduce the complexity of the model. This has sparked renewed interest in so-called 1.5D models. These models are cross-section averaged and depend on macroscopic parameters of the head, such as the radius R and velocity v, which are often fixed and only accounted for phenomenologically. For axisymmetric streamers this approach is essentially one-dimensional, except that the head curvature is taken into account, hence the term "1.5D". Examples of phenomenological 1.5D models are [153–157]. Recent improvements provide quantitative descriptions of various important mechanisms [10, 129, 133, 139, 158]. When such models are extended to three-dimensional branched streamer discharges, as is done in [10], they drastically simplify the computational complexity.

1.5D models are attractive, but there are still open problems. The central issue is that there is no fundamental approach to calculating macroscopic parameters of the streamer head, e.g. radius R and velocity v. These parameters can vary by 2 or 3 orders of magnitude in the same gas, depending on the applied electric field and initial conditions [9]. Without a physics-based method of calculating macroscopic parameters it is not possible to give a physical basis for 1.5D models, which seriously limits their impact.

5.1.2   Application of steady streamers

Being able to understand when a streamer is able to cross a gap is important to many applications. Historically, the empirical notion of the stability field was used to refer to the lowest background electric field in which gap crossing is observed [159], see also [160–163]. Streamers propagating in such low fields can be in a steady state, in the sense that properties such as radius, velocity and length do not change over time [130–132]. In [164] it was argued that steady streamers are not unique. In later works [131, 132] this was confirmed as steady streamers were found by numerical simulation for different E_{bg} ranging from 4.0–5.5 kV cm^{-1} (positive polarity) and 9.2–15.8 kV cm^{-1} (negative) in air at 1 bar and 300 K. The study of steady streamers gives a better interpretation of the concept of the

stability field. Another reason to study steady streamers is because they are a mathematically convenient test case for the development of axial models, since steady streamers are at rest in a co-moving frame.

5.1.3   Our work

The goal of this work is to derive a 1.5D model which includes a physics-based description of macroscopic parameters of steady streamer heads. This distinguishes our approach from existing phenomenological 1.5D models. More specifically, we combine two existing approaches that precisely complement each other:

- For the modelling of the dynamics of the streamer channel we base our approach on [129]. This model calculates the longitudinal charge distribution and electric fields for streamers with a prescribed R, v and ionization density $n_{i,\mathrm{ch}}$.

- To obtain the head properties R, v, $n_{i,\mathrm{ch}}$ and the width of the charge layer ℓ we use our earlier work for the calculation of macroscopic parameters (Chapter 4).

When applied within the context of steady streamers in air, these two models combined are able to describe their properties as a function of only the applied background field E_{bg}. Our approach is also a stepping stone towards the development of more sophisticated axial models.

In section 5.2 we outline a plasma fluid streamer model and in section 5.3 derive our axial model from it. In section 5.4 we discuss the implementation. Finally, in section 5.5 we analyze the results and validate against numerical results of positive steady streamers.

5.2   Basic equations (fluid model)

The basic equations are given by a fluid streamer model with local field approximation. The electron density evolves according to a drift-diffusion-reaction equation

$$\partial_t n_e = \nabla \cdot (\mu n_e \mathbf{E} + D \nabla n_e) + S, \tag{5.1}$$

with $\mathbf{E}$ the electric field, $\mu(E)$ the electron mobility, $D(E)$ the electron diffusion coefficient and S the sum of source terms, given by

$$S = S_{\mathrm{ion}} + S_{\mathrm{att}} + S_{\mathrm{detach}} + S_{\mathrm{recom}} + S_{\mathrm{ph}} \tag{5.2}$$

Table 5.1 Reactions included in the model. E/N is the reduced electric field in units of Townsend, T_e is the electron temperature which is given in terms of the mean electron energy ϵ_e computed by Bolsig+: $T_e = 2\epsilon_e/3k_B$. This reaction set is taken from [131].

No.	Reaction	Rate coefficient	Reference
1	$e + N_2 \rightarrow e + e + N_2^+$ (15.6 eV)	$k_1(E/N)$	[14, 143]
2	$e + N_2 \rightarrow e + e + N_2^+$ (18.8 eV)	$k_2(E/N)$	[14, 143]
3	$e + O_2 \rightarrow e + e + O_2^+$	$k_3(E/N)$	[14, 143]
4	$e + O_2 + O_2 \rightarrow O_2^- + O_2$	$k_4(E/N)$	[14, 143]
5	$e + O_2 \rightarrow O^- + O$	$k_5(E/N)$	[14, 143]
6	$O_2^- + N_2 \rightarrow O_2 + N_2 + e$	$k_6 = 1.13 \cdot 10^{-25} \text{ m}^3\text{s}^{-1}$	[165]
7	$O_2^- + O_2 \rightarrow O_2 + O_2 + e$	$k_7 = 2.20 \cdot 10^{-24} \text{ m}^3\text{s}^{-1}$	[165]
8	$O^- + N_2 \rightarrow e + N_2O$	$k_8 = 1.16 \cdot 10^{-18} \exp(-(\frac{48.9}{11+E/N})^2) \text{ m}^3\text{s}^{-1}$	[166]
9	$O^- + O_2 \rightarrow O_2^- + O$	$k_9 = 6.96 \cdot 10^{-17} \exp(-(\frac{198}{5.6+E/N})^2) \text{ m}^3\text{s}^{-1}$	[166]
10	$O^- + O_2 + M \rightarrow O_3^- + M$	$k_{10} = 1.10 \cdot 10^{-42} \exp(-(\frac{E/N}{65})^2) \text{ m}^6\text{s}^{-1}$	[166]
11	$N_2^+ + N_2 + M \rightarrow N_4^+ + M$	$k_{11} = 5.0 \cdot 10^{-41} \text{ m}^6\text{s}^{-1}$	[167]
12	$N_4^+ + O_2 \rightarrow O_2^+ + N_2 + N_2$	$k_{12} = 2.5 \cdot 10^{-16} \text{ m}^3\text{s}^{-1}$	[167]
13	$O_2^+ + O_2 + M \rightarrow O_4^+ + M$	$k_{13} = 2.4 \cdot 10^{-42} \text{ m}^6\text{s}^{-1}$	[167]
14	$e + O_4^+ \rightarrow O_2 + O_2$	$k_{14} = 1.4 \cdot 10^{-12} (\frac{300\,K}{T_e})^{1/2} \text{ m}^3\text{s}^{-1}$	[165]
15	$e + N_4^+ \rightarrow N_2 + N_2$	$k_{15} = 2.0 \cdot 10^{-12} (\frac{300\,K}{T_e})^{1/2} \text{ m}^3\text{s}^{-1}$	[165]

which are, respectively, the source terms for impact ionization, attachment, detachment, electron-ion recombination and photoionization. All source terms, except S_{ph}, are determined from a set of cross sections or chemical reactions. The cross sections are taken from the Phelps database [143] and are used by Bolsig+ [14, 109] to calculate transport and reaction coefficients under the assumption that the evolution of the electron density follows an exponential temporal growth [18]. Additionally we calculate rate coefficients k_1 to k_5 which characterize individual ionization and attachment reactions, see table 5.1. Furthermore the terms S_{detach} and S_{recomb} are obtained from secondary reactions involving ions. The reactions included in the model are shown in table 5.1. The cross section and chemical reaction data is the same as used in [131] with which we compare our results in later sections. However, when ion conversion is not deemed important we can work with ionization and attachment sources as functions of reaction coefficients

$$S_{\text{ion}} = |\mathbf{j}_e|\alpha(E) \quad \text{and} \quad S_{\text{att}} = |\mathbf{j}_e|\eta(E), \tag{5.3}$$

where $\mathbf{j}_e = -\mu n_e \mathbf{E}$ is the drift current density of electrons, e is the elementary charge, $\alpha(E)$ is the ionization coefficient and $\eta(E)$ is the attachment coefficient. These two terms can be lumped into S_{eff} using the effective ionization coefficient $\alpha_{\text{eff}} = \alpha - \eta$.

We follow a similar approach for the ions. The density of the jth species follows from

$$\partial_t n_j = S_j, \tag{5.4}$$

where S_j contains all reactions affecting n_j. Note that we consider ions to be immobile. The net charge of all ions is denoted by $e n_i = e(n_{i,+} - n_{i,-})$, where the subscript $\pm$ denotes the sign of the ion charge.

The photoionization source term in a volume V is given by

$$S_{\text{ph}}(\mathbf{r}) = \iiint_V \frac{I(\mathbf{r}')f(|\mathbf{r} - \mathbf{r}'|)}{4\pi|\mathbf{r} - \mathbf{r}'|^2}d^3r', \tag{5.5}$$

with $I(\mathbf{r}')$ the source of ionizing photons, $f(r)$ the absorption function and $4\pi|\mathbf{r} - \mathbf{r}'|^2$ is a geometric factor. Following Zheleznyak's model [13, 115], $I(\mathbf{r})$ can be expressed as

$$I(\mathbf{r}) = \frac{p_q}{p + p_q}\xi S_{\text{ion}}(\mathbf{r}), \tag{5.6}$$

with p the actual pressure, $p_q = 40$ mbar the quenching pressure of the gas-mixture, and $\xi = 0.075$ (taken from [130]) a proportionality factor relating impact excitation to impact
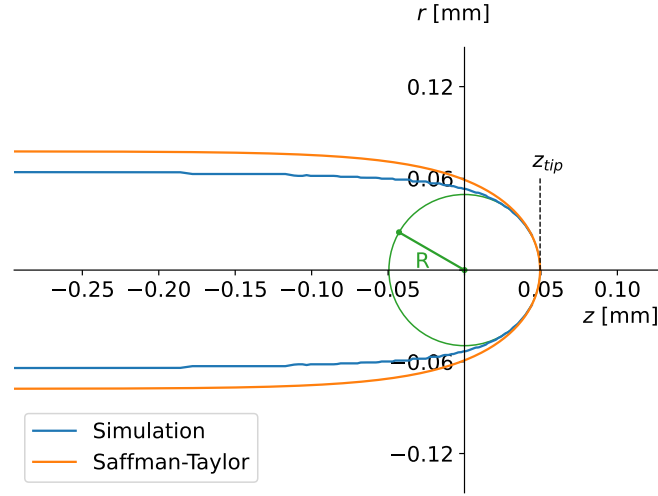
Fig. 5.1 The axisymmetric charge layer from simulation and from equation (5.10) (Saffman-Taylor). The applied electric field is $E_{bg} = 4.5$ kV cm^{-1}. We also show the sphere with a radius of curvature R that best approximates the charge layer at the tip. The charge layer is not resolved since this is the outer scale representation.

ionization S_{ion}. The absorption function $f(r)$ is given by

$$f(r) = \frac{\exp(-\chi_{min} p_{O_2} r) - \exp(-\chi_{max} p_{O_2} r)}{r \ln(\chi_{max}/\chi_{min})}, \tag{5.7}$$

with $\chi_{max} = 150$ (mm bar)$^{-1}$, $\chi_{min} = 2.6$ (mm bar)$^{-1}$, and p_{O_2} is the partial pressure of oxygen. For air at 300 K and 1 bar, the corresponding absorption lengths are 33 μm and 1.9 mm. The coefficients p_q, ξ, χ_{max} and χ_{min} are the same as in the numerical models used to obtain the reference solutions in [131] and Chapter 4.

The electric field follows from Poisson's equation for the electric potential ϕ

$$\epsilon_0 \nabla^2 \phi = -e(n_{i,+} - n_{i,-} - n_e), \tag{5.8}$$

$$\mathbf{E} = -\nabla \phi, \tag{5.9}$$

with ϵ_0 the dielectric constant.

5.3 Axial model description

Equations (5.1)-(5.9) form the starting point of our derivation of an axial model. The goal is to find approximate solutions to the basic equations parametrized by the central axis.

Furthermore our approximations will be functions of several macroscopic parameters that will be calculated self-consistently.

5.3.1   Streamer shape and distinct regions

We model the steady streamer as an axially symmetric filament, propagating with constant velocity v, oriented along the z-direction in a co-moving coordinate frame. The coordinates and the origin are shown in figure 5.1. All charges are situated in a thin charge layer surrounding the conductive interior. Since the width of this layer is much smaller than the radius we shall approximate it as a charged surface and we assume a shape given by the function $\mathcal{R}(z)$. Note that this, by construction, introduces a discontinuity between the solutions on the outer scale. This notably occurs at the tip, which is denoted by z_{tip}.

Next, we parameterize the shape $\mathcal{R}(z)$ as a function of z. To the best of our knowledge, there is currently no general shape function for three-dimensional streamers with photoionization known. Here we use the Saffman-Taylor shape function found in [168]

$$\mathcal{R}(z) = \frac{R_\infty}{\pi} \arccos\left(2\exp\left(\frac{\pi(z_{\mathrm{tip}} - z)}{R_\infty}\right) - 1\right),$$

$$\text{for } z < z_{\mathrm{tip}}, \tag{5.10}$$

where R_∞ is the asymptotic radius of the channel at $z \to -\infty$ and, as mentioned before, z_{tip} is the location of the streamer tip. This shape function was found to approximate negative streamers without photoionization in a 2D Cartesian periodic array very well [168]. From this we can calculate the radius of curvature of the head R. R is defined as the radius of the sphere that gives the best approximation of the charge layer profile at the tip. Calculating the curvature of $\mathcal{R}(z)$ at z_{tip} gives

$$R_\infty = \frac{\pi}{2}R. \tag{5.11}$$

We can also extract R from numerical simulations by fitting a circle through the maximum (for each z) of the charge density in the interval $[z_{\mathrm{tip}} - 2\ell, z_{\mathrm{tip}}]$, where ℓ is the width of the charge layer.

In figure 5.1 we compare equation (5.10) with numerical simulations of a steady streamer at $E_{\mathrm{bg}} = 4.5$ kV cm^{-1} from Chapter 4. The outline of the charge layer is given by the r-coordinate of the maximum of charge density for each z. Additionally, we extracted R from simulations and used equation (5.11) in order to evaluate equation (5.10), which is also shown. This yields good agreement near the tip, but some overestimation of the channel radius.

Continuing, streamers can be decomposed into three distinct regions which are governed by different dynamics. We will treat each region separately and formulate axial approximations of their dynamics. These regions are:

1. *The avalanche zone* is the region directly ahead of the streamer tip: $z > z_{\text{tip}}$. Here the electric field is above breakdown. Thus, avalanches created by photoionization grow as they approach the streamer head. This facilitates the propagation of a positive streamer.

2. *The charge layer* is a layer of positive charge surrounding and screening the channel. Note that this region is approximated as infinitely thin in figure 5.1. Due to the curvature at z_{tip} we have a high electric field enhancement and subsequently a high ionization rate.

3. *The channel* is the conductive interior of the plasma filament: $z < z_{\text{tip}}$. In this region an electron current flows along the channel. For steady streamers, the loss of conductivity is an important physical mechanism affecting the current. Furthermore, the charge distribution in the channel determines the axial electric field, which couples the dynamics of the channel to the aforementioned regions.

Each of these regions has been investigated before. A model for the evolution of charged species in the channel has been derived in [10, 129] and the dynamics of the ionization front and the avalanche zone have been investigated in Chapter 4. In remainder of this section we will give an overview of the modelling approach of each region in the context of steady streamers. Throughout this chapter, and in the previous investigations, currents due to diffusion are neglected.

5.3.2 The avalanche zone $(z > z_{\text{tip}})$

Photoionization:

The propagation of positive streamers is dependent on the generation of free electrons in the region ahead of the tip. In air without background ionization, the ionization of oxygen molecules by energetic photons is the dominant mechanism for the generation of free electrons. These photons are produced by energetic collisions mostly occurring in the charge layer at the head. We approximate the head as a semispherical surface $\mathcal{S}$ (see figure 4.7), which corresponds to the right half of the tangent sphere shown in figure 5.1. From Zhelezniaks photoionization model [13] we derive an axial (i.e. $r = 0$) photoelectron source

term on the axis of the avalanche zone

$$S_{ph}(z) = \iint_{\mathcal{S}} \frac{I(\mathbf{r}')f(|z\mathbf{e}_z - \mathbf{r}'|)}{4\pi|z\mathbf{e}_z - \mathbf{r}'|^2} d^2r', \tag{5.12}$$

with $\mathbf{e}_z$ the unit vector in the z-direction, and where the coordinates $\mathbf{r}'$ now lie on the semispherical surface $\mathcal{S}$. In our axial model we write the source of ionizing photons as

$$I(\mathbf{r}) = \mathcal{A}(\mathbf{r})I^*, \tag{5.13}$$

where $\mathcal{A}(\mathbf{r})$ is a coefficient representing the non-uniformity of photon emission across the semispherical head for which we assume

$$\mathcal{A}(\mathbf{r}) = 1 - \left(\frac{r}{R}\right)^2,$$
$$\text{for } r \leq R, \tag{5.14}$$

so that it vanishes at the edges of the head and where I^* is the magnitude

$$I^* = \frac{p_q}{p + p_q} \xi v n_{i,\mathrm{ch}}, \tag{5.15}$$

with $n_{i,\mathrm{ch}}$ the ion density in the channel (i.e. the ionization density). Note that our choice of $\mathcal{A}(\mathbf{r})$ is different than in Chapter 4, where we used $\mathcal{A} = 1$ for simplicity.

Electron density:

The term $S_{ph}(z)$ represents the source of photoelectrons that initialize electron avalanche dynamics in the region ahead of the streamer. Because the influence of local charges is negligible, the avalanches develop in a field that is externally determined. Since the head is approximately spherical, we approximate the electric field profile in the avalanche zone by a uniformly charged sphere with radius R_∞

$$E(z) = \frac{R_\infty^2(E_{\max} - E_{\mathrm{bg}})}{(R_\infty + z - z_{\mathrm{tip}})^2} + E_{\mathrm{bg}},$$
$$\text{for } z > z_{\mathrm{tip}}. \tag{5.16}$$

Here we use R_∞ instead of R as was done in Chapter 4, since no valid solutions for steady streamers could be found when using R, i.e. equation (4.36). A possible explanation is that approximations such as (4.36) underestimate the head potential which could prevent

convergence of the solution method. If so, then introducing the larger radius R_∞ might compensate for this underestimation without addressing the underlying issues. Further consideration is required to find improved alternatives to approximations such as equations (5.16) and (4.36).

Next we recall from section 4.4 that we can reformulate the electron transport equation (5.1) for steady streamers as

$$\partial_z n_e + \lambda(z) n_e = -K(z), \tag{5.17}$$

where K represents the generation of photoelectrons and λ governs electron avalanche growth

$$K(z) = \frac{S_{ph}}{v + v_{dr}}, \tag{5.18}$$

$$\lambda(z) = \frac{v_{dr}}{v + v_{dr}} \left(\alpha_{eff} + \frac{\partial_z \mu}{\mu} \right). \tag{5.19}$$

with the charge drift velocity $v_{dr} = \mu E$. Note that we have neglected electron diffusion. Equation (5.17) has the following solution

$$n_e(z) = \int_z^\infty K(y) \, e^{\int_z^y \lambda(x) \, dx} \, dy, \tag{5.20}$$

$$\text{for } z > z_{\text{tip}}.$$

Space-charge effects are small in the avalanche zone, we therefore use equation (5.20) to also determine n_i, i.e. $n_i \approx n_e$ in this region.

5.3.3 The charge layer $(z \approx z_{\text{tip}})$

In all other parts of this section we model the outer scale where the charge layer is considered to be infinitely thin. As a result there is a jump in n_e, n_i and E at z_{tip}. In this section we consider the inner scale and resolve the dynamics in the charge layer in order to determine consistent jump conditions.

The charge layer has a width ℓ that is much smaller than the radius of curvature, $\ell/R \ll 1$, and can therefore be approximately treated as a planar ionization front at the tip. When resolving this planar front we use

$$z_{\text{ch}} = z_{\text{tip}} - \ell, \tag{5.21}$$

to denote the inner boundary of the charge layer. A formula for the ion density in this region can be obtained by integrating the impact ionization source term over the width of the charge

layer

$$n_i(z) = n_{i,\text{tip}} + \frac{\epsilon_0}{e} \int_{E(z)}^{E_{\max}} \alpha_{\text{eff}}(E)\, dE + \frac{1}{ev} \int_z^{z_{\text{tip}}} \alpha_{\text{eff}}(E(z)) j_{\text{tot}}\, dz,$$

$$\text{for } z_{\text{ch}} < z < z_{\text{tip}}. \tag{5.22}$$

where $j_{\text{tot}} = -e j_{e,\text{tip}}$ is the total current density. As a side note, the dynamics of the charge layer are influenced by the avalanche zone since $j_{e,\text{tip}}$ and $n_{i,\text{tip}}$ follow from equation (5.20).

Furthermore, equation (5.22) depends on the electric field profile $E(z)$ which, in the charge layer, is given by a heuristic parameterization of the charge distribution

$$E(z) = E_{\max} - \frac{e}{\epsilon_0} \int_z^{z_{\text{tip}}} \tilde{n}_q(z)\, dz, \tag{5.23}$$

$$\tilde{n}_q = \frac{N_q}{\sigma_\ell \sqrt{2\pi}} \exp\left(-\left(\frac{z-R}{\sigma_\ell}\right)^2\right), \tag{5.24}$$

$$N_q = \frac{\epsilon_0}{e}(E_{\max} - E_{\text{ch}}), \tag{5.25}$$

$$\sigma_\ell = \frac{\ell}{6}. \tag{5.26}$$

Note that $\tilde{n}_q$ is only used to parameterize the electric field in the charge layer.

Additionally, in section 4.3.3 it was shown that by conservation of charge we can calculate n_e as

$$n_e(z) = \frac{v n_i(z) - j_{e,\text{ch}}}{v + v_{\text{dr}}},$$

$$\text{for } z_{\text{ch}} < z < z_{\text{tip}}. \tag{5.27}$$

which in turn determines j_e in the charge layer. We now have a description of the dynamics of the charge layer at the tip. This is used to define the jump conditions for n_e and n_i whenever the charge layer is treated as infinitely thin. For example, the ionization density $n_{i,\text{ch}} = n_i(z_{\text{ch}})$ is obtained by solving equation (5.22), which is then substituted for the value $n_i(z_{\text{tip}}^-)$ when modelling other regions.

In a similar manner we can formulate expressions for the production by electron impact of a specific species in the front, i.e. produced by k_1 to k_5

$$n_{j,\text{ch}} = n_{j,\text{tip}} + \frac{1}{v} \sum_{i \in \mathcal{I}_j} \int_{z_{\text{ch}}}^{z_{\text{tip}}} k_i(E) n_e n_M \, dz,$$

$$j \in \{\text{N}_2^+, \text{O}_2^+, \text{O}_2^-, \text{O}^-, \text{O}\}, \tag{5.28}$$

where $\mathcal{I}_j$ is the set of all reactions producing n_j and n_M is the density of neutrals participating in the reaction, see table 5.1. Note that three-body collisions are an exception, i.e. for the production of O_2^- by k_4 we need to replace n_M by n_M^2. This is not written out for the sake of simplicity, but is accounted for in our calculations. Equation (5.28) can be readily evaluated since E and n_e are determined by equations (5.23) and (5.27).

5.3.4   The channel ($z < z_{\text{tip}}$)

The conductive interior of a streamer is surrounded by a thin layer of charge. The distribution of these charges determines the axial electric field, which couples the dynamics of the channel to the aforementioned regions. In this section we formulate an axial model for the charge distribution in the channel and explain how to calculate the axial electric field.

Charge transport in the channel can be investigated in a width-integrated sense where only the longitudinal currents have to be taken into account [129]. All space charge is accumulated in the charge layer surrounding the channel. We consider the charge layer to be infinitely thin, i.e. $\ell \to 0$, such that we can model it as a charged surface. The net surface charge per unit length is given by $\Sigma(z)$ which satisfies a width-integrated transport equation

$$\partial_t (A\Sigma)(z) = -\partial_z I(z), \tag{5.29}$$

where $I(z)$ is the current (strictly in the z-direction) integrated across the cross section of the streamer and the function $A(z)$ accounts for the area per unit length of the axisymmetric charged surface at z

$$A(z) = 2\pi \mathcal{R}(z) \sqrt{1 + \partial_z \mathcal{R}(z)^2}. \tag{5.30}$$

 We shall briefly investigate the properties of $A(z)$. In figure 5.2 we show the dimensionless result when evaluating equation (5.30) with $R_\infty = 1$. We observe that A approaches a non-zero value at the tip. Working out the limit as $z \to z_{\text{tip}}$ yields $4R_\infty$. One can show, using equation (5.11), that this corresponds to a sphere with radius R. Moreover, the limit for $z \to -\infty$ goes to $2\pi R_\infty$, which corresponds to a cylinder with radius R_∞.
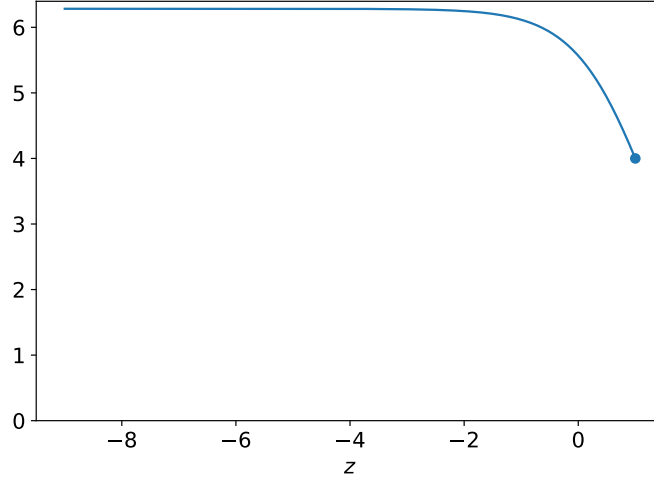
Fig. 5.2 Dimensionless evaluation of A, see equation (5.30), using $R_\infty = 1$ and $z_{\text{tip}} = 1$. The limit for $z \to z_{\text{tip}}$ is also denoted with a bullet.

Now we continue our derivation of the steady-state transport equation. To simplify the notation, we will drop the dependency on z in the notation. Steady streamers, which propagate with a constant velocity v, are at rest in a co-moving reference frame and equation (5.29) can be further simplified

$$\partial_z(vA\Sigma - I) = 0, \tag{5.31}$$

which gives

$$vA\Sigma - I = 0. \tag{5.32}$$

In other words: for steady streamers the current due to translation of the charged surface is equal to the cross section integrated electron current. Note that there is no integration constant in equation (5.32) since both I and Σ vanish far behind the front [131].

In order to solve equation (5.32) we shall give an expression for the current I. Similarly as in [129] we decompose I into two terms

$$I = I_C + I_S, \tag{5.33}$$

with I_C the channel current that flows through the conductive channel and I_S the surface current that flows through the charge layer which we model as a surface on the outer scale. We shall treat these individually in the next sections.

Channel current:

The current in the bulk of the channel, so excluding the current in the charge layer, is given by:

$$I_C(z) = \int_0^{\mathcal{R}(z)} 2\pi r \cdot j_z(z, r)\, dr, \tag{5.34}$$

where $j_z = \sigma E_z$ is the z-component of $\mathbf{j_e}$ and $\sigma = e\mu n_e$ is the conductivity of the plasma channel. Here we consider the simple case where σ is homogeneous in the r-direction, which means it can be considered as a function of z

$$I_C(z) = \sigma(z) \int_0^{\mathcal{R}(z)} 2\pi r \cdot E_z(z, r)\, dr. \tag{5.35}$$

In later sections we will explain how σ is determined by E_z and the primary production of reactive species, equation (5.28).

Now we work out the dependency of I_C on Σ. To that end we first decompose the electric field as

$$E_z = E_{bg} + E_{z,\Sigma} \tag{5.36}$$

where $E_{z,\Sigma}$ is the z-component of the electric field only due to the surface charge Σ. Similarly we decompose

$$I_C = I_{C,bg} + I_{C,\Sigma}. \tag{5.37}$$

The current due to the background field has a simple expression

$$I_{C,bg}(z) = \pi\mathcal{R}(z)^2\sigma(z)E_{bg}. \tag{5.38}$$

However, working out $I_{C,\Sigma}$ is more challenging. Similarly to [129] our approach is to write out $I_{C,\Sigma}$ in terms of a Green's function G_C that represents the contribution to the width-integrated current at z due to a charged ring located at z'

$$I_{C,\Sigma}(z) = \frac{\sigma(z)}{4\pi\epsilon_0} \int_{-\infty}^{z_{\text{tip}}} G_C(z, z')A(z')\Sigma(z')\, dz'. \tag{5.39}$$

The definition of $G_C(z, z')$ is the exact same as used in [129]

$$G_C(z, z') = (z - z') \int_0^{2\pi} \left. \frac{x(r - x) - \rho^2}{\rho^2\sqrt{\rho^2 + (r - x)^2}} \right|_{r=0}^{r=\mathcal{R}(z)} d\varphi', \tag{5.40}$$
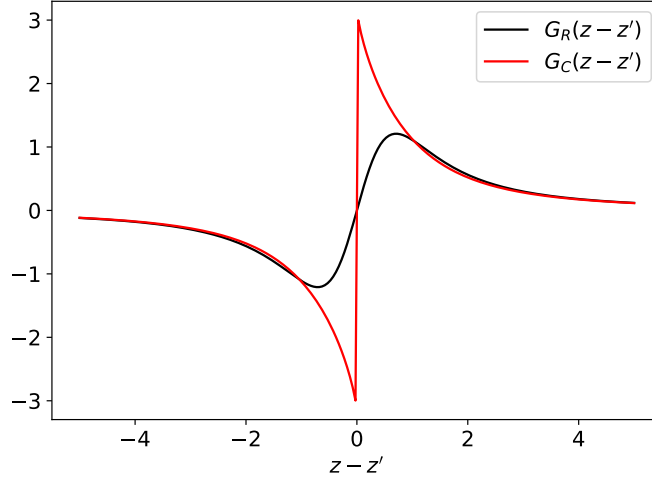
Fig. 5.3 The Green's functions G_C and G_R, defined by equations (5.40) and (5.48), plotted for the case $\mathcal{R} = 1$.

where φ' is the azimuth and, x and ρ are shorthand notation for

$$x(z', \varphi') = \mathcal{R}(z') \cos \varphi' \qquad (5.41)$$

$$\rho(z, z', \varphi') = \sqrt{\mathcal{R}(z')^2 + (z - z')^2}. \qquad (5.42)$$

A graphic representation, using $\mathcal{R}(z) = 1$, is shown in figure 5.3.

One difference of our approach compared to [129] is that they formulated equations (5.29), (5.39) *etc.* in terms of a line charge whereas we use a surface charge. We found that there is a practical advantage to a numerical discretization in terms of the surface charge. We elaborate on this in section 5.4.1 where we discuss the implementation. For now we only remark that this results in the inclusion of the function A in the respective equations.

Surface current:

There is a current flowing through the charge layer at the head which we call the surface current I_S. In this section we derive a width-integrated formulation of I_S. For the definition of I_S we deviate from the formulation of [129], since there are new descriptions of the dynamics of charge layers.

At z_{tip} the channel currents vanish, since $\mathcal{R}(z_{\text{tip}}) = 0$, and the movement of the charge layer is determined by the surface current

$$v A(z_{\text{tip}}) \Sigma(z_{\text{tip}}) = I_S(z_{\text{tip}}). \qquad (5.43)$$

In section 4.3.3 a similar expression was derived that relates the movement of a planar ionization front with an associated surface charge σ_0 to the currents flowing through it

$$v\sigma_0 = \int_{z_{\text{ch}}}^{z_{\text{tip}}} e(j_{e,\text{tip}} - j_e)\, dz. \tag{5.44}$$

In section 5.3.3 we analysed the inner solution of the charge layer at the tip and explained how the right-hand side can be evaluated. In order to be consistent with the underlying physics of moving ionization fronts we use this to express the surface current at the tip

$$I_S(z_{\text{tip}}) = A(z_{\text{tip}}) \int_{z_{\text{ch}}}^{z_{\text{tip}}} e(j_{e,\text{tip}} - j_e)\, dz, \tag{5.45}$$

where the function A accounts for the surface area since we work within a width-integrated approach here. Essentially this couples the dynamics of the inner- and outer solutions.

Equation (5.45) describes the surface current only at the tip. However, the active region of the charge layer surrounds the whole of the streamer head and is diminishing towards the side. The off-axis dynamics of the active charge layer are difficult to express within our axial model, for that reason we impose a prescribed z-dependency, giving

$$I_S(z) = A(z) \exp\left(\frac{z - z_{\text{tip}}}{R}\right) \int_{z_{\text{ch}}}^{z_{\text{tip}}} e(j_{e,\text{tip}} - j_e)\, dz. \tag{5.46}$$

This decay accounts for the fact that the ionization front is most intense at the tip and diminishes towards the sides of the head. Our imposed z-dependency of I_S currently lacks physical motivation. Instead we chose the simplest z-dependency. Future research should address this subject in more detail.

Calculation of the internal electric field:

In this section we explain how the axial electric field $E_z(z)$ can be calculated for given $\Sigma(z)$. Due to symmetry we can calculate $E_z(z)$ by integrating over a series of charged rings. The shape function $\mathcal{R}(z)$ defines the radius of each ring and $\Sigma(z)$ determines their charge

$$E_z(z) = \frac{1}{4\pi\epsilon_0} \int_{-\infty}^{z_{\text{tip}}} G_R(z, z') A(z') \Sigma(z')\, dz', \tag{5.47}$$

where G_R is a Green's function that accounts for contribution of a uniformly charged ring at z' to the electric field at z [129]. Due to symmetry E_z is always oriented in the z-direction

on the z-axis, so we will drop the subscript from now on. Similarly to G_C, G_R is multiplied with the function A in equation (5.47) so that we can work with the same definition as [129], namely

$$G_R(z, z') = \frac{(z - z')}{[\mathcal{R}(z')^2 + (z - z')^2]^{3/2}}.$$
(5.48)

Figure 5.3 shows a graphic representation of G_R using $\mathcal{R} = 1$.

Note that the above equation is also used to extract the macroscopic parameters related to the electric field at either side of z_{tip}: E_{max} and E_{ch}. For this we use $E_{\text{max}} = E(z_{\text{tip}} + \delta)$, where $\delta = 10^{-7}$ is a small parameter that prevents evaluation of the electric field at the discontinuity at z_{tip}. This parameter has no physical meaning and decreasing it by a factor 10 has a negligible influence on E_{max}. For the channel electric field we take the value computed at the first cell face behind the tip: $E_{\text{ch}} = E(z_{\text{tip}} - \Delta z_{\text{tip}})$ where Δz_{tip} is the size of the cell at the tip.

Calculation of the channel conductivity:

In previous sections we formulated Σ, and therefore E, in terms of a given conductivity σ. Now we complement this by formulating σ in terms of a given E and the primary excitation of reactive species in the front. The full solution of this implicit problem is left until section 5.4.3.

In a co-moving frame the evolution of species follow from the coupled reaction equations

$$\begin{cases} v\partial_z n_e = -S, \\ v\partial_z n_j = -S_j. \end{cases}$$
(5.49)

Note that electron currents do not have to be included here. Since the channel is quasi-neutral and ions are immobile, we locally must have $\nabla \cdot \mathbf{j_e} = 0$. We will further consider the validity of this argument in future research.

The densities of reactive species are coupled to the other regions by equation (5.28), which determines the boundary conditions $n_{j,\text{ch}}$ and $n_{e,\text{ch}} = \sum_j q_j n_{j,\text{ch}}$ at z_{tip} inside the channel, where q_j is the signed charge of n_j. Equation (5.49) can be solved by numerical integration, from which we obtain $\sigma(z)$ for a given E.

5.3.5 Steady streamer propagation

In the previous sections we have derived the model equations for electron, ion and surface charge densities as a function of the steady streamer properties velocity v, radius R, the

species-resolved ionization density $\bar{n}_{j,\text{ch}}$ and charge layer width ℓ. Here we will explain how these parameters are calculated self-consistently.

In Chapter 4 we have formulated a system of equations that can be used to calculate 4 macroscopic parameters. We follow the same approach with two crucial differences: (i) we use the resolved axial electric field $E(z)$ instead of a parametrized interior electric field with a given conductivity loss length L_{loss}, and (ii) we calculate v, R, ℓ and $\bar{n}_{j,\text{ch}}$ as a function of the applied background field

$$E_{\text{bg}} \rightarrow v,\ R,\ \ell \text{ and } \bar{n}_{j,\text{ch}}. \tag{5.50}$$

This calculation is implicitly coupled to Σ, E and σ. In earlier sections we have derived equations (5.32), (5.47) and (5.49) from which Σ, E and σ follow, respectively. For completeness we will append these to our system of equations.

Our system of equations is thus composed of the following:

1. from conservation of total current density we get

$$j_{e,\text{ch}} = j_{e,\text{tip}}, \tag{5.51}$$

2. from conservation of charge in the ionization front we get

$$v\epsilon_0(E_{\text{max}} - E_{\text{ch}}) = \int_{z_{\text{ch}}}^{z_{\text{tip}}} e(j_{e,\text{tip}} - j_e)\,dz. \tag{5.52}$$

3. since the electric field is a gradient we have

$$R_\infty(E_{\text{max}} - E_{\text{bg}}) = \int_{-\infty}^{z_{\text{tip}}} (E_{\text{bg}} - E(z))\,dz. \tag{5.53}$$

4. consistent electron dynamics in the avalanche zone and the charge layer requires

$$\frac{n_{e,\text{tip}}}{n_{i,\text{ch}}} = F(v, R, E_{\text{max}}, E_{\text{bg}}), \tag{5.54}$$

   where the reader is referred to equation (4.45) for the definition of F. Additionally, each species-resolved ionization density has to follow

$$n_{j,\text{ch}} = n_{j,\text{tip}} + \frac{1}{v}\sum_{i\in\mathcal{I}_j}\int_{z_{\text{ch}}}^{z_{\text{tip}}} k_i(E)n_e n_M\,dz, \tag{5.55}$$

5. the surface charge Σ follows a steady state charge distribution

$$vA\Sigma - I = 0, \tag{5.56}$$

6. the axial electric field follows from the surface charge

$$E(z) = \frac{1}{4\pi\epsilon_0} \int_{-\infty}^{z_{\text{tip}}} G_R(z, z')A(z')\Sigma(z')\,dz'. \tag{5.57}$$

This also determines E_{max} and E_{ch}.

7. the conductivity follows from solving the chemical reaction mechanism

$$\begin{cases} v\partial_z n_e = -S, \\ v\partial_z n_j = -S_j, \end{cases} \tag{5.58}$$

which uses $\bar{n}_{j,\text{ch}}$ as a boundary condition at z_{tip} inside the channel.

By adopting an iterative solution method the system of equations (5.51)-(5.58) will be solved which self-consistently determines steady streamer parameters as a function of E_{bg}. This requires a particular order in which the calculations have to be performed. We postpone this until section 5.4.3, after discussing implementation details.

5.4   Implementation

5.4.1   Solving for the surface charge

In this section we discretize equation (5.32) and write it as a linear system which is used to solve Σ for given macroscopic parameters. We write equation (5.32) as

$$vA\Sigma - I_{C,\Sigma} - I_S = I_{C,\text{bg}}. \tag{5.59}$$

Next we introduce the discretizion. The z-axis is divided into cells $C^1, C^2, \ldots, C^N$ with the cell-faces of C^i defined at $(z^{i-1/2}, z^{i+1/2})$. Correspondingly, the surface charge is discretized as

$$\bar{\Sigma} = [\Sigma^1, \Sigma^2, \ldots, \Sigma^i, \ldots, \Sigma^{N-1}, \Sigma^N]^T, \tag{5.60}$$

such that $\Sigma^i = \Sigma(z^i)$ is constant within each cell. In discretized form, we can represent the current at the jth cell face as a matrix-vector product. For instance

$$\bar{I}_{C,\Sigma} = \mathbf{M_C}\bar{\Sigma}, \tag{5.61}$$

where $\mathbf{M_C}$ is an $N \times N$ matrix with entries

$$M_C^{ij} = \frac{\sigma^j}{4\pi\epsilon_0} \int_{z^{i-1/2}}^{z^{i+1/2}} G_C(z^j, z')A(z') \, dz', \tag{5.62}$$

These cell-wise integrands are numerically integrated by the double-exponential quadrature rule [169], which proved to be robust and computationally efficient in the presence of the singularities of G_C.

We address the surface current, defined in equation (5.46), in a similar manner. However, we first use equation (5.52) to write I_S in terms of $E_{\max}$, neglecting E_{ch} since it is much smaller. Then we use equation (5.57) evaluated at z_{tip} such that we can also write I_S as a matrix-vector product

$$\bar{I}_S = \mathbf{M_S}\bar{\Sigma}, \tag{5.63}$$

$$M_S^{ij} = \frac{B^j}{4\pi} \int_{z^{i-1/2}}^{z^{i+1/2}} G_R(z^{N+1/2}, z')A(z') \, dz', \tag{5.64}$$

$$B^j = vA^j \exp\left(\frac{z^j - z^{N+1/2}}{R}\right). \tag{5.65}$$

Using these matrix representations of the currents we can write equation (5.59) as a linear system

$$(vA\mathbf{1} - \mathbf{M_C} - \mathbf{M_S})\bar{\Sigma} = \bar{I}_{\text{bg}}, \tag{5.66}$$

with $\mathbf{1}$ the identity matrix. Or simply

$$\mathbf{M}\bar{\Sigma} = \bar{I}_{\text{bg}}. \tag{5.67}$$

Note that $\mathbf{M}$ and $\bar{I}_{\text{bg}}$ can be explicitly evaluated for given v, R and σ. Thus we can solve this linear system to obtain $\bar{\Sigma}$. An important consequence of this is that this solution also gives us the axial electric field. Specifically, we can write equation (5.47) in discretized form

$$\bar{E} = \mathbf{M_E}\bar{\Sigma}, \tag{5.68}$$

where $\mathbf{M_E}$ is defined by

$$M_E^{ij} = \frac{1}{4\pi\epsilon_0} \int_{z^{i-1/2}}^{z^{i+1/2}} G_R(z^j, z')A(z')\,dz'. \tag{5.69}$$

As a final note, we remark why it is advantageous to work in terms of a surface charge, instead of a line charge as was done in [129]. A desired property of the discretization is that the surface charge is constant within each cell, see equation (5.60). However, if we would instead work with a line charge that is constant in each cell then the surface charge is varying in each cell. These sub-cell variations are determined by the fixed shape function $\mathcal{R}(z)$, which means we have no control over them. We found that this can lead to poor convergence properties when the cell size is reduced, especially near z_{tip}. To avoid this issue we explicitly work in terms of a surface charge which in discretized form is held constant within each cell.

5.4.2 Chemistry in the avalanche zone

We do not resolve secondary reactions in the avalanche zone. This is justified since ionization and secondary reactions occurring there do not contribute much to the initial ion densities $\bar{n}_{j,\text{ch}}$. Instead we will approximate $n_{j,\text{tip}}$ such that it is consistent with the treatment of the avalanche zone, i.e. $n_{i,\text{tip}} = \sum_j q_j n_{j,\text{tip}}$.

In equation (5.54) we have defined a criteria for consistent electron dynamics in the avalanche zone and the charge layer. Now we assume that this also holds individually for each of the species produced by electron impact, cf. reactions k_1 to k_5 in table 5.1. This allows us to approximate $n_{j,\text{tip}}$ in terms of $n_{j,\text{ch}}$

$$n_{j,\text{tip}} = F\,n_{j,\text{ch}}. \tag{5.70}$$

This is then used to evaluate equation (5.55).

5.4.3 Obtaining a self-consistent solution

In the previous section we have described how Σ and E can be calculated as functions of steady streamer parameters v, R, ℓ and $\bar{n}_{j,\text{ch}}$. However, the main challenge is to obtain these parameters self-consistently. To that end we shall illustrate that an iterative solution method can find parameters that are simultaneously consistent with the equations summarized in section 5.3.5.

Our approach consists of two nested iterative solvers. The outer solver approximates the parameters:

$$m = [v, \ R, \ \ell, \ \bar{n}_{j,\text{ch}}], \qquad\qquad (5.71)$$

and the inner solver approximates a solution for the implicitly-coupled grid-vectors $\bar{\Sigma}$, $\bar{E}$ and $\bar{\sigma}$ for a given m.

The inner solver consists of the following steps:

1. *Solving the conductivity:* We use an approximation m' which is the current guess of the outer solver. Then we make an initial guess for the electric field $\bar{E}'$. These guesses combined are sufficient to solve the reaction equations (5.58) and obtain a conductivity $\bar{\sigma}'$ in the channel.

2. *Solving for the electric field:* With m' and $\bar{\sigma}'$ we can solve equation (5.67) to find $\bar{\Sigma}'$. Then by equation (5.68) we calculate $\bar{E}$.

3. *Evaluation and update:* now we evaluate the difference between the guessed $\bar{E}'$ and the calculated $\bar{E}$. We employ a Newton-Krylov iterative solver that updates $\bar{E}'$ with the goal to minimize the norm of this difference. This gives the self-consistent quantities $\bar{\Sigma}$, $\bar{E}$ and $\bar{\sigma}$ for a given m'.

The outer solver complements the above procedure with the following steps:

1. *Solving the avalanche zone:* We start from a guessed solution m' and employ the inner solver to obtain $\bar{E}$, which notably calculates E_{max} and E_{ch}. Then we use $n'_{i,\text{ch}}$ to calculate the photoionization source in equation (5.18) and solve the electron density in the avalanche zone from equation (5.20). In particular this defines the electron density at the tip $n_{e,\text{tip}}$.

2. *Solving front ionization:* Using the calculated $n_{e,\text{tip}}$ we can calculate $j_{e,\text{tip}}$ and subsequently $n_{i,\text{ch}}$ from equation (5.22). This also gives the species-resolved ionization density $\bar{n}_{j,\text{ch}}$ by equation (5.55).

3. *Evaluation and update:* Now we can evaluate the consistency of m'. Using the calculated parameters we evaluate whether equations (5.51)-(5.55) are satisfied. We employ an optimization algorithm based on a modification of the Levenberg-Marquadt algorithm [149] that provides a new m' with the goal of minimizing the residuals from the equations (5.51)-(5.55).

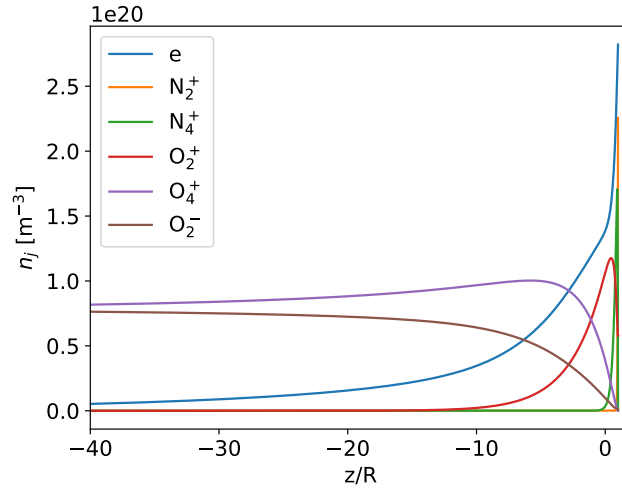The two nested iterative solvers produce a sequence of approximations that converge to a self-consistent solution m.

Fig. 5.4 The evolution of reactive species at $E_{\text{bg}} = 4.5 \text{ kV cm}^{-1}$

5.5   Results

First we analyze the channel dynamics of a steady streamer at 4.5 kV cm^{-1}. Afterwards we investigate how the properties of steady streamers depend on E_{bg} and compare them to earlier observations.

5.5.1   Dynamics in the channel

We analyze the results of a steady streamer in a background field of 4.5 kV cm^{-1}. The macroscopic parameters corresponding to this self-consistent solution are $v = 5.43 \cdot 10^4 \text{ m s}^{-1}$, $R = 4.81 \cdot 10^{-5} \text{ m}$, $\ell = 4.84 \cdot 10^{-6} \text{ m}$ and $n_{i,ch} = 2.90 \cdot 10^{20} \text{ m}^{-3}$.

In figure 5.4 we show the evolution of reactive species. The initial densities at z_{tip} of electrons, N_2^+, O_2^+ and other negative ions are primarily created by ionization in the charge layer. Then a sequence of chemical processes leads to the loss of conductivity: (i) N_2^+ is rapidly converted to N_4^+ which either reacts to form O_2^+ or already neutralizes due to electron-ion recombination. This leads to a fast initial reduction of n_e, (ii) a slightly slower process is the conversion of O_2^+ to O_4^+ which also leads to recombination. (iii) Further into the channel three-body attachment to O_2, forming O_2^-, becomes an important sink of electrons.

In figure 5.5 we show the width integrated currents. The bulk currents $I_{C,\text{bg}}$ and $I_{C,\Sigma}$ are about a factor 10 larger than I_S, but they partially cancel which means that their combined effect is comparable to the other terms. At the back of the streamer there is almost no surface current and therefore the translational movement of the charges, represented by $vA\Sigma$, is equal to the
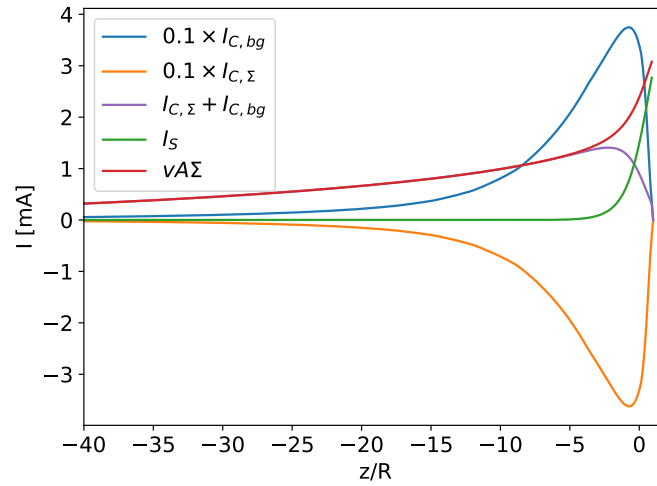
Fig. 5.5 The width integrated currents at $E_{bg} = 4.5\ \text{kV cm}^{-1}$. $I_{C,\Sigma}$ and $I_{C,bg}$ have been scaled to fit the graph.
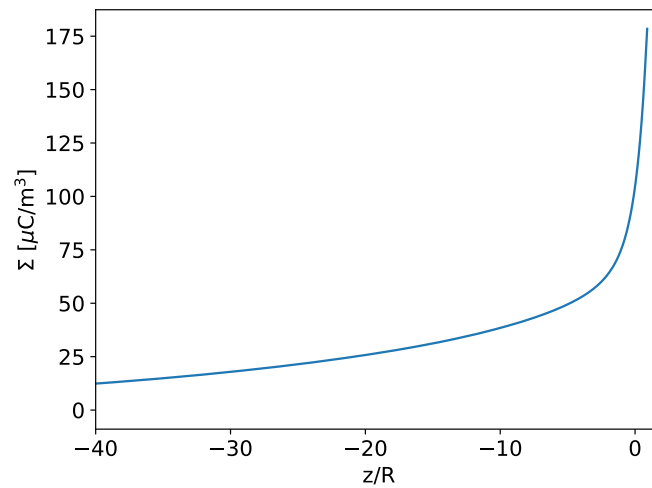

Fig. 5.6 The surface charge per unit length at $E_{bg} = 4.5\ \text{kV cm}^{-1}$.
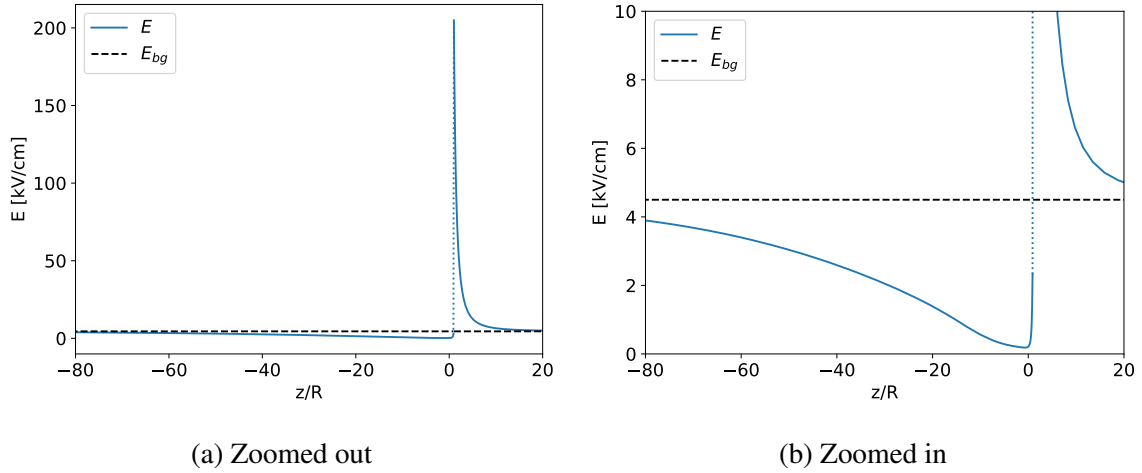
(a) Zoomed out   (b) Zoomed in

Fig. 5.7 E of a steady streamer at $E_{\mathrm{bg}} = 4.5 \, \mathrm{kV \, cm^{-1}}$.

sum of the bulk currents. Moreover, due to the decaying conductivity the currents vanish far back into the channel. On the contrary, close to the head we approach the active region of the charge layer where I_S starts to play an important role. In particular close to the tip where the bulk currents vanish since $\mathcal{R}(z_{\mathrm{tip}}) = 0$, but where I_S approaches its maximum value.

In figure 5.6 we show the surface charge (per unit length) Σ. We find that the head is intensely charged, which is primarily a result of I_S. Further back into the channel Σ is decaying as a result of the loss of conductivity. Next, Σ produces an electric field that is shown in figure 5.7. The intensely charged head causes high electric field enhancement and screening of the interior electric field. Far back into the channel, where Σ is decaying, we observe that E returns to the background electric field.

One striking feature of this solution is that E_{ch} is not the minimum electric field inside the streamer channel. Instead the minimum is found at $z/R = -0.72$, which is well into the channel, and a value of $0.185 \, \mathrm{kV \, cm^{-1}}$. In comparison, this is only about 8% of E_{ch} which equals $2.33 \, \mathrm{kV \, cm^{-1}}$. Similar behaviour is also observed in direct numerical simulations of steady streamers (not shown here) although this is often not remarked if y-axis is zoomed out to also incorporate E_{max}. We therefore conclude that such non-monotonic electric field profiles in the streamer head are physical, at least for steady streamers.

5.5.2   Dependence on E_{bg}

In figure 5.8 we show the properties v, R, E_{max} and $n_{i,\mathrm{ch}}$ of steady streamers as a function of E_{bg}. Each of the data points in that figure represents a self-consistent solution where only the (constant) values of E_{bg} has been varied in the range 4.0 - 5.0 $\mathrm{kV \, cm^{-1}}$. Moreover
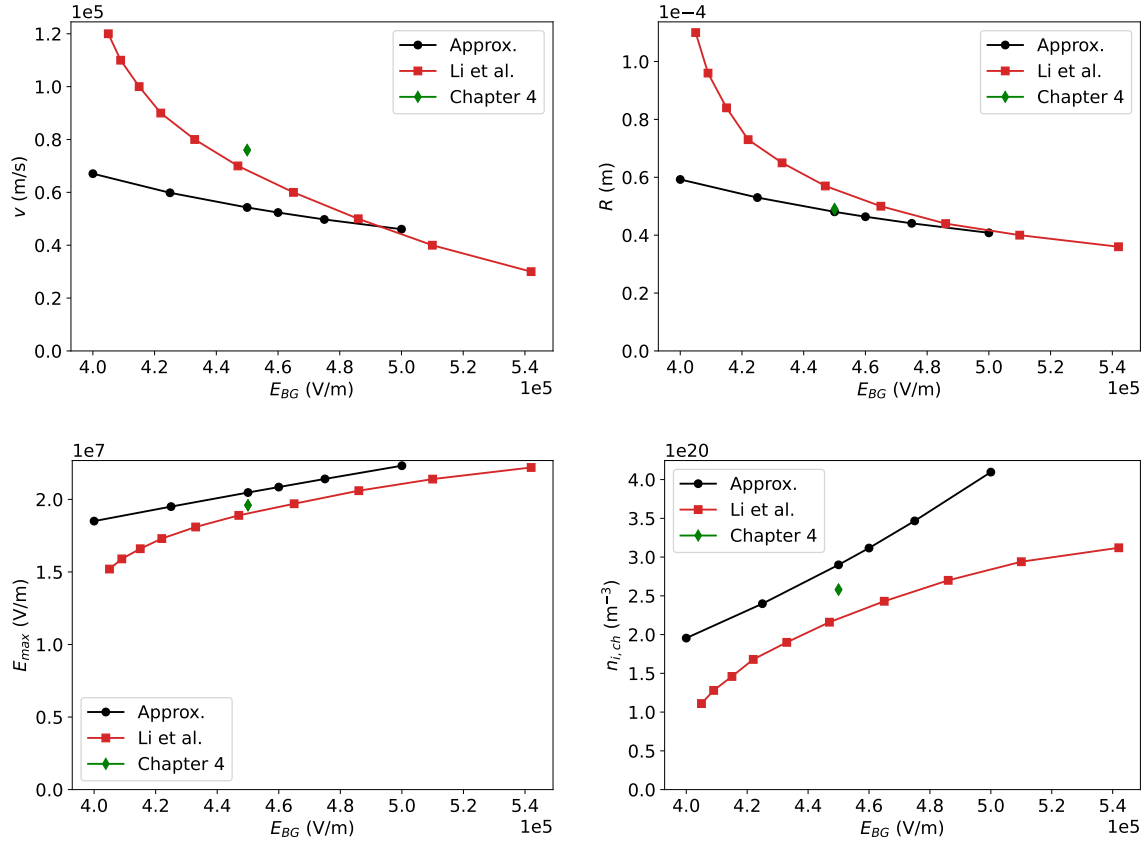
Fig. 5.8 The macroscopic parameters v, R, $E_{\max}$ and $n_{i,\mathrm{ch}}$ of steady streamers as a function of E_{bg}. Each bullet represents a single steady streamer. We compare our results with numerical simulations (Li *et al.* [131] and Chapter 4), the differences between these simulations are explained in the text. Notably, Li *et al.* uses a different definition of the radius.

in figure 5.8 we also include results from two series of direct numerical simulation: Li *et al.* [131] and Chapter 4. The simulations in Li *et al.* account for ion motion and contain a regularization factor that suppresses impact ionization due the component of the diffusion current that is parallel to the electric field. Both of these are not included in our axial model. Moreover, Li *et al.* also work with a different definition of the radius, namely: "the radial coordinate at which the radial electric field has a maximum". These differences prevent us from making a one-to-one comparison between our results and this data, however a certain level of agreement could be expected. On the other hand the simulation of Chapter 4 is consistent with our terminology and the basic equations explained in section 5.2, but it only contains data of one steady streamer at 4.5 kV cm^{-1}.

Overall, our results agree with the general trend of steady streamer properties as a function of E_{bg} as reported in Li *et al.* [131]. We observe that:

- E_{max} and $n_{i,\text{ch}}$ increase with increasing E_{bg}, and

- v and R decrease with increasing E_{bg}.

Thus, in higher E_{bg} we have slower and thinner steady streamers with a higher degree of ionization.

We also observe some differences when we compare our approximations with the results from Li *et al.* [131], especially for the faster steady streamers in low E_{bg}. When compared to simulations from Chapter 4 at 4.5 kV cm^{-1} we find a better agreement, except for v. This suggest that the different model used in Li *et al.* [131] explains only a part of the discrepancy with our results.

5.6 Summary and outlook

5.6.1 Summary

The main contribution of this work is the derivation of an axial model for positive steady streamers. Our model solves or projects all relevant parameters on the central axis, which is a highly attractive property from a computational point of view. Our solutions are characterized by the macroscopic parameters velocity, radius, charge layer width and ionization densities, which are resolved by the model itself. This distinguishes our approach from previous so-called 1.5D models where the radius had to be externally supplied. Our model was derived by combining existing approaches which dealt with the sub-problems of the channel dynamics [129] and the approximation of macroscopic parameters Chapter 4 and by imposing steady propagation. We found reasonable agreement when our approximations were compared to the properties of steady streamers obtained by numerical simulation. The comparison might be improved further after a reconsideration of some approximations and assumptions made and discussed in the present version of the calculation.

5.6.2 Outlook

For future work it is important to reconsider the calculation of E_{max} and E_{ch}. The current approach is to use equation (5.47) evaluated at z_{tip}. The issue is that at z_{tip} we are in or around the charge layer and the approximation of the charge layer as an infinitely thin surface looses its validity (cf. figure 5.1). Note that this is not as big an issue further into the channel where the distance from the central axis to the charge layer is always much greater than ℓ (since generally $R \gg \ell$). A similar issue arises with the approximated electric field in the avalanche

zone, equation (5.16), which also looses its validity when the distance between z and z_{tip} becomes comparable with ℓ.

Our scope was restricted to positive steady streamers in air, since it is a mathematically convenient test case. It would be interesting to derive more sophisticated axial models for applications involving large streamer coronae or repetitively pulsed streamer discharges. Such applications involve accelerating or even stagnating streamers. In Chapter 4 we have already shown that our approach to calculating macroscopic parameters can also be considered for accelerating streamers, however the validity of this model regarding stagnating streamers has yet to be investigated. Further research should also investigate whether a similar approach can be formulated for negative streamers.

Finally we comment on the significance of our work regarding the development of accurate streamer tree models. The current limitation of these models is that they lack a self-consistent description of macroscopic parameters such as velocity, radius, internal conductance and subsequent chemical activation. In this work we show explicitly how such limitations can be overcome.

Chapter 6

Summary and outlook

6.1 Summary

We started this thesis by showing that the physics of streamer discharges span widely varying spatial and temporal scales and we reviewed the hierarchy of models that is used to investigate these phenomena (cf. section 1.2). The reader that made it up to here can conclude that we traversed the whole of this hierarchy. We started from the microscopic scale as we reviewed electron scattering cross sections with methane (Chapter 2). They were used to investigate the mesoscopic scale where we simulated streamers in stoichiometric air-methane using a particle model for the electrons (Chapter 3). Finally we extended the scope towards the macroscopic scale as we described streamers solely on the basis of a set of macroscopic parameters such as velocity, radius, length *etc.* We showed how these macroscopic parameters are non-linearly coupled with each other and how they determine electron dynamics (Chapter 4). Moreover we succeeded in formulating an axial model for steady streamers. This model gives a complete macroscopic description of steady streamers as a function of the applied electric field (Chapter 5).

Now we present a more detailed summary of the main conclusions per chapter:

- **Chapter 2:** We have collected cross section data for electron scattering with the ground state of methane. The available data was inconsistent regarding neutral dissociation, which is an important process that can not be omitted. We then proposed cross sections for this process by relying on a blend of empirical and analytical cross sections. The resulting cross section set was implicitly validated by a performing a Boltzmann analysis. The presented set distinguishes itself by not relying on data-fitting techniques

to ensure consistency. This feature is especially attractive for particle-in-cell models or applications that focus on plasma-chemical activation of the gas (cf. Chapter 3). Our suggested cross sections are available on LXCat [170].

- **Chapter 3:** We have performed three-dimensional particle-in-cell simulations of positive streamers in air and in a stoichiometric air-methane mixture. This is relevant for plasma-assisted combustion. For this, we used the cross sections from Chapter 2 and extended the photoionization model for air to account for methane. It follows that methane significantly suppresses photoionization while the transport and reaction coefficients stay essentially unchanged. This has the effect that positive streamers branch more often than their counterparts in air. Similar behaviour can be expected in other gasses with weak photoionization. Additionally we have characterized the plasma-chemical activation of air-methane by streamers by calculating the energy density deposition and the radical production.

- **Chapter 4:** We have given a macroscopic representation of positive steady streamers in air using 8 parameters. These parameters are: velocity, radius, length, charge layer width, ionization density and the background-, channel- and maximum electric fields. Using analytical approximations we showed how the electron dynamics are defined by these parameters and how they are coupled to each other. Our approximations are compared with numerical simulations and we found reasonable agreement. We presented our model as an estimation technique that can support experimental studies when direct measurements of certain macroscopic parameters are impossible. Finally our results indicate that this macroscopic representation seems also applicable to accelerating streamers.

- **Chapter 5:** We developed an axial model for positive steady streamers in air. The solutions of the axial model are characterized by macroscopic parameters, but these are calculated by the model itself (opposed to Chapter 4 where some parameters had to be supplied). We can thus calculate the properties of steady streamers in an axial manner solely as a function of the applied electric field. We compared our results with numerical simulations and found reasonable agreement. This indicates that our axial model captures the relevant physics of steady streamers using a simple macroscopic representation. Our approach is a stepping stone for the development of more sophisticated axial streamer models.

6.2   Outlook

This thesis culminated when we derived an axial model for steady positive streamers from the underlying microphysics (Chapter 5). In doing so we formally extended the hierarchy of models for streamers to the macroscopic scale. A clear advantage of such macroscopic models is that they can be simulated much more conveniently. This opens up the possibility of investigations into streamer discharge phenomena that are infeasible to simulate using a fluid model, e.g. large streamer discharge structures that are the result of successive branching. Such streamer trees are crucial to explain and model various types of atmospheric electricity. Streamers trees can even be essential to several poorly-understood lightning phenomena such as: the mechanism of lightning initiation, the asymmetry between the propagation of different types of lightning leaders, explaining various electromagnetic signatures (e.g. narrow bipolar events) and high-energy radiation (e.g. X-ray pulses and terrestrial gamma ray flashes). However observational and experimental research into this subject is hindered by the unpredictable, transient and extreme nature of lightning and the difficulties of measuring in thunderstorms. Numerical simulations are then an attractive alternative scientific approach, provided that accurate and computationally feasible models exist. We identify this as one of the key areas where macroscopic streamer models could have significant impact.

Lastly, we summarize several improvements and other opportunities to continue the research presented in this thesis. We shall restrict ourselves to the macroscopic scale (Chapters 4 and 5):

- **Formal representation of the charge layer:** In section 4.3 we proposed heuristic approximations for the dynamics of the charge layer, but a more rigorous approach could be developed. Ideally such an approach also provides better approximations for E_{max} and E_{ch} (see section 5.6.2) and captures the gradual transition from the curved charge layer to the avalanche zone, instead of the abrupt transition that was considered in this thesis. The same holds for the transition to the channel region.

- **Streamers in different conditions:** Our macroscopic representation of streamers was restricted to positive steady streamers in air. The reason for this is that positive steady streamers are a mathematically convenient test case that includes photoionization. In realistic applications, however, there is a large variety of streamer phenomena and the parameter regime is extensive: streamer heads can be accelerating or stagnating, the gas composition or pressure can change, they can have negative polarity and have widely varying parameters. Our macroscopic model should be extended and validated

to account for these phenomena as well. In this regard, a first effort was already made in Chapter 4 where we compared our model with accelerating positive streamers.

- **Streamer branching and trees:** As mentioned, macroscopic models are particularly interesting for large streamer discharge structures that are the result of successive branching. A simplified approximation of a so-called streamer tree model is given in [10]. The model developed in this thesis accounts for more physics than [10] because it calculates the velocity and radius of streamer heads based on the microphysics, but branching still needs to be prescribed. One approach is to prescribe branching stochastically where parameters, such as branching frequency and angles, are obtained from numerical or experimental observations (cf. [128], in particular figures 5 and 6).

- **Repetitive discharges with chemistry:** Industrial applications of streamers often involve repetitive streamer discharging. For a sufficiently high repetition frequency the chemical effects of the consecutive streamers will accumulate. Investigating repetitive streamer discharges using the fluid model is computationally demanding due to widely varying time scales and it is usually only feasible to simulate a few pulses, even in 2D axisymmetric configurations with simplified chemistry. A macroscopic model could be useful to study such discharges on longer time scales, provided that memory effects, surface interactions, gas heating and other relevant processes can be accounted for on a macroscopic scale.

References

[1] Sander Nijdam, F M J H van de Wetering, R. Blanc, E M van Veldhuizen, and U. Ebert. Probing photo-ionization: experiments on positive streamers in pure gases and mixtures. *Journal of Physics D: Applied Physics*, 43(14):145204, 4 2010.

[2] Steven A. Cummer, Nicolas Jaugey, Jingbo Li, Walter A. Lyons, Thomas E. Nelson, and Elizabeth A. Gerken. Submillisecond imaging of sprite development and structure. *Geophysical Research Letters*, 33(4):L04104, 2 2006.

[3] Piers Forster, Venkatachalam Ramaswamy, Paulo Artaxo, Terje Berntsen, Richard Betts, David W Fahey, James Haywood, Judith Lean, David C Lowe, Gunnar Myhre, et al. Changes in atmospheric constituents and in radiative forcing. *Climate Change 2007: The Physical Science Basis. Contribution of Working Group I to the 4th Assessment Report of the Intergovernmental Panel on Climate Change*, 2007.

[4] Junhong Chen and Jane H Davidson. Ozone production in the positive DC corona discharge: Model and comparison to experiments. *Plasma chemistry and plasma processing*, 22:495–522, 2002.

[5] L. Bárdos and H. Baránková. Cold atmospheric plasma: Sources, processes, and applications. *Thin Solid Films*, 518(23):6705–6713, 2010.

[6] Gregory Fridman, Gary Friedman, Alexander Gutsol, Anatoly B. Shekhter, Victor N. Vasilets, and Alexander Fridman. Applied plasma medicine. *Plasma Processes and Polymers*, 5(6):503–533, 2008.

[7] Rohit Thirumdas, Anjinelyulu Kothakota, Uday Annapure, Kaliramesh Siliveru, Renald Blundell, Ruben Gatt, and Vasilis P. Valdramidis. Plasma activated water (PAW): Chemistry, physico-chemical properties, applications in food and agriculture. *Trends in Food Science & Technology*, 77:21–31, 7 2018.

[8] Andrey Starikovskiy and Nickolay Aleksandrov. Plasma-assisted ignition and combustion. *Progress in Energy and Combustion Science*, 39(1):61–110, 2 2013.

[9] Sander Nijdam, Jannis Teunissen, and Ute Ebert. The physics of streamer discharge phenomena. *Plasma Sources Science and Technology*, 29(10):103001, 11 2020.

[10] Alejandro Luque and Ute Ebert. Growing discharge trees with self-consistent charge transport: the collective dynamics of streamers. *New Journal of Physics*, 16(1):013039, 1 2014.

[11] Michael J Brunger and Stephen J Buckman. Electron–molecule scattering cross-sections. I: Experimental techniques and data for diatomic molecules. *Physics reports*, 357(3-5):215–458, 2002.

[12] Jonathan Tennyson. Electron–molecule collision calculations using the R-matrix method. *Physics Reports*, 491(2-3):29–76, 2010.

[13] M. B. Zhelezniak, A. Kh. Mnatsakanian, S. V. Sizykh, M. B. Zhelezniak, A. Kh. Mnatsakanian, and S. V. Sizykh. Photoionization of nitrogen and oxygen mixtures by radiation from a gas discharge. *HTemS*, 20(3):357–362, 1982.

[14] G. J.M. Hagelaar and L. C. Pitchford. Solving the Boltzmann equation to obtain electron transport coefficients and rate coefficients for fluid models. *Plasma Sources Science and Technology*, 14(4):722–733, 2005.

[15] Tiago C. Dias, Antonio Tejero-del Caz, Luís L. Alves, and Vasco Guerra. The LisbOn KInetics Monte Carlo solver. *Computer Physics Communications*, 282, 1 2023.

[16] J. M. Meek. A Theory of Spark Discharge. *Physical Review*, 57(8):722–728, 4 1940.

[17] C. Montijn and U. Ebert. Diffusion correction to the Raether–Meek criterion for the avalanche-to-streamer transition. *Journal of Physics D: Applied Physics*, 39(14):2979–2992, 7 2006.

[18] Zhen Wang, Anbang Sun, and Jannis Teunissen. A comparison of particle and fluid models for positive streamer discharges in air. *Plasma Sources Science and Technology*, 31(1):015012, 1 2022.

[19] Robert Marskar. 3D fluid modeling of positive streamer discharges in air with stochastic photoionization. *Plasma Sources Science and Technology*, 29(5):055007, 5 2020.

[20] Leonard B Loeb. Ionizing Waves of Potential Gradient. *Science*, 148(3676):1417–1426, 6 1965.

[21] A. M. Cravath and L. B. Loeb. The mechanism of the high velocity of propagation of lightning discharges. *Journal of Applied Physics*, 6(4):125–127, 1935.

[22] H Raether. Die entwicklung der elektronenlawine in den funkenkanal: Nach beobachtungen in der nebelkammer. *Zeitschrift für Physik*, 112(7-8):464–489, 1939.

[23] Leonard Benedict Loeb and John M Meek. *The mechanism of the electric spark*. Stanford University Press, 1941.

[24] MI Dyakonov and VY Kachorovskii. Theory of streamer discharge in semiconductors. *Sov. Phys. JETP*, 67(5):1049–1054, 1988.

[25] MI D'yakonov and VY Kachorovskii. Streamer discharge in a homogeneous field. *Zh. Eksp. Teor. Fiz*, 95(May):1850–1859, 1989.

[26] George V. Naidis. Positive and negative streamers in air: Velocity-diameter relation. *Physical Review E - Statistical, Nonlinear, and Soft Matter Physics*, 79(5):3–6, 2009.

[27] Dennis D. Bouwman, Andy Martinez, Bastiaan J Braams, and U. Ebert. Neutral dissociation of methane by electron impact and a complete and consistent cross section set. *Plasma Sources Science and Technology*, 30(7):075012, 7 2021.

[28] S. M. Starikovskaia. Plasma assisted ignition and combustion. *Journal of Physics D: Applied Physics*, 39(16):R265–R299, 8 2006.

[29] Tomohiro Nozaki and Ken Okazaki. Non-thermal plasma catalysis of methane: Principles, energy efficiency, and applications. *Catalysis Today*, 211:29–38, 8 2013.

[30] Mutsukazu Kamo, Yoichiro Sato, Seiichiro Matsumoto, and Nobuo Setaka. Diamond synthesis from gas phase in microwave plasma. *Journal of Crystal Growth*, 62(3):642–644, 1983.

[31] Yoav Yair, Yukihiro Takahashi, Roy Yaniv, U. Ebert, and Yukihiro Goto. A study of the possibility of sprites in the atmospheres of other planets. *Journal of Geophysical Research E: Planets*, 114(9):1–10, 2009.

[32] Christoph Köhn, Saša Dujko, Olivier Chanrion, and Torsten Neubert. Streamer propagation in the atmosphere of Titan and other N2:CH4 mixtures compared to N2:O2 mixtures. *Icarus*, 333(May):294–305, 2019.

[33] L D Horton. Atomic and molecular data needs for fusion research. *Physica Scripta*, T65:175–178, 1 1996.

[34] L. C. Pitchford, L. L. Alves, K. Bartschat, S. F. Biagi, M. C. Bordage, A. V. Phelps, C. M. Ferreira, G J M Hagelaar, W. L. Morgan, S. Pancheshnyi, V. Puech, A. Stauffer, and O. Zatsarinny. Comparisons of sets of electron–neutral scattering cross sections and swarm parameters in noble gases: I. Argon. *Journal of Physics D: Applied Physics*, 46(33):334001, 8 2013.

[35] Stephen J. Buckman, Michael J. Brunger, and Kurunathan Ratnavelu. Atomic scattering data and their evaluation: Strategies for obtaining complete cross-section sets for electron collision processes. *Fusion Science and Technology*, 63(3):385–391, 2013.

[36] Z. Lj Petrović, M. Šuvakov, Z Nikitović, Saša Dujko, O Šašić, J. Jovanović, G. Malović, and V. Stojanović. Kinetic phenomena in charged particle transport in gases, swarm parameters and cross section data. *Plasma Sources Science and Technology*, 16(1):S1–S12, 2 2007.

[37] L. L. Alves. The IST-LISBON database on LXCat. *Journal of Physics: Conference Series*, 565(1):012007, 12 2014.

[38] R.W. Crompton. Benchmark Measurements of Cross Sections for Electron Collisions: Electron Swarm Methods. In *Advances in Atomic, Molecular and Optical Physics*, volume 33, pages 97–148. 1994.

[39] Mi Young Song, Jung Sik Yoon, Hyuck Cho, Grzegorz P. Karwasz, Viatcheslav Kokoouline, Yoshiharu Nakamura, and Jonathan Tennyson. "Recommended" cross sections for electron collisions with molecules, 3 2020.

[40] Mi-Young Song, Jung-Sik Yoon, Hyuck Cho, Yukikazu Itikawa, Grzegorz P. Karwasz, Viatcheslav Kokoouline, Yoshiharu Nakamura, and Jonathan Tennyson. Cross Sections for Electron Collisions with Methane. *Journal of Physical and Chemical Reference Data*, 44(2):023101, 6 2015.

[41] Michael Allan. Improved techniques of measuring accurate electron - molecule cross sections near threshold and over a large angular range. *AIP Conference Proceedings*, 901(1):107–116, April 2007. Publisher: American Institute of Physics.

[42] Kamil Fedus and Grzegorz P. Karwasz. Ramsauer-Townsend minimum in methane — modified effective range analysis. *Eur. Phys. J. D*, 68(4):93, April 2014.

[43] T. Sakae, S. Sumiyoshi, E. Murakami, Y. Matsumoto, K. Ishibashi, and A. Katase. Scattering of electrons by CH4, CF4and SF6in the 75-700 eV range. *J. Phys. B: At. Mol. Opt. Phys.*, 22(9):1385–1394, May 1989. Publisher: IOP Publishing.

[44] M. T. Elford, S. J. Buckman, and M. Brunger. 6.3 Elastic momentum transfer cross sections. In Y. Itikawa, editor, *Interactions of Photons and Electrons with Molecules*, volume 17C, pages 6085–6117. Springer-Verlag, Berlin/Heidelberg, 2003. Series Title: Landolt-Börnstein - Group I Elementary Particles, Nuclei and Atoms.

[45] M. Kurachi and Y. Nakamura. *Proceedings of 13th Symposium on Ion Sources and Ion-Assisted Technology*, 1990.

[46] B. G. Lindsay and M. A. Mangan. 5.1 Ionization. In Y. Itikawa, editor, *Interactions of Photons and Electrons with Molecules*, volume 17C, pages 5001–5077. Springer-Verlag, Berlin/Heidelberg, 2003. Series Title: Landolt-Börnstein - Group I Elementary Particles, Nuclei and Atoms.

[47] Prashant Rawat, Vaibhav S. Prabhudesai, M. A. Rahman, N. Bhargava Ram, and E. Krishnakumar. Absolute cross sections for dissociative electron attachment to NH3 and CH4. *International Journal of Mass Spectrometry*, 277(1):96–102, November 2008.

[48] Abdelatif Gadoum and Djilali Benyoucef. Set of the Electron Collision Cross Sections for Methane Molecule. *IEEE Transactions on Plasma Science*, 47(3):1505–1513, 2019.

[49] Daniel A. Erwin and Joseph A. Kunc. Electron-impact dissociation of the methane molecule into neutral fragments. *Physical Review A - Atomic, Molecular, and Optical Physics*, 72(5):1–6, 2005.

[50] Daniel A. Erwin and Joseph A. Kunc. Dissociation and ionization of the methane molecule by nonrelativistic electrons including the near threshold region. *Journal of Applied Physics*, 103(6):064906, 3 2008.

[51] Safa Motlagh and John H. Moore. Cross sections for radicals from electron impact on methane and fluoroalkanes. *Journal of Chemical Physics*, 109(2):432–438, 1998.

[52] R. K. Janev and D. Reiter. Collision processes of CHy and CHy+ hydrocarbons with plasma electrons and protons. *Physics of Plasmas*, 9(9):4071, 2002.

[53] D. Reiter and R. K. Janev. Hydrocarbon Collision Cross Sections for Magnetic Fusion: The Methane, Ethane and Propane Families. *Contributions to Plasma Physics*, 50(10):986–1013, 2010.

[54] Marcin Ziółkowski, Anna Vikár, Maricris Lodriguito Mayes, Ákos Bencsura, György Lendvay, and George C. Schatz. Modeling the electron-impact dissociation of methane. *The Journal of Chemical Physics*, 137(22):22A510, 12 2012.

[55] Tohru Nakano, Hirotaka Toyoda Hirotaka Toyoda, and Hideo Sugai Hideo Sugai. Electron-Impact Dissociation of Methane into CH3 and CH2 Radicals II. Absolute Cross Sections. *Jpn. J. Appl. Phys.*, 30(11R):2912, November 1991. Publisher: IOP Publishing.

[56] Tohru Nakano, Hirotaka Toyoda Hirotaka Toyoda, and Hideo Sugai Hideo Sugai. Electron-Impact Dissociation of Methane into CH3 and CH2 Radicals I. Relative Cross Sections. *Jpn. J. Appl. Phys.*, 30(11R):2908, November 1991. Publisher: IOP Publishing.

[57] C. Makochekanwa, K. Oguri, R. Suzuki, T. Ishihara, M. Hoshino, M. Kimura, and H. Tanaka. Experimental observation of neutral radical formation from CH4 by electron impact in the threshold region. *Physical Review A - Atomic, Molecular, and Optical Physics*, 74(4):4–7, 2006.

[58] Charles E. Melton and P. S. Rudolph. Radiolysis of methane in a wide-range radiolysis source of a mass spectrometer. I. Individual and total cross sections for the production of positive ions, negative ions, and free radicals by electrons. *The Journal of Chemical Physics*, 47(5):1771–1774, 1967.

[59] O Sasic, G Malovic, A Strinic, Z Nikitovic, and Z Lj Petrovic. Excitation coefficients and cross-sections for electron swarms in methane. *New Journal of Physics*, 6:74–74, 7 2004.

[60] Harold F. Winters. Dissociation of methane by electron impact. *The Journal of Chemical Physics*, 63(8):3462–3466, 10 1975.

[61] Toshizo Shirai, Tatsuo Tabata, Hiroyuki Tawara, and Yukikazu Itikawa. Analytic cross sections for electron collisions with hydrocarbons: CH_4, C_2H_6, C_2H_4, C_2H_2, C_3H_8, and C_3H_6. *Atomic Data and Nuclear Data Tables*, 80(2):147–204, March 2002.

[62] A. Salabas, G. Gousset, and L. L. Alves. Two-dimensional fluid modelling of charged particle transport in radio-frequency capacitively coupled discharges. *Plasma Sources Sci. Technol.*, 11(4):448–465, October 2002. Publisher: IOP Publishing.

[63] L. S. Frost and A. V. Phelps. Rotational Excitation and Momentum Transfer Cross Sections for Electrons in H2 and N2 from Transport Coefficients. *Phys. Rev.*, 127(5):1621–1633, September 1962. Publisher: American Physical Society.

[64] S. A. J. Al-Amin, H. N. Kucukarpaci, and J. Lucas. Electron swarm parameters in oxygen and methane. *J. Phys. D: Appl. Phys.*, 18(9):1781–1794, September 1985. Publisher: IOP Publishing.

[65] L. W. Cochran and D. W. Forester. Diffusion of Slow Electrons in Gases. *Phys. Rev.*, 126(5):1785–1788, June 1962. Publisher: American Physical Society.

[66] T. L. Cottrell and Isobel C. Walker. Drift velocities of slow electrons in polyatomic gases. *Trans. Faraday Soc.*, 61(0):1585–1593, January 1965. Publisher: The Royal Society of Chemistry.

[67] D. K. Davies, L. E. Kline, and W. E. Bies. Measurements of swarm parameters and derived electron collision cross sections in methane. *Journal of Applied Physics*, 65(9):3311–3323, May 1989. Publisher: American Institute of Physics.

[68] A. E. D. Heylen. Ionization coefficients and sparking voltages from methane to butane. *International Journal of Electronics*, 39(6):653–660, December 1975. Publisher: Taylor & Francis.

[69] S. R. Hunter, J. G. Carter, and L. G. Christophorou. Electron transport measurements in methane using an improved pulsed Townsend technique. *Journal of Applied Physics*, 60(1):24–35, July 1986. Publisher: American Institute of Physics.

[70] C. S. Lakshminarasimha and J. Lucas. The ratio of radial diffusion coefficient to mobility for electrons in helium, argon, air, methane and nitric oxide. *J. Phys. D: Appl. Phys.*, 10(3):313–321, February 1977. Publisher: IOP Publishing.

[71] S. L. Lin, R. E. Robson, and E. A. Mason. Moment theory of electron drift and diffusion in neutral gases in an electrostatic field. *J. Chem. Phys.*, 71(8):3483–3498, October 1979. Publisher: American Institute of Physics.

[72] P. G. Millican and I. C. Walker. Electron swarm characteristic energies (D/μ) in methane, perdeuteromethane, silane, perdeuterosilane, phosphine and hydrogen sulphide at low E/N. *J. Phys. D: Appl. Phys.*, 20(2):193–196, February 1987. Publisher: IOP Publishing.

[73] W. J. Pollock. Momentum transfer and vibrational cross-sections in non-polar gases. *Trans. Faraday Soc.*, 64(0):2919–2926, January 1968. Publisher: The Royal Society of Chemistry.

[74] M. Shimozuma and H. Tagashira. Measurement of the ionisation coefficients in nitrogen and methane mixtures. *J. Phys. D: Appl. Phys.*, 14(10):1783–1789, October 1981. Publisher: IOP Publishing.

[75] Particle Swarm Boltzmann Solver. www.gitlab.com/MD-CWI-NL/particle_swarm. version: 9b7e181f.

[76] Jannis Teunissen and Ute Ebert. 3D PIC-MCC simulations of discharge inception around a sharp anode in nitrogen/oxygen mixtures. *Plasma Sources Science and Technology*, 25(4):044005, 8 2016.

[77] Alan A. Sebastian and J. M. Wadehra. Time-dependent behaviour of electron transport in methane-argon mixtures. *Journal of Physics D: Applied Physics*, 38(10):1577–1587, 2005.

[78] Will J Brigg, Jonathan Tennyson, and Martin Plummer. R-matrix calculations of low-energy electron collisions with methane. *Journal of Physics B: Atomic, Molecular and Optical Physics*, 47(18):185203, 9 2014.

[79] Scott Habershon, David E. Manolopoulos, Thomas E. Markland, and Thomas F. Miller. Ring-Polymer Molecular Dynamics: Quantum Effects in Chemical Dynamics from Classical Trajectories in an Extended Phase Space. *Annu. Rev. Phys. Chem.*, 64(1):387–413, April 2013. Publisher: Annual Reviews.

[80] J. Perrin, J. P. M. Schmitt, G. de Rosny, B. Drevillon, J. Huc, and A. Lloret. Dissociation cross sections of silane and disilane by electron impact. *Chemical Physics*, 73(3):383–394, December 1982.

[81] Ankit Rohatgi. Webplotdigitizer: Version 4.4, 2020.

[82] Dennis Bouwman, Jannis Teunissen, and Ute Ebert. 3D particle simulations of positive air–methane streamers for combustion. *Plasma Sources Science and Technology*, 31(4):045023, 4 2022.

[83] Hyun Ha Kim. Nonthermal plasma processing for air-pollution control: A historical review, current issues, and future prospects. *Plasma Processes and Polymers*, 1(2):91–110, 2004.

[84] Behnaz Bagheri, Jannis Teunissen, and Ute Ebert. Simulation of positive streamers in CO 2 and in air: the role of photoionization or other electron sources. *Plasma Sources Science and Technology*, 29(12):125021, 12 2020.

[85] Hani Francisco, Behnaz Bagheri, and Ute Ebert. Electrically isolated propagating streamer heads formed by strong electron attachment. *Plasma Sources Science and Technology*, 30(2):025006, 2 2021.

[86] Behnaz Bagheri and Jannis Teunissen. The effect of the stochasticity of photoionization on 3D streamer simulations. *Plasma Sources Science and Technology*, 28(4):045013, 4 2019.

[87] She Chen, Feng Wang, Qiuqin Sun, and Rong Zeng. Branching characteristics of positive streamers in nitrogen-oxygen gas mixtures. *IEEE Transactions on Dielectrics and Electrical Insulation*, 25(3):1128–1134, 2018.

[88] D. Dubrovin, Sander Nijdam, E. M. van Veldhuizen, U. Ebert, Y. Yair, and C. Price. Sprite discharges on Venus and Jupiter-like planets: A laboratory investigation. *Journal of Geophysical Research: Space Physics*, 115(A6):A00E34, 6 2010.

[89] C. Köhn, O. Chanrion, M. Bødker Enghoff, and S. Dujko. Streamer Discharges in the Atmosphere of Primordial Earth. *Geophysical Research Letters*, 49(5):1–11, 3 2022.

[90] T M P Briels, E M van Veldhuizen, and U. Ebert. Positive streamers in air and nitrogen of varying density: experiments on similarity laws. *Journal of Physics D: Applied Physics*, 41(23):234008, 12 2008.

[91] George V. Naidis. Modelling of transient plasma discharges in atmospheric-pressure methane-air mixtures. *Journal of Physics D: Applied Physics*, 40(15):4525–4531, 2007.

[92] Yiguang Ju and Wenting Sun. Plasma assisted combustion: Dynamics and chemistry. *Progress in Energy and Combustion Science*, 48(1):21–83, 6 2015.

[93] Douglas Breden, Laxminarayan L. Raja, Cherian A. Idicheria, Paul M. Najt, and Shankar Mahadevan. A numerical study of high-pressure non-equilibrium streamers for combustion ignition application. *Journal of Applied Physics*, 114(8):083302, 8 2013.

[94] Douglas Breden, Cherian A. Idicheria, Seunghwan Keum, Paul M. Najt, and Laxminarayan L. Raja. Modeling of a Dielectric-Barrier Discharge-Based Cold Plasma Combustion Ignition System. *IEEE Transactions on Plasma Science*, 47(1):410–418, 2019.

[95] Hidemasa Takana and Hideya Nishiyama. Numerical simulation of nanosecond pulsed DBD in lean methane–air mixture for typical conditions in internal engines. *Plasma Sources Science and Technology*, 23(3):034001, 5 2014.

[96] Suo Yang, Sharath Nagaraja, Wenting Sun, and Vigor Yang. Multiscale modeling and general theory of non-equilibrium plasma-assisted ignition and combustion. *Journal of Physics D: Applied Physics*, 50(43):433001, 11 2017.

[97] Dmitry Levko and Laxminarayan L. Raja. Fluid versus global model approach for the modeling of active species production by streamer discharge. *Plasma Sources Science and Technology*, 26(3):035003, 2 2017.

[98] Guillaume Pilla, David Galley, Deanna A. Lacoste, François Lacas, Denis Veynante, and Christophe O. Laux. Stabilization of a turbulent premixed flame using a nanosecond repetitively pulsed plasma. *IEEE Transactions on Plasma Science*, 34(6):2471–2477, 2006.

[99] Timothy Ombrello, Sang Hee Won, Yiguang Ju, and Skip Williams. Flame propagation enhancement by plasma excitation of oxygen. Part I: Effects of O3. *Combustion and Flame*, 157(10):1906–1915, 10 2010.

[100] Timothy Ombrello, Sang Hee Won, Yiguang Ju, and Skip Williams. Flame propagation enhancement by plasma excitation of oxygen. Part II: Effects of O2(a1Δg). *Combustion and Flame*, 157(10):1916–1928, 10 2010.

[101] D. A. Lacoste, J. P. Moeck, D. Durox, C. O. Laux, and T. Schuller. Effect of Nanosecond Repetitively Pulsed Discharges on the Dynamics of a Swirl-Stabilized Lean Premixed Flame. In *Volume 1A: Combustion, Fuels and Emissions*, volume 1 A, pages 1–9. American Society of Mechanical Engineers, 6 2013.

[102] D. Singleton, S. J. Pendleton, and M. A. Gundersen. The role of non-thermal transient plasma for enhanced flame ignition in C2H4 –air. *Journal of Physics D: Applied Physics*, 44(2):022001, 1 2011.

[103] Alejandro Luque and U. Ebert. Electron density fluctuations accelerate the branching of positive streamer discharges in air. *Physical Review E*, 84(4):046411, 10 2011.

[104] Jannis Teunissen and Ute Ebert. Controlling the weights of simulation particles: adaptive particle management using k-d trees. *Journal of Computational Physics*, 259:318–330, 2 2014.

[105] S. Kawaguchi, K. Takahashi, and K. Satoh. Electron collision cross section set for N 2 and electron transport in N 2 , N 2 /He, and N 2 /Ar. *Plasma Sources Science and Technology*, 30(3):035010, 3 2021.

[106] Yukikazu Itikawa. Cross Sections for Electron Collisions with Oxygen Molecules. *Journal of Physical and Chemical Reference Data*, 38(1):1–20, 3 2009.

[107] S. A. Lawton and A. V. Phelps. Excitation of the b1Σg+ state of O2 by low energy electrons. *The Journal of Chemical Physics*, 69(3):1007–1009, 1978.

[108] Mi-Young Song, Jung-Sik Yoon, Hyuck Cho, Grzegorz P Karwasz, Viatcheslav Kokoouline, Yoshiharu Nakamura, James R. Hamilton, and Jonathan Tennyson. Cross Sections for Electron Collisions with NF 3. *Journal of Physical and Chemical Reference Data*, 46(4):043104, 12 2017.

[109] BOLSIG+ (version 12/2019). www.bolsig.laplace.univ-tlse.fr.

[110] J Stephens, M Abide, A Fierro, and A Neuber. Practical considerations for modeling streamer discharges in air with radiation transport. *Plasma Sources Science and Technology*, 27(7):075007, 7 2018.

[111] Olivier Chanrion and T. Neubert. A PIC-MCC code for simulation of streamer propagation in air. *Journal of Computational Physics*, 227(15):7222–7245, 7 2008.

[112] F. Albugues, A. Birot, D. Blanc, H. Brunet, J. Galy, P. Millet, and J. L. Teyssier. Destruction of the levels C3Πu(v=0, v=1) of nitrogen by O2, CO2, CH4, and H2O. *The Journal of Chemical Physics*, 61(7):2695–2699, 10 1974.

[113] Xiaoran Li, Siebe Dijcks, Sander Nijdam, Anbang Sun, Ute Ebert, and Jannis Teunissen. Comparing simulations and experiments of positive streamers in air: steps toward model validation. *Plasma Sources Science and Technology*, 30(9):095002, 9 2021.

[114] Kosei Kameta, Noriyuki Kouchi, Masatoshi Ukai, and Yoshihiko Hatano. Photoabsorption, photoionization, and neutral-dissociation cross sections of simple hydrocarbons in the vacuum ultraviolet range. *Journal of Electron Spectroscopy and Related Phenomena*, 123(2-3):225–238, 2002.

[115] S. Pancheshnyi. Photoionization produced by low-current discharges in O2 , air, N2 and CO2. *Plasma Sources Science and Technology*, 24(1):015023, 12 2014.

[116] Jannis Teunissen and Ute Ebert. Afivo: A framework for quadtree/octree AMR with shared-memory parallelization and geometric multigrid methods. *Computer Physics Communications*, 233:156–166, 12 2018.

[117] G. Diniz, C. Rutjes, U. Ebert, and I. S. Ferreira. Cold electron run-away below the friction curve. *Journal of Geophysical Research: Atmospheres*, 124(1):189–198, 12 2018.

[118] Atsushi Komuro, Ryo Ono, and Tetsuji Oda. Numerical simulation for production of O and N radicals in an atmospheric-pressure streamer discharge. *Journal of Physics D: Applied Physics*, 45(26):265201, 7 2012.

[119] Andrey Starikovskiy, Nickolay Aleksandrov, and Aleksandr Rakitin. Plasma-assisted ignition and deflagration-to-detonation transition. *Philosophical Transactions of the Royal Society A: Mathematical, Physical and Engineering Sciences*, 370(1960):740–773, 2012.

[120] N. Yu Babaeva and George V. Naidis. Two-Dimensional modeling of positive streamer propagation in flue gases in sphere-plane gaps. *IEEE Transactions on Plasma Science*, 26(1):41–45, 1998.

[121] Muyang Qian, Gui Li, Jinsong Kang, Sanqiu Liu, Chunsheng Ren, Jialiang Zhang, and Dezhen Wang. Fluid modeling of radical species generation mechanism in dense methane-air mixture streamer discharge. *Physics of Plasmas*, 25(1), 2018.

[122] Dennis Bouwman, Hani Francisco, and Ute Ebert. Estimating the properties of single positive air streamers from measurable parameters. *Plasma Sources Science and Technology*, 32(7):075015, 7 2023.

[123] Behnaz Bagheri, Jannis Teunissen, U. Ebert, M. M. Becker, S. Chen, O. Ducasse, O. Eichwald, D. Loffhagen, Alejandro Luque, D. Mihailova, J. M. Plewa, Jan van Dijk, and M. Yousfi. Comparison of six simulation codes for positive streamers in air. *Plasma Sources Science and Technology*, 27(9):095002, 9 2018.

[124] P. O. Kochkin, C. V. Nguyen, A. P.J. Van Deursen, and U. Ebert. Experimental study of hard x-rays emitted from metre-scale positive discharges in air. *Journal of Physics D: Applied Physics*, 45(42), 10 2012.

[125] B. M. Hare, O. Scholten, J. Dwyer, U. Ebert, Sander Nijdam, A. Bonardi, S. Buitink, A. Corstanje, H. Falcke, T. Huege, J. R. Hörandel, G. K. Krampah, P. Mitra, K. Mulrey, B. Neijzen, A. Nelles, H. Pandya, J. P. Rachen, L. Rossetto, T. N.G. Trinh, S. Ter Veen, and T. Winchen. Radio Emission Reveals Inner Meter-Scale Structure of Negative Lightning Leader Steps. *Physical Review Letters*, 124(10), 3 2020.

[126] C. Sterpka, J. Dwyer, N. Liu, B. M. Hare, O. Scholten, S. Buitink, S. ter Veen, and A. Nelles. The Spontaneous Nature of Lightning Initiation Revealed. *Geophysical Research Letters*, 48(23):2520–2533, 12 2021.

[127] Siebe Dijcks, Martijn van der Leegte, and Sander Nijdam. Imaging and reconstruction of positive streamer discharge tree structures. *Plasma Sources Science and Technology*, 32(4), 4 2023.

[128] Zhen Wang, Siebe Dijcks, Yihao Guo, Martijn van der Leegte, Anbang Sun, Ute Ebert, Sander Nijdam, and Jannis Teunissen. Quantitative modeling of streamer discharge branching in air. *Plasma Sources Science and Technology*, 32(8):085007, 8 2023.

[129] Alejandro Luque, M. González, and F. J. Gordillo-Vázquez. Streamer discharges as advancing imperfect conductors: inhomogeneities in long ionized channels. *Plasma Sources Science and Technology*, 26(12):125006, 11 2017.

[130] Hani Francisco, Jannis Teunissen, Behnaz Bagheri, and Ute Ebert. Simulations of positive streamers in air in different electric fields: steady motion of solitary streamer heads and the stability field. *Plasma Sources Science and Technology*, 30(11):115007, 11 2021.

[131] Xiaoran Li, Baohong Guo, Anbang Sun, Ute Ebert, and Jannis Teunissen. A computational study of steady and stagnating positive streamers in N2 –O2 mixtures. *Plasma Sources Science and Technology*, 31(6):065011, 6 2022.

[132] Baohong Guo, Xiaoran Li, Ute Ebert, and Jannis Teunissen. A computational study of accelerating, steady and fading negative streamers in ambient air. *Plasma Sources Science and Technology*, 31(9):095011, 9 2022.

[133] C. Pavan, M. Martinez-Sanchez, and C. Guerra-Garcia. Investigations of positive streamers as quasi-steady structures using reduced order models. *Plasma Sources Science and Technology*, 29(9):095004, 9 2020.

[134] T M P Briels, J. Kos, G J J Winands, E M van Veldhuizen, and U. Ebert. Positive and negative streamers in ambient air: measuring diameter, velocity and dissipated energy. *Journal of Physics D: Applied Physics*, 41(23):234004, 12 2008.

[135] George V. Naidis. Modelling of plasma chemical processes in pulsed corona discharges. *Journal of Physics D: Applied Physics*, 30(8):1214–1218, 1997.

[136] Chao Li, W. J.M. Brok, U. Ebert, and J. J.A.M. Van Der Mullen. Deviations from the local field approximation in negative streamer heads. *Journal of Applied Physics*, 101(12):1–17, 2007.

[137] George V. Naidis. Efficiency of generation of chemically active species by pulsed corona discharges. *Plasma Sources Science and Technology*, 21(4):042001, 8 2012.

[138] S. Pancheshnyi, S. M. Starikovskaia, and Andrey Starikovskiy. Role of photoionization processes in propagation of cathode-directed streamer. *Journal of Physics D: Applied Physics*, 34(1):105–115, 1 2001.

[139] N.G. Lehtinen. Physics and Mathematics of Electric Streamers. *Izvestiya vysshikh uchebnykh zavedenii. Radiofizika*, 64(1):12–28, 2021.

[140] Mojtaba Niknezhad, Olivier Chanrion, Joachim Holbøll, and Torsten Neubert. Underlying mechanism of the stagnation of positive streamers. *Plasma Sources Science and Technology*, 30(11):115014, 11 2021.

[141] Natalia Yu Babaeva and George V. Naidis. Universal nature and specific features of streamers in various dielectric media. *Journal of Physics D: Applied Physics*, 54(22):223002, 6 2021.

[142] Jannis Teunissen and Ute Ebert. Simulating streamer discharges in 3D with the parallel adaptive Afivo framework. *Journal of Physics D: Applied Physics*, 50(47):474001, 11 2017.

[143] Phelps database (available at www.lxcat.net), retrieved March 2019.

[144] A. Bourdon, V. P. Pasko, N. Y. Liu, S. Célestin, P. Ségur, and E. Marode. Efficient models for photoionization produced by non-thermal gas discharges in air based on radiative transfer and the Helmholtz equations. *Plasma Sources Science and Technology*, 16(3):656–678, 2007.

[145] N. Yu Babaeva and George V. Naidis. Dynamics of positive and negative streamers in air in weak uniform electric fields. *IEEE Transactions on Plasma Science*, 25(2):375–379, 1997.

[146] Alejandro Luque and U. Ebert. Sprites in varying air density: Charge conservation, glowing negative trails and changing velocity. *Geophysical Research Letters*, 37(6), 3 2010.

[147] A. A. Kulikovsky. Analytical Model of Positive Streamer in Weak Field in Air: Application to Plasma Chemical Calculations. *Physical Review E*, 57(6):7066–7074, 6 1998.

[148] Andrey Starikovskiy, Edward Bazelyan, and Nick L Aleksandrov. The influence of humidity on positive streamer propagation in long air gap. *Plasma Sources Science and Technology*, 11 2022.

[149] Jorge J Moré, Burton S Garbow, and Kenneth E Hillstrom. User guide for MINPACK-1. Technical report, CM-P00068642, 1980.

[150] M. Seeger, M. Schwinne, R. Bini, N. Mahdizadeh, and T. Votteler. Dielectric recovery in a high-voltage circuit breaker in SF 6. *Journal of Physics D: Applied Physics*, 45(39), 10 2012.

[151] Philippe Lalande, Anne Bondiou-Clergerie, G. Bacchiega, and I. Gallimberti. Observations and modeling of lightning leaders. *Comptes Rendus Physique*, 3(10):1375–1392, 12 2002.

[152] Caitano L. Da Silva and Victor P. Pasko. Dynamics of streamer-to-leader transition at reduced air densities and its implications for propagation of lightning leaders and gigantic jets. *Journal of Geophysical Research Atmospheres*, 118(24):561–13, 12 2013.

[153] R. Morrow. Theory of negative corona in oxygen. *Physical Review A*, 32(3):1799–1809, 9 1985.

[154] N L Aleksandrov and E M Bazelyan. Simulation of long-streamer propagation in air at atmospheric pressure. *Journal of Physics D: Applied Physics*, 29(3):740–752, 3 1996.

[155] Jing-Ming Guo and Chwan-Hwa Wu. Streamer radius model and its assessment using two-dimensional models. *IEEE Transactions on Plasma Science*, 24(6):1348–1358, 1996.

[156] V. P. Pasko, U. S. Inan, and T. F. Bell. Fractal structure of sprites. *Geophysical Research Letters*, 27(4):497–500, 2 2000.

[157] Mose Akyuz, Anders Larsson, Vernon Cooray, and Gustav Strandberg. 3D simulations of streamer branching in air. *Journal of Electrostatics*, 59(2):115–141, 2003.

[158] Nikolai G Lehtinen and Robert Marskar. What Determines the Parameters of a Propagating Streamer: A Comparison of Outputs of the Streamer Parameter Model and of Hydrodynamic Simulations. *Atmosphere*, 12(12):1664, 12 2021.

[159] I. Gallimberti. The mechanism of the long spark formation. *Le Journal de Physique Colloques*, 40(C7):7–193, 7 1979.

[160] C. T. Phelps. Field-enhanced propagation of corona streamers. *Journal of Geophysical Research*, 76(24):5799–5806, 8 1971.

[161] R. F. Griffiths and C. T. Phelps. The effects of air pressure and water vapour content on the propagation of positive corona streamers, and their implications to lightning initiation. *Quarterly Journal of the Royal Meteorological Society*, 102(432):419–426, 4 1976.

[162] N.L. Allen and M. Boutlendj. Study of the electric fields required for streamer propagation in humid air. *IEE Proceedings A Science, Measurement and Technology*, 138(1):37, 1991.

[163] N L Allen and A Ghaffar. The conditions required for the propagation of a cathode-directed positive streamer in air. *Journal of Physics D: Applied Physics*, 28(2):331–337, 2 1995.

[164] Jianqi Qin and Victor P. Pasko. On the propagation of streamers in electrical discharges. *Journal of Physics D: Applied Physics*, 47(43), 10 2014.

[165] I. A. Kossyi, A. Yu Kostinsky, A. A. Matveyev, and V. P. Silakov. Kinetic scheme of the non-equilibrium discharge in nitrogen-oxygen mixtures. *Plasma Sources Science and Technology*, 1(3):207–220, 1992.

[166] Sergey Pancheshnyi. Effective ionization rate in nitrogen–oxygen mixtures. *Journal of Physics D: Applied Physics*, 46(15):155201, 4 2013.

[167] Nickolay Aleksandrov and E. M. Bazelyan. Ionization processes in spark discharge plasmas. *Plasma Sources Science and Technology*, 8(2):285–294, 1999.

[168] Alejandro Luque, Fabian Brau, and U. Ebert. Saffman-Taylor streamers: Mutual finger interaction in spark formation. *Physical Review E - Statistical, Nonlinear, and Soft Matter Physics*, 78(1):1–7, 2008.

[169] Hidetosi Takahasi and Masatake Mori. Double exponential formulas for numerical integration. *Publications of the Research Institute for Mathematical Sciences*, 9(3):721–741, 1974.

[170] LXCat. www.lxcat.net.

[171] Robert P. Nieuwenhuizen, Dennis D. Bouwman, and Klamer Schutte. Assessing the prospects for robust sub-diffraction limited super-resolution imaging with deep neural networks. In Richard C. Hollins, Gerald S. Buller, and Robert A. Lamb, editors, *Emerging Imaging and Sensing Technologies for Security and Defence III; and Unmanned Sensors, Systems, and Countermeasures*, page 3. SPIE, 10 2018.

[172] Yaogong Wang, Xiaoqin Ma, Dennis Bouwman, Zhuoran Liu, Ute Ebert, and Xiaoning Zhang. Different ionization mechanisms in pulsed micro-DBD's in argon at different pressures. *Plasma Sources Science and Technology*, 31(10):105015, 10 2022.

Curriculum Vitae

Dennis Bouwman was born on the 8$^{\text{th}}$ of July 1994 in Amsterdam, The Netherlands. In 2012 he enrolled in the Double Degree program at the TU Delft and in 2016 he simultaneously obtained two bachelor's degrees in Applied Physics and Applied Mathematics. Afterwards he pursued a master's degree in Applied Mathematics with a specialization in Computational Science which was obtained in 2019. In the same year he started his Ph.D. in the field of Computational Plasma Physics at the Centrum Wiskunde & Informatica.

In his free time Dennis enjoys playing the piano, he favors classical music of the romantic era. With his friends he plays many card- and board games which he hardly ever manages to win. He is a vivid *Dungeons & Dragons* enthusiast. He owns 82 plants and 0 bicycles.

List of publications

1. Robert P. Nieuwenhuizen, Dennis D. Bouwman, and Klamer Schutte. Assessing the prospects for robust sub-diffraction limited super-resolution imaging with deep neural networks. In Richard C. Hollins, Gerald S. Buller, and Robert A. Lamb, editors, *Emerging Imaging and Sensing Technologies for Security and Defence III; and Unmanned Sensors, Systems, and Countermeasures*, page 3. SPIE, 10 2018

2. Dennis D. Bouwman, Andy Martinez, Bastiaan J Braams, and U. Ebert. Neutral dissociation of methane by electron impact and a complete and consistent cross section set. *Plasma Sources Science and Technology*, 30(7):075012, 7 2021

3. Dennis Bouwman, Jannis Teunissen, and Ute Ebert. 3D particle simulations of positive air–methane streamers for combustion. *Plasma Sources Science and Technology*, 31(4):045023, 4 2022

4. Yaogong Wang, Xiaoqin Ma, Dennis Bouwman, Zhuoran Liu, Ute Ebert, and Xiaoning Zhang. Different ionization mechanisms in pulsed micro-DBD's in argon at different pressures. *Plasma Sources Science and Technology*, 31(10):105015, 10 2022

5. Dennis Bouwman, Hani Francisco, and Ute Ebert. Estimating the properties of single positive air streamers from measurable parameters. *Plasma Sources Science and Technology*, 32(7):075015, 7 2023

In preperation

6. Dennis Bouwman, Alejandro Luque, and Ute Ebert. Approximating steady positive air streamers with an axial model. *In preparation*

Other contributions

7. Song-Bouwman database for electron scattering cross sections with CH_4 (available at www.lxcat.net in the community database.)